

Conditional Moment Closure Model for Ignition of  
Homogeneous Fuel/Air Mixtures in Internal Combustion  
Engines

Dissertation

Presented in Partial Fulfillment of the Requirements for the Degree Doctor of  
Philosophy in the Graduate School of The Ohio State University

By

Wei Wang,

Graduate Program in Mechanical Engineering

The Ohio State University

2020

Dissertation Committee:

Seung Hyun Kim, Associate Professor, Advisor

Datta Gaitonde, Professor

Jeffrey Sutton, Professor

Shawn Midlam-Mohler, Professor of Practice

© Copyright by

Wei Wang

2020

## Abstract

To improve the fuel economy and to reduce the emission in internal combustion (IC) engines, advanced engine technologies such as the homogeneous charge compression ignition (HCCI), further increasing the compression ratio, and gasoline engine downsizing with charge boosting need to be further developed. The development of these technologies is restricted by the prediction and control of the ignition of premixed fuel/air mixtures. The ignition of the premixed mixtures in IC engines is governed by complex chemical kinetics. The in-cylinder flow turbulence, temperature inhomogeneity, and other mixture conditions affect the ignition processes by influencing the chemical reaction rates. In this study, the conditional moment closure (CMC) method is extended for the ignition of the premixed mixtures with temperature inhomogeneity in IC engines. A CMC model based on sensible enthalpy is developed for the ignition of the premixed mixtures. Closure models for the mixing statistics of sensible enthalpy are proposed based on a mapping method. A method to couple the CMC model with a multidimensional flow solver for the prediction of knock in SI engines is developed. In the coupling, a method to reduce the computational cost by solving a subset of species in the flow solver is proposed. The sensible-enthalpy-based CMC model and a total-enthalpy-based formulation are assessed with data from 2-D direct numerical simulation (DNS) of the ignition of homogeneous primary

reference fuel (PRF)-air mixtures with temperature inhomogeneity under HCCI conditions and spark ignition (SI) engine knocking conditions. Results show that the total-enthalpy-based CMC gives good predictions of the heat release rate (HRR) under HCCI conditions when the temperature inhomogeneity level is low, but leads to substantial overprediction under SI engine knocking conditions regardless of the thermal stratification levels. The sensible enthalpy formulation gives good predictions of the HRR for the ignition under HCCI and SI engine knocking conditions due to suppressed conditional temperature fluctuations. The proposed mixing models are found to generally well capture the mixing characteristics of the reacting scalar. A method to couple the CMC model with a multidimensional flow solver is developed and the spatially-integrated total-enthalpy-based CMC model is implemented into CONVERGE user defined functions (UDF) for knock prediction in SI engines using large eddy simulation (LES). Multicycle LES of a gasoline direct injection (GDI) engine is conducted with the total-enthalpy-based CMC model and the results are compared with data from engine experiments. Results show that the onsets of knock in reference knocking cases are captured. The effects of spark timing (ST) retarding and wall temperature on the occurrence of knock are investigated.

This is dedicated to my wife.

Thank you for being together with me in the exploration of the world.

Thank you for encouraging me when I face hardships.

Thank you for sharing my joy and happiness when I progress.

Thank you for your love.

## Acknowledgments

I would like to express my sincere gratitude to my advisor, Professor Seung Hyun Kim, for his guidance, support, encouragement, and criticizing during my PhD study. Without his guidance and support, I would not be able to finish this thesis work. Without his encouragement and criticizing, I would not be able to progress this far in my research. I would like to express my sincere thankfulness to my committee members: Professor Datta Gaitonde, Professor Jeffrey Sutton, and Professor Shawn Midlam-Mohler. Without your kind support and insightful suggestions, I would not be able to finish my defense. I am thankful to Dr. Splitter at ORNL for sharing the engine experiments data. I would like to say thank you to my labmate Yunde Su for sharing the FPF code for the engine simulation and for his discussion and suggestion on topics of my research. I would like to say thank you to my labmates Abhishek Jain, and Weibo Zheng for the sharing of the research experience.

I would like to thank my friends Qi Yan, Jing Guo, and their daughter Yuhan Yan for their comfort and help when we face hardships in our life. I would like to thank my friend Yan Lu for this suggestion and help on my career planning. Many thanks to all my friends for being so kind in my life. Last but not least, I would like to thank my family for their endless love and support. Many thanks to my parents and parents in law for their encouragement and support. Sincere thanks to my wife for her accompany and love.

## Vita

2010-2014 .....	B.S. Energy and Power Engineering, Huazhong University of Science and Technology.
2014-present .....	Graduate Research Associate, Graduate Teaching Associate, The Ohio State University.

## Publications

### Research Publications

#### Journal

W. Wang and S. H. Kim “Sensible-Enthalpy-Based Conditional Moment Closure Model for Homogeneous Charge Compression Ignition with Temperature Inhomogeneity”, *Flow, Turbulence and Combustion*, (2018): 1-20.

#### Conference

W. Wang and S. H. Kim “Assessment of Enthalpy-Based Conditional Moment Closure Models in Predicting Ignition of Lean and Stoichiometric PRF-Air Mixtures with Temperature Inhomogeneity”, *11th U.S. National Combustion Meeting*, March, 2019.

## Fields of Study

Major Field: Mechanical Engineering

## Table of Contents

	Page
Abstract . . . . .	ii
Dedication . . . . .	iv
Acknowledgments . . . . .	v
Vita . . . . .	vi
List of Tables . . . . .	x
List of Figures . . . . .	xi
1. Introduction . . . . .	1
1.1 Motivation and Significance . . . . .	1
1.2 Scope and Objectives of the Research . . . . .	7
1.3 Organization of this Thesis . . . . .	10
2. Literature Review on the Ignition of Premixed Mixtures in IC Engines .	11
2.1 Ignition of Homogeneous Fuel/Air Mixtures in IC Engines . . . . .	11
2.1.1 Charge Ignition in HCCI Engines . . . . .	11
2.1.2 End-gas Auto-ignition in SI Engines . . . . .	14
2.2 Models for Ignition in HCCI engines and End-gas Auto-ignition in SI Engines . . . . .	17
2.2.1 Chemistry Models . . . . .	19
2.2.2 Multizone Models . . . . .	24
2.2.3 Transport Probability Density Function Model . . . . .	26
2.2.4 Enthalpy-Based Flamelet Model . . . . .	26
2.2.5 Total-Enthalpy-Based Conditional Moment Closure Model . . . . .	27

3.	Conditional Moment Closure Method for Ignition of Premixed Mixtures with Temperature Inhomogeneity . . . . .	28
3.1	CMC Method for Turbulent Reacting Flows . . . . .	28
3.1.1	Governing Equations . . . . .	28
3.1.2	Moment Closure Method . . . . .	32
3.1.3	Conditional Moment Closure Method . . . . .	37
3.1.4	Applications of CMC in Turbulent Reacting Flows . . . . .	42
3.2	Spatially-Integrated CMC Model for the Ignition of Premixed Mixtures in IC engines . . . . .	44
3.2.1	Total-Enthalpy-Based CMC Model . . . . .	48
3.2.2	Sensible-Enthalpy-Based CMC Model . . . . .	49
4.	Validation of the Enthalpy-Based CMC Models Using DNS . . . . .	56
4.1	Spatially-Integrated Enthalpy-Based CMC Models for Ignition of Premixed Mixtures . . . . .	57
4.1.1	Spatially-Integrated Enthalpy-Based CMC Models . . . . .	57
4.1.2	Closure Models . . . . .	57
4.2	Numerical Methods for the DNS . . . . .	60
4.3	Validation of CMC Models under HCCI Conditions . . . . .	61
4.3.1	Initial Conditions for the DNS . . . . .	61
4.3.2	Results and Discussion . . . . .	63
4.4	Validation of CMC Models under SI Engine Knocking Conditions . . . . .	80
4.4.1	Initial Conditions for the DNS . . . . .	80
4.4.2	Results and Discussion . . . . .	82
4.5	Conclusions . . . . .	86
5.	Application of CMC in LES of Knock using CONVERGE . . . . .	91
5.1	Spatially-Integrated Total-Enthalpy-Based CMC Method for Knock Prediction . . . . .	92
5.1.1	Spatially-Integrated CMC Method . . . . .	92
5.1.2	Closure for Conditional Reaction Rates . . . . .	93
5.1.3	Closure for the Local FDF . . . . .	93
5.1.4	Closure for the Conditional SDR . . . . .	94
5.2	Method to Couple the CMC Model with the Flow Solver for Knock Prediction . . . . .	95
5.2.1	Base Approach to Couple the CMC Solver and the CONVERGE Flow Solver . . . . .	99
5.2.2	Modifications to Conditioning Variable . . . . .	101

5.2.3	Reducing Computational Cost by Solving a Subset of Species in CONVERGE . . . . .	106
5.2.4	Summary of the Coupling between CMC and CONVERGE	109
5.3	Multicycle LES of Knock in a GDI Engine with Total-Enthalpy- Based CMC for Knock Prediction . . . . .	111
5.3.1	GDI Engine Specifications and Operating Conditions . . . . .	111
5.3.2	Conditions and Models in LES . . . . .	112
5.3.3	Validation of the Total-Enthalpy-Based CMC Model on Knock Prediction . . . . .	116
5.3.4	Conclusions . . . . .	125
6.	Summary and Future Work . . . . .	128
	Bibliography . . . . .	131

## List of Tables

<b>Table</b>	<b>Page</b>
4.1 Initial and simulation conditions for the DNS cases under HCCI conditions. Also shown are the ignition delay times . . . . .	61
4.2 Grid and time step sensitivity study for Case 4 . . . . .	63
4.3 Initial and simulation conditions for the DNS cases under knocking conditions. Also shown are the ignition delays . . . . .	80
5.1 GDI engine specifications and operating conditions in the LES validation study. . . . .	113
5.2 Summary of the conditions for the validation cases chosen from the ORNL engine experiments. The spark timing (ST) is relative to TDC firing, which is at 0 CAD. Negative sign indicates the ST is before the TDC. . . . .	113
5.3 Wall temperature boundary conditions for the LES. . . . .	115

## List of Figures

Figure	Page
1.1 Laser-induced fluorescence (LIF) image of auto-ignition spots in a knocking cycle. The figure is taken from [123]. . . . .	4
2.1 In-cylinder pressure traces for normal and knocking combustion cycles.	15
3.1 Schematic showing the conditional average and fluctuations. Each black circle represents a pair of measured temperature and the mixture fraction. The red solid line shows the temperature averaged with the condition that the mixture fraction takes a particular value. Practically, the conditional average is obtained by taking an average for samples having a certain small range of the mixture fraction, which is represented by the blue dashed lines. The red solid circle is the averaged temperature in that particular bin, i.e. the conditionally averaged temperature. The degree of scatter within the region bounded by the dashed lines represents conditional fluctuations. . . . .	38
3.2 Typical (monotonic) mapping curve with scatter plots of total enthalpy on sensible enthalpy from DNS data. The red solid line is obtained from the mapping in Eq. (3.58). $P(\eta)d\eta$ is the probability of finding the points within the specified enthalpy range. Here, $P(\eta_t)d\eta_t = P(\eta_s)d\eta_s$ .	52
3.3 A non-monotonic mapping curve and the schematic showing the modification to the PDF mapping. The red solid line is obtained from the mapping in Eq. (3.58), with data from a DNS simulation. A given value of total enthalpy will correspond to multiple values of sensible enthalpy when the mapping is non-monotonic. Here, the total enthalpy range $\delta\eta_t$ corresponds to three sensible enthalpy ranges, where $P(\eta_t)\delta\eta_t = \sum_i P(\eta_{s,i})\delta\eta_{s,i}$ . . . . .	54

3.4 Schematic of the modification to the mapping curve for modeling conditional SDR of sensible enthalpy when the mapping is non-monotonic. It has been found that after the modification, the mapping curves become monotonic in the HCCI (fuel-lean) cases. . . . .	55
4.1 Initial temperature field (left) and velocity field for Case 4. . . . .	62
4.2 Temperature fields and iso-scalar surfaces of sensible enthalpy and of total enthalpy at various stages of ignition. (a) $t^* = 0.2$ for Case 3 ( $T_0' = 60K$ ), (b) $t^* = 0.6$ for Case 3 ( $T_0' = 60K$ ), (c) $t^* = 0.99$ for Case 3 ( $T_0' = 60K$ ), (d) $t^* = 0.2$ for Case 4 ( $T_0' = 100K$ ), (e) $t^* = 0.6$ for Case 4 ( $T_0' = 100K$ ), and (f) $t^* = 0.99$ for Case 4 ( $T_0' = 100K$ ). The magenta contour lines represent iso- $h_t$ surfaces, while the black ones represent iso- $h_s$ surfaces . . . . .	65
4.3 Conditional mean and r.m.s. fluctuations of (a) temperature and (b) fuel mass fraction for Case 4 ( $T_0' = 100K$ ) at $t^* = 0.99$ (red solid lines: conditional mean based on sensible-enthalpy conditioning, blue dashed-dotted lines: conditional mean based on total-enthalpy conditioning, error bars: conditional r.m.s. fluctuations) . . . . .	66
4.4 Scatter plot and conditional means for heat release rates for Case 4 ( $T_0' = 100K$ ) at $t^* = 0.955$ (black dashed-dotted line: CMCh <sub>t</sub> , black circles: DNS data with total-enthalpy conditioning, red solid line: CMCh <sub>s</sub> , red diamonds: DNS data with sensible-enthalpy conditioning; small blue and green circles represent the scatter data for heat release rates plotted in the normalized total enthalpy coordinate and in the normalized sensible enthalpy coordinate, respectively) . . . . .	67
4.5 Normalized conditional mean heat release rates for Case 1 ( $T_0' = 15K$ ) at (a) $t^* = 0.2$ , (b) $t^* = 0.6$ , and (c) $t^* = 0.99$ ; Case 3 ( $T_0' = 60K$ ) at (d) $t^* = 0.2$ , (e) $t^* = 0.6$ , and (f) $t^* = 0.99$ ; and Case 4 ( $T_0' = 100K$ ) at (g) $t^* = 0.2$ , (h) $t^* = 0.6$ , and (i) $t^* = 0.99$ (blue circles: DNS data with total-enthalpy conditioning, blue dashed-dotted lines: CMCh <sub>t</sub> , red diamonds: DNS data with sensible-enthalpy conditioning, red solid lines: CMCh <sub>s</sub> ) . . . . .	68

4.6 Conditional mean reaction rates of H <sub>2</sub> O <sub>2</sub> for Case 1 ( $T_0' = 15K$ ) at (a) $t^* = 0.2$ , (b) $t^* = 0.6$ , and (c) $t^* = 0.99$ ; Case 3 ( $T_0' = 60K$ ) at (d) $t^* = 0.2$ , (e) $t^* = 0.6$ , and (f) $t^* = 0.99$ ; and Case 4 ( $T_0' = 100K$ ) at (g) $t^* = 0.2$ , (h) $t^* = 0.6$ , and (i) $t^* = 0.99$ (blue circles: DNS data with total-enthalpy conditioning, blue dashed-dotted lines: CMCh <sub>t</sub> , red diamonds: DNS data with sensible-enthalpy conditioning, red solid lines: CMCh <sub>s</sub> ) . . . . .	70
4.7 Conditional mean reaction rates of OH for Case 1 ( $T_0' = 15K$ ) at (a) $t^* = 0.2$ , (b) $t^* = 0.6$ , and (c) $t^* = 0.99$ ; Case 3 ( $T_0' = 60K$ ) at (d) $t^* = 0.2$ , (e) $t^* = 0.6$ , and (f) $t^* = 0.99$ ; and Case 4 ( $T_0' = 100K$ ) at (g) $t^* = 0.2$ , (h) $t^* = 0.6$ , and (i) $t^* = 0.99$ (blue circles: DNS data with total-enthalpy conditioning, blue dashed-dotted lines: CMCh <sub>t</sub> , red diamonds: DNS data with sensible-enthalpy conditioning, red solid lines: CMCh <sub>s</sub> ) . . . . .	71
4.8 Mapping curve for PDF and conditional SDR modeling. (a) Case 1 ( $T_0' = 15K$ ) at $t^* = 0.2$ , (b) $t^* = 0.6$ , and (c) $t^* = 0.99$ . (d) Case 3 ( $T_0' = 60K$ ) at $t^* = 0.2$ , (e) $t^* = 0.6$ , and (f) $t^* = 0.99$ . (g) Case 4 ( $T_0' = 100K$ ) at $t^* = 0.2$ , (h) $t^* = 0.6$ , and (i) $t^* = 0.99$ (red solid lines: original mapping curve $\eta_t - \eta_s$ , green squares: modified mapping curve $\eta'_t - \eta'_s$ ) . . . . .	73
4.9 Mapping curve and conditional fluctuations. (a) Case 1 ( $T_0' = 15K$ ) at $t^* = 0.6$ , and (b) $t^* = 0.99$ . (c) Case 4 ( $T_0' = 100K$ ) at $t^* = 0.6$ , and (d) $t^* = 0.99$ . . . . .	74
4.10 Effects of differential diffusion on the mapping curve. (a) Case 3 ( $T_0' = 60K$ ) at $t^* = 0.6$ , (b) Case 4 ( $T_0' = 100K$ ) at $t^* = 0.2$ , and (c) Case 4 ( $T_0' = 100K$ ) at $t^* = 0.6$ (red solid lines: mapping curve $\eta_t - \eta_s$ , blue dashed lines: mapping curve $\eta_t - \eta_s$ from the corresponding DNS cases with the unity Lewis number assumption – Cases 5 and 6) . . . . .	74

4.11 PDF of sensible enthalpy and total enthalpy for Case 1 ( $T_0' = 15K$ ) at (a) $t^* = 0.2$ , (b) $t^* = 0.6$ , and (c) $t^* = 0.99$ ; Case 3 ( $T_0' = 60K$ ) at (d) $t^* = 0.2$ , (e) $t^* = 0.6$ , and (f) $t^* = 0.99$ ; and Case 4 ( $T_0' = 100K$ ) at (g) $t^* = 0.2$ , (h) $t^* = 0.6$ , and (i) $t^* = 0.99$ (blue circles: total-enthalpy PDF from DNS, blue dashed-dotted lines: beta PDF for total enthalpy, red diamonds: sensible-enthalpy PDF from DNS, red solid lines: modeled sensible-enthalpy PDF using total-enthalpy PDF from DNS, green dashed lines: modeled sensible-enthalpy PDF using beta PDF for total-enthalpy) . . . . .	76
4.12 Comparison of the PDFs of sensible enthalpy predicted by the two different approaches, Eqs. (4.6) and (4.9), for Case 4 ( $T_0' = 100K$ ) at (a) $t^* = 0.6$ and (b) $t^* = 0.99$ (red diamonds: sensible-enthalpy PDF from DNS; green dashed lines: modeled PDF using modified mapping, Eq. (4.6), and DNS PDF for total-enthalpy; blue solid lines: modeled PDF using equal-distribution assumption, Eq. (4.9), and DNS PDF for total-enthalpy) . . . . .	77
4.13 Conditional dissipation rates of sensible enthalpy for (a) Case 1 ( $T_0' = 15K$ ) at $t^* = 0.6$ , (b) Case 3 ( $T_0' = 60K$ ) at $t^* = 0.6$ , (c) Case 4 ( $T_0' = 100K$ ) at $t^* = 0.6$ , (d) Case 1 ( $T_0' = 15K$ ) at $t^* = 0.99$ , (e) Case 3 ( $T_0' = 60K$ ) at $t^* = 0.99$ , and (f) Case 4 ( $T_0' = 100K$ ) at $t^* = 0.99$ . (red diamonds: DNS, red solid lines: mapping method) . . . . .	78
4.14 Time evolution of total heat release rates for (a) Case 1 ( $T_0' = 15K$ ), (b) Case 3 ( $T_0' = 60K$ ), and (c) Case 4 ( $T_0' = 100K$ ) (red diamonds: DNS, magenta dotted lines: CMCh <sub>t</sub> integrated using the beta PDF for total enthalpy, blue dashed-dotted lines: CMCh <sub>t</sub> integrated using the total enthalpy PDF from DNS data, red solid lines: CMCh <sub>s</sub> integrated using the sensible enthalpy PDF obtained using the mapping method and the beta PDF for total enthalpy, red short-dashed lines: CMCh <sub>s</sub> integrated using the sensible enthalpy PDF obtained using the mapping method and the total enthalpy PDF from DNS data, green long-dashed lines: CMCh <sub>s</sub> integrated using the sensible enthalpy PDF from DNS data) . . . . .	80
4.15 Temperature and heat release rate (HRR) evolution for Case 4, 7, and 8. . . . .	83

4.16 Temperature fields and iso-scalar surfaces of sensible enthalpy and of total enthalpy at various stages of ignition for Case 7. (The magenta contour lines represent iso- $h_t$ surfaces, while the black ones represent iso- $h_s$ surfaces.) . . . . .	84
4.17 Conditional mean and conditional fluctuations of temperature at $t^* = 0.99$ (red solid lines: CMChs, blue dashed-dotted lines: CMCh <sub>t</sub> , error bars: conditional fluctuations). . . . .	88
4.18 Conditional mean heat release rates at $t^* = 0.99$ (blue circles: DNS data with total-enthalpy conditioning, blue dashed-dotted lines: CM-Ch <sub>t</sub> model, red diamonds: DNS data with sensible-enthalpy conditioning, red solid lines: CMChs model). . . . .	89
4.19 PDF of sensible enthalpy and enthalpy for Case 7 at $t^* = 0.6$ (left), and $t^* = 0.99$ (right). (blue circles: DNS data with total-enthalpy conditioning, blue dashed-dotted lines: presumed Beta PDF for enthalpy, red diamonds: DNS data with sensible-enthalpy conditioning, red solid lines: mapping-approach modeled PDF for sensible enthalpy.) . . . . .	90
4.20 Conditional dissipation rates of sensible enthalpy for Case 7 at $t^* = 0.6$ (left), and $t^* = 0.99$ (right). (red diamonds: DNS data with sensible-enthalpy conditioning, red solid lines: mapping-approach modeled conditional SDR for sensible enthalpy.) . . . . .	90
5.1 In-cylinder equivalence ratio (top) and its probability distribution at TDC (bottom) in RANS. . . . .	97
5.2 Relation of enthalpy $h_t$ and the equivalence ratio $\phi$ for the iso-octane/air mixture at different temperature. . . . .	102
5.3 Slopes of the $h_t-\phi$ curves as a function of the temperature for the iso-octane/air mixture. . . . .	103
5.4 Pressure and specific internal energy fields at the time of knocking. . . . .	104

5.5 Pressure evolution showing the ignition delays for the 2-D constant volume ignition cases. (a) $P_0 = 20$ bar. (b) $P_0 = 30$ bar. (c) $P_0 = 40$ bar. (d) $P_0 = 50$ bar (Black circles: 121 species, green dashed lines: 13 species with the fuel-mass-fraction-based progress variable for deficit mass deposition, blue dashed lines: 7 major species with the fuel-based progress variable for deficit mass deposition, red solid lines: 7 major species with the heat-released-based progress variable for deficit mass deposition). . . . .	110
5.6 Surface geometry of the GM GDI engine used in the LES. . . . .	112
5.7 Isotherm for temperature of 1500 K, colored by the end-gas index function $H(c_\psi^* - \tilde{c}_\psi)$ for one LES cycle (Cyc8). In the end-gas region $H(c_\psi^* - \tilde{c}_\psi)$ is 1.0, otherwise it is 0.0. The isotherm of 1500 K is chosen to represent the flame fronts of the premixed flame and the ignition fronts of the end-gas auto-ignition. End-gas auto-ignition occur at multiple locations at 24 CAD aTDC, as indicated by the red isotherm. The view is in the positive $z$ direction, from piston to the cylinder head.	118
5.8 Temperature (left) and fuel mass fraction (right) fields at 24 CAD aTDC for Cyc8. The black lines are contours of the progress variable, $\tilde{c}_\psi$ , of 0.001. In the burned region, $\tilde{c}_\psi = 1.0$ . In the end-gas region, $\tilde{c}_\psi < 0.001$ . The region beyond the black contours towards the liner walls are the end-gas region. The fields are on a cut-plane in the $z$ direction, showing two auto-ignition locations in the end-gas. . . . .	119
5.9 Pressure fields at 20 CAD aTDC and at 25 CAD aTDC for Cyc8. End-gas auto-ignition first occurs at 21 CAD aTDC for Cyc8. At 20 CAD aTDC, the magnitude of the pressure variation on the cut-plane is 0.5 bar. At 25 CAD aTDC, the magnitude of pressure oscillations is 2.0 bar. When the pressure oscillation amplitudes exceed 1 bar, it is considered as a knocking cycle in the ORNL experiments. . . . .	120

5.10 In-cylinder pressure evolution in consecutive multicycle LES with total-enthalpy-based CMC for R018 (thin gray lines: measured 50 cycles cylinder pressure randomly selected from 5000 cycles in the ORNL experiment R018, black dashed-dotted lines: fastest and slowest cycles in the experiment, black lines with triangles: 5% and 95% bounds from 5000 cycles in the experiment, thick colored lines: pressure from fifteen consecutive LES cycles). The measured 50 cycles cylinder pressure randomly selected from 5000 cycles in the ORNL experiment R018 are shown in the right figure to display the pressure oscillation amplitudes in experiment. . . . .	121
5.11 Comparison of the measured cylinder pressure from one cycle of engine experiments (grey) and the probed pressure from one cycle of multicycle LES (cyan). . . . .	121
5.12 In-cylinder pressure evolution for selected cycles for cases R018-R020. The prediction is from consecutive multicycle LES with total-enthalpy-based CMC (thin gray lines: measured 50 cycles cylinder pressure randomly selected from 5000 cycles in the ORNL experiments, black dashed-dotted line: fastest and slowest cycles in the experiment, black lines with triangles: 5% and 95% bounds from 5000 cycles in the experiment, thick colored lines: pressure from selected consecutive LES cycles). In the figures at the right side, only measured pressure curves are shown to better present the amplitude of the pressure oscillations in the experiment. . . . .	123
5.13 Effects of the exhaust valve temperature on knock occurrence in selected consecutive LES cycles (thin gray lines: measured 50 cycles cylinder pressure randomly selected from 5000 cycles in the ORNL experiment, black dashed-dotted lines: fastest and slowest cycles in the experiment, black lines with triangles: 5% and 95% bounds from 5000 cycles in the experiment, thick colored lines: probed pressure from selected consecutive LES cycles; the total-enthalpy-based CMC knock model is used). . . . .	126

# **Chapter 1: Introduction**

## **1.1 Motivation and Significance**

Despite the fast development of electric propulsion technology, IC engines will remain the major powertrain for vehicles in the next few decades [52, 96]. As the emission regulations become more stringent and the concern on the depletion of fossil fuel agglomerates, the development of advanced IC engine technologies is of significant importance. The major focuses for the development of advanced IC engines are on improving the fuel economy and reducing the emissions, which include NO<sub>x</sub>, CO<sub>2</sub> and unburned hydrocarbons (UHC). To achieve these, promising technologies like the HCCI, further increasing the compression ratio, and the gasoline engine downsizing are being applied in the automotive industry. Over the past decades, significant progresses in the above advanced IC engine technologies have been made. However, further advancing these technologies is facing some major barriers. For HCCI engines, controlling the ignition timing to achieve optimal efficiency is one of the principle challenges [121]. For SI engines with advanced downsizing technique or high compression ratios, preventing engine knock to avoid performance reduction and engine damage is one of the key limitations.

The HCCI engine is regarded as an effective alternative to the traditional IC engines due to its great potential in increasing the thermal efficiency and reducing NO<sub>x</sub> and soot emissions [156, 121]. In the HCCI engine, the fuel-air mixtures are premixed and the charge auto-ignites as it is compressed. The HCCI engine operates at higher compression ratio than traditional SI engines, which is one of the major reasons contributing to the improvement of the thermal efficiency over SI engines [121]. Besides, the HCCI engine operates under fuel lean conditions or with large amounts of exhaust gas recirculation (EGR). Therefore, the maximum combustion temperature in HCCI engines is lower than that in traditional IC engines, which leads to the reduction of the NO<sub>x</sub> emission [156, 121]. In addition, the premixing of the charge in HCCI engines also leads to more complete combustion than that in traditional diesel engines, which reduces the soot emissions compared with diesel engines [121]. Over the past decades, significant progress in the development of HCCI engines has been made [121]. However, the development of effective HCCI engines is still constrained by some key challenges. Controlling the ignition timing is one of the principle challenges limiting the advancement of HCCI technology [156, 104, 121, 5].

The gasoline engine downsizing is a promising technology to improve the fuel economy and to reduce the CO<sub>2</sub> emission [106]. After downsizing, the engine displacement volume can be reduced by around 40% [22], and the reduction can be even more with extreme downsizing technologies. Through the downsizing of the engine, the weight of the engine and the friction loss can be reduced, which contribute to the improvement of the specific fuel consumption (SFC). In addition, the SFC for the downsized engine can be further reduced when operated at partial load conditions due to a decrease of the pumping loss. The improvement of the SFC leads to the

improvement of the fuel economy and the reduction of CO<sub>2</sub> emission. In order to output the same amount of power as the large-size naturally-aspirated engine does, the downsized engine needs to run with air boosting technology [76]. With a turbocharger or a supercharger to compress the air, more air can be breathed into the cylinder under high load conditions. Therefore, the maximum power output from a downsized engine can be maintained as that of a normal-sized engine does. Over the past decades, downsizing the IC engine is one of the major trends in developing advanced engine technology. However, the development of advanced IC engines with further downsizing is facing some major obstacles. Engine knock is one of the major challenges restricting further downsizing.

It is generally accepted that knock in SI engines originates from the auto-ignition of the end-gas, which refers to the unburned mixtures in SI engines before the consumption by premixed flame fronts [123, 59, 53]. Figure 1.1 shows the auto-ignition spots in the end-gas region visualized using laser-induced fluorescence (LIF) imaging technique. Several spots in the end-gas auto-ignite before the consumption by premixed flame fronts, which leads to the occurrence of knock. The boosting of air in downsized SI engines leads to the increase of the temperature and pressure in the cylinder. And further increasing the compression ratio, which is a straightforward practice to increase the thermal efficiency in IC engines, also leads to the increase of the temperature and pressure in the cylinder. Under higher temperature and pressure, the auto-ignition of the end-gas happens faster, and the probability of knock occurrence will be higher. The occurrence of knock not only undermines the engine performance, but also leads to potential engine damage, noise, and pollutant

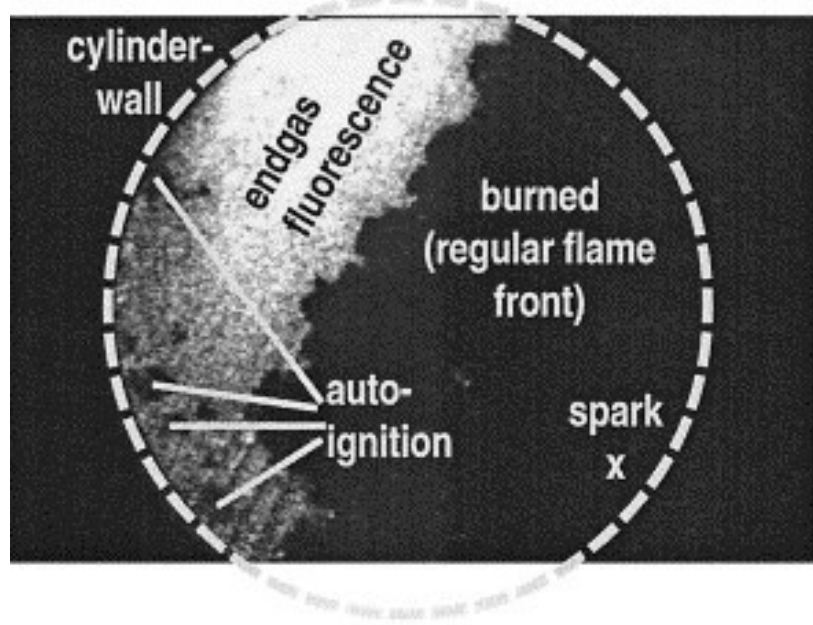


Figure 1.1: Laser-induced fluorescence (LIF) image of auto-ignition spots in a knocking cycle. The figure is taken from [123].

emissions. Therefore, further increasing the compression ratio in IC engines and the downsizing of SI engines are restricted by knock.

The control of the charge ignition in HCCI engines and the prevention of the end-gas auto-ignition in SI engines require further understanding of the ignition of premixed mixtures in IC engines. The experimental research using optical measurement techniques on the charge ignition in HCCI engines [99, 36, 35, 40] and the end-gas auto-ignition in SI engines [59, 123] have advanced the understanding of ignition phenomena in IC engines. The ignition of premixed hydrocarbon fuel-air mixtures is dominated by complex chemical kinetics consisting of hundreds or thousands of species, and is affected by the in-cylinder turbulence. The computational research on the ignition of premixed mixtures in IC engines using high fidelity combustion

models can offer more details on ignition phenomena such as the species evolution and the turbulence-chemistry interaction [114]. The computational research on the ignition of premixed mixtures in IC engines is regarded as an effective alternative to the experimental research [80].

In the computational research on the ignition of premixed mixtures in IC engines, the development of models that can predict the ignition delay accurately and efficiently is the major focus. In the modelling of the ignition of hydrocarbon fuels in IC engines, detailed or reduced chemical mechanisms are required to capture the low temperature kinetics [80, 28]. The LES, which resolves the large-scale unsteady flows and reproduces the cycle-to-cycle variations (CCV) [118, 143], is an attractive method to study knock in SI engines [114, 116] and charge ignition in HCCI engines [56]. The development of high fidelity models that employs complex chemical kinetics, captures the turbulence-chemistry interaction, and can be applied in LES cost-effectively is of significant importance in the computational research on the ignition of premixed mixtures.

The moment closure methods have been widely used in the computational research on turbulent flows [67, 14]. In the moment closure methods, first moments are means and second moments are variances and covariances about the means. The equations for any level of moments have unclosed terms involving higher moments, which are modeled by lower moments to achieve closure. The moment closure methods have proved to be very useful in predictions for a wide range of flows in turbulent non-reacting flows [67]. However, the application of the methods in reacting flow problems may not be satisfactory due to the highly non-linear reaction rate terms and large fluctuations about the moments. Klimenko [66] and Bilger [14] proposed the CMC

method independently for turbulent reacting flow problems. The primary hypothesis for the CMC method is that the fluctuations of reacting scalars are strongly correlated with those of one key quantity, which will be the conditioning variable. The conditional fluctuations are expected to be much smaller than the unconditional ones, which contributes to the accurate modeling of the reaction rate terms. The CMC method [14, 67] has been successfully applied to non-premixed combustion [65, 151]. The research on extending the CMC model to the combustion of premixed mixtures has also been reported [136, 92, 139, 7, 120, 119, 145]. The focus of this thesis is to extend the CMC method to the ignition of premixed mixtures in IC engines, more specifically, to the charge ignition in HCCI engines and end-gas auto-ignition in SI engines.

The CMC method has been applied in the modeling of combustion in diesel engines [34, 124, 17, 16]. In the diesel engines the combustion is non-premixed, and the mixture fraction is taken as a conditioning variable in the CMC. Paola et al. [34] used a 3-D CMC model coupled with Reynolds averaged Navier Stokes (RANS) simulations to study the combustion in a diesel engine under different loads and engine speeds. They also compared the volume-integrated CMC models, in which the 3-D CMC is simplified to 2-D and 0-D CMC models, with the 3-D CMC model and reported promising results with the integrated CMC models. Seo et al. [124] used a spatially-integrated CMC model coupled with RANS to study the combustion in a diesel engine operated in partial homogeneous charge compression ignition (pHCCI) mode. Bolla et al. [16] used a 2-D CMC model coupled with RANS to study the soot formation in a diesel engine under different operating conditions. Recently, Salehi et al. [120] proposed a CMC model for the ignition of premixed heptane-air mixtures

with temperature inhomogeneity, where enthalpy is taken as a conditioning variable. Their results show that the predicted ignition delays are in good agreement with the DNS data for cases with low levels of temperature inhomogeneity under HCCI conditions. However, for high levels of temperature inhomogeneity, the underprediction of ignition delays was observed. Salehi et al. [119] proposed a doubly-conditioned CMC model, where the scalar dissipation rate is taken as the second conditioning variable in addition to enthalpy, and reported improved prediction for the ignition delays for HCCI cases with high levels of temperature inhomogeneity.

The prediction of the ignition of premixed mixtures in IC engines is one of the key challenges in the development of advanced IC engine technologies. The previous works suggest that the CMC method has significant potential in modeling the ignition of premixed mixtures in IC engines accurately and cost-efficiently. However, the CMC method with one conditioning variable can be improved to accurately predict the ignition delays under HCCI conditions with high levels of temperature inhomogeneity. And the application of the CMC method in the modeling of knock in SI engines has not been reported. This study aims at developing a CMC method that provides accurate prediction of the ignition delays under HCCI conditions with high levels of temperature inhomogeneity, and under SI engine knocking conditions. In addition, this study will also explore the capability of the CMC method in the prediction of knock in a GDI engine.

## 1.2 Scope and Objectives of the Research

The overall goal of this thesis research is to extend the CMC method to the ignition of homogeneous fuel/air mixtures with temperature inhomogeneity in HCCI and SI

engines. To achieve this goal, a sensible-enthalpy-based CMC model is developed, together with closure models for the mixing statistics of sensible enthalpy. 2-D DNS of ignition under HCCI and SI engine knocking conditions are performed to validate the sensible-enthalpy-based CMC model and a total-enthalpy-based formulation on the closure of conditional mean reaction rates. A method to apply the CMC model in the prediction of knock in SI engines using LES is developed. Multicycle LES of knock in a GDI engine is conducted with the spatially-integrated total-enthalpy-based CMC model and the results are compared with data from engine experiments. Specifically in this thesis work, the following objectives are accomplished:

- A CMC model based on sensible enthalpy is developed for the ignition of premixed mixtures with temperature inhomogeneity. The ignition of premixed mixtures in IC engines is governed by complex chemical kinetics, which show strong nonlinear-dependence on temperature. Using sensible enthalpy as a conditioning variable, which is strongly correlated with temperature, the conditional fluctuations of temperature are expected to be small throughout the ignition process. As a result, the estimation of the reaction rates can be made accurate. The accurate prediction of the reaction rates also requires closure of the conditional scalar dissipation rate (SDR) and the probability density function (PDF) of the conditioning variable, which is a challenge for the CMC method based on sensible enthalpy. A mapping method is proposed to model these mixing statistics of sensible enthalpy.
- CMC models based on sensible enthalpy and total enthalpy are assessed on the prediction of ignition of premixed mixtures under HCCI and SI engine knocking conditions. 2-D DNS of the ignition of homogeneous PRF-air mixtures with

temperature inhomogeneity in fuel lean and stoichiometric conditions are conducted. The ignition of fuel-lean and stoichiometric mixtures correspond to the charge ignition under HCCI conditions and the end-gas auto-ignition under SI engine knocking conditions, respectively. The enthalpy-based CMC models are assessed through *a priori* analysis using the DNS data. The assessment focuses on the closure of the mean reaction rate, and the closure of the conditional SDR and PDF of sensible enthalpy. The assessment serves as a preliminary validation of the enthalpy-based CMC methods on the prediction of ignition of premixed mixtures in IC engines.

A method to apply the CMC model in the prediction of knock in SI engines is developed. The occurrence of knock in SI engines originates from the end-gas auto-ignition before the consumption by premixed flame fronts. The prediction of knock requires accurate prediction of the end-gas auto-ignition and the premixed flame propagation. The end-gas auto-ignition is modeled by the CMC model. For the prediction of knock in SI engines, the CMC model is coupled with a commercial software, CONVERGE, which is responsible for solving the flow fields. In the coupling, a method to reduce the computational cost by solving a subset of species in the flow solver is proposed. Multicycle LES of knocking cases in a GDI engine is conducted using CONVERGE and the spatially-integrated total-enthalpy-based CMC model. The LES results are compared with data from Oak Ridge National Laboratory (ORNL) engine experiments to validate the coupling and the spatially-integrated total-enthalpy-based CMC model on the prediction of knock in SI engines. The effects of the spark timing retarding and wall temperature on the occurrence of knock are investigated.

### 1.3 Organization of this Thesis

The rest of this thesis is organized as follows. In Ch. 2, a literature review on the ignition of the premixed mixtures in HCCI and SI engines and the models for the ignition processes is presented. In Ch. 3, the CMC method for turbulent reacting flows is described and its applications in non-premixed and premixed combustion are summarized. The enthalpy-based CMC models for the ignition of premixed mixtures with temperature inhomogeneity are presented. The advantage and challenge of using sensible enthalpy as the conditioning variable over using total enthalpy are discussed. In Ch. 4, the enthalpy-based-CMC models for the ignition of premixed mixtures are validated using DNS data. 2-D DNS of ignition of homogeneous PRF-air mixtures with temperature inhomogeneity under both HCCI and SI engine knocking conditions are conducted. The DNS data are used to validate the enthalpy-based CMC models through *a priori* analysis. The validation focuses on the closure of conditional reaction rates and the closure of the conditional SDR and PDF of sensible enthalpy. In Ch. 5, the method to apply the CMC model in the prediction of knock in SI engines is presented. And a method to reduce the computational cost by solving a subset of species in the flow solver is developed. Multicycle LES of reference knocking cases in a GDI engine is performed with CONVERGE and the spatially-integrated total-enthalpy-based CMC model. The LES results are compared with experimental data to validate the coupling method and the total-enthalpy-based CMC model on knock prediction. In Ch. 6, the contributions of this work are summarized and future works are discussed.

## **Chapter 2: Literature Review on the Ignition of Premixed Mixtures in IC Engines**

In this chapter, a literature review on the ignition of the premixed mixtures in HCCI and SI engines and the models for the ignition processes is presented.

### **2.1 Ignition of Homogeneous Fuel/Air Mixtures in IC Engines**

#### **2.1.1 Charge Ignition in HCCI Engines**

In traditional IC engines, the ignition of the fuel-air mixtures can be accurately controlled by the engine control unit (ECU) [51]. In SI engines, the ignition is controlled by the spark discharge timing. In compression ignition (CI) engines, the ignition is controlled by the fuel spray injection timing. However, in HCCI engines, the ignition of the charge is governed by the chemical kinetics and is affected by the in-cylinder inhomogeneity (especially temperature inhomogeneity) and turbulence-chemistry interaction. The control of the ignition timing in HCCI engines is one of the major challenges [156, 8, 134, 104, 121].

The HCCI engine operates under fuel lean conditions or with large amounts of EGR. In HCCI engines, the charge is mixed homogeneously when the fuel is injected

early in the intake stroke [131, 98, 124]. Chemical reactions happen in the homogeneous charge, which eventually lead to the auto-ignition at multiple locations in the cylinder [113, 8, 5]. The ignition processes in HCCI engines are governed by the chemical kinetics [113, 134, 69, 5]. For lower octane rating fuels such as heptane and diesel, a peculiar two-stage ignition phenomenon is observed under HCCI conditions [113, 8, 134, 69, 111, 128, 121]. The first stage of ignition is associated with the low temperature kinetics [69, 134, 111, 121], and cool flames are observed through optical measurements [113, 8]. The second stage of ignition characterize the onset of the main combustion phase [69], releasing most of heat. For higher octane rating fuels such as iso-octane and ethanol, a single-stage ignition is observed under HCCI conditions [111, 128, 121].

In HCCI engines, inhomogeneity in temperature field exists [27, 36, 35, 40, 50], and has significant effect on the ignition process [129, 130, 127, 83, 50, 121]. The temperature inhomogeneity can come naturally from wall heat transfer [36, 35, 40, 50]. Dec and coworkers used chemiluminescence [36] and planar laser induced fluorescence (PLIF) [35, 40] to study the development of thermal stratification in HCCI engines. Dronniou and Dec [40] reported temperature r.m.s. fluctuations in their HCCI engine to be around 20K at the top dead center (TDC) and continue to rise during the expansion stroke. The temperature inhomogeneity can also be enhanced artificially [126, 121] using delayed direct injection or EGR. Introducing thermal stratification is a promising strategy to control the ignition timing and to limit the maximum heat release rate (HRR) in HCCI engines [129, 130, 127, 83, 50, 121]. Sjöberg and coworkers [130, 127] investigated the effect of thermal stratification on spreading the

HR<sub>R</sub> and on the control of ignition timing and combustion phasing in HCCI engines using a multi-zone model and experimental data. The thermal stratification can lead to different reaction progress in the charge and may result in sequential auto-ignition [121]. Yoo and coworkers [154, 90] used 2-D DNS to study the effect of thermal stratification on the ignition delays of PRF fuels under HCCI conditions. Ignition delays were found to decrease as the thermal stratification levels increase, and negative temperature coefficient (NTC) effect was observed in their cases. The inhomogeneity in the mixture composition field can also be introduced by using delayed direction injection to control the ignition timing [121]. The discussion of the effect of introduced mixture inhomogeneity on the ignition in HCCI engines can be found in the review of HCCI engines research [121] and is beyond the scope of this thesis.

The ignition processes in HCCI engines are also found to be affected by the in-cylinder turbulence [25, 71] and the turbulence-chemistry interaction when inhomogeneities exist [69, 70, 154, 5]. The in-cylinder turbulence can affect the ignition in HCCI engines by altering temperature and charge mixing, boundary layer thickness, and wall heat transfer [25, 71]. Christensen and Johansson [25] studied the effect of in-cylinder flow and turbulence on the HCCI operation using experiments. They reported that the combustion duration, CO emission, and wall temperature were affected by the in-cylinder turbulence. Kong and Reitz [71] studied the effect of piston geometry-generated turbulence on HCCI combustion using RANS. They reported that the flow turbulence affects the HCCI combustion mainly through wall heat transfer. In addition, the chemical reactions controlling the ignition in HCCI

engines can be affected by turbulent mixing directly [69, 70]. The use of kinetics-controlled models which neglect this turbulence-chemistry interaction usually leads to very fast combustion rates [69]. Kong and coworkers [69, 70] used a multi-zone model coupled with RANS to study the combustion in HCCI engines under different operating conditions. The ignition of the charge was modeled by modified kinetics-controlled detailed chemistry models, in which a turbulent timescale was introduced to account for the turbulence-chemistry interaction. Yoo et al. [154, 90, 91] used 2-D DNS to study the effect of turbulence-chemistry interaction on the ignition under HCCI conditions with temperature inhomogeneity.

### 2.1.2 End-gas Auto-ignition in SI Engines

In SI engines, further increasing the compression ratio contributes to the improvement of thermal efficiency. Besides, engine downsizing with charge boosting contributes to the improvement of fuel economy and reduction of CO<sub>2</sub> emission. However, further increase of the compression ratio and the downsizing of SI engines are restricted by knock.

The SI engine operates under near-stoichiometric conditions, putting the diluted mixture operation aside. In SI engines, the fuel can enter the cylinder through the intake ports with air in port fuel injection (PFI), or enter the cylinder directly through the injector in GDI engines. The fuel-air mixture has a sufficient time to mix when the injection happens early in the intake stroke [135]. In the combustion stroke, a spark is discharged and an ignition kernel is developed from the spark. The ignition kernel then develops to turbulent flame fronts, which propagate in the cylinder and consume the unburned fuel-air mixture. In normal combustion cycles, all the

unburned mixtures are consumed by the premixed flame fronts and the cylinder pressure evolves smoothly as shown in Fig. 2.1(a). However, the unburned mixture ahead of the premixed flame fronts, which is referred to as the end-gas, is undergoing chemical reactions and may auto-ignite before premixed flame fronts come to its location. When the end-gas auto-ignition happens, a substantial amount of heat is released rapidly, which generates strong oscillating pressure waves in the cylinder [51]. This is an abnormal combustion phase in the SI engine operations, which is referred to as knocking combustion [51]. The pressure oscillations in knocking combustion cycles are shown in Fig. 2.1(b).

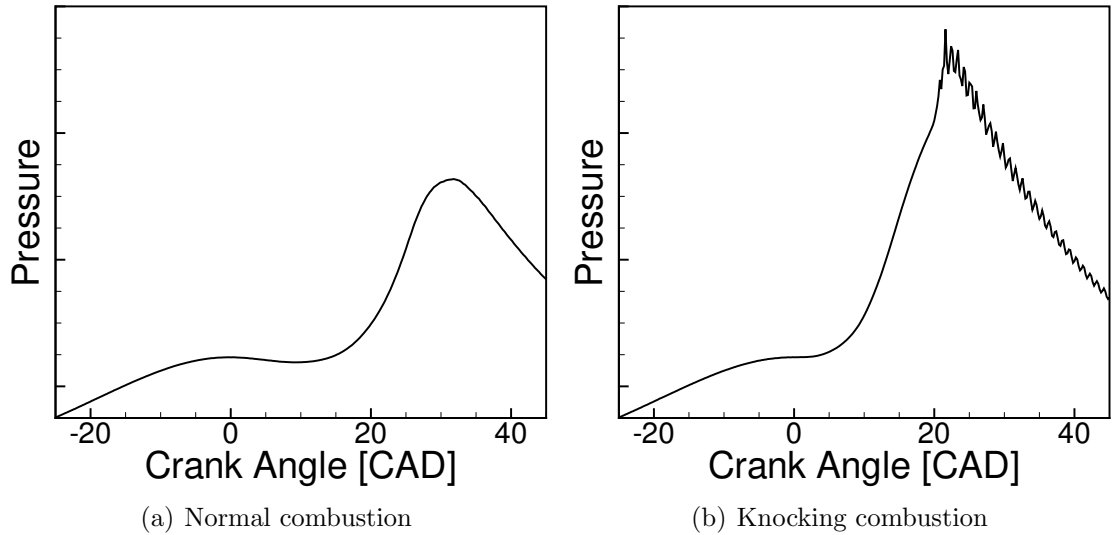


Figure 2.1: In-cylinder pressure traces for normal and knocking combustion cycles.

Knock or knocking is a terminology in the IC engine community referring to the noise caused by the resonance of oscillating in-cylinder pressure waves and metallic structures in the engine cylinder [51]. The abnormal combustion of the end-gas in

knocking cycles leads to reduction in the thermal efficiency [51, 77] and extra CO and NO<sub>x</sub> emissions [77]. Besides, in intense knocking cycles, the maximum pressure may exceed the designed limit of the cylinder, which undermines the engine durability.

It is generally accepted that the auto-ignition of the end-gas is the cause of knock in SI engines [51, 123, 59, 53]. The compression from the propagation of the premixed flame fronts and the piston motion towards the TDC raise the pressure and temperature of the end-gas. Under elevated pressure and temperature, the end-gas may ignite before the premixed flame fronts propagate to its location. Increasing the compression ratio and boosting the charge in downsized SI engines lead to the increase of temperature and pressure in the cylinder, which increase the probability of knock. Therefore, further increasing the compression ratio and downsizing of SI engines are restricted by knock.

Similar to the ignition of homogeneous charge in HCCI engines, the auto-ignition of end-gas in SI engines is governed by the chemical kinetics [148, 78, 59, 47, 146]. Westbrook [148] examined the chemical kinetic factors of hydrocarbon oxidation in a variety of ignition problems, including the charge ignition in HCCI engines and end-gas auto-ignition in SI engines. Two major chain-branching regimes were identified in the ignition of hydrocarbon fuels. Kawahara et al. [59] observed the two-stage ignition phenomena of n-butane in an optically-accessible SI engine using high-speed video camera. Griffiths et al. [47] observed the two-stage ignition phenomena of n-pentane in a rapid compression machine using chemiluminescence. For fuels showing two-stage ignition phenomena in SI engines, a NTC regime is prominent in the ignition delay times plot [146]. In the NTC regime, for given pressure the ignition delay times increase with the increase of initial temperature.

The auto-ignition of end-gas in SI engines can also be affected by the temperature inhomogeneity [123, 47] and by the in-cylinder turbulence and turbulence-chemistry interaction [146, 147]. Schiessl and Maas [123] investigated the spacial thermal stratification in the end-gas using LIF and reported the thermal stratification exceeding 20 K in the nominally homogeneous end-gas for their engine. Griffiths et al. [47] studied the effects of temperature inhomogeneity and fuel reactivity on the controlled auto-ignition through experiments in a rapid compression machine. Wei et al. [147] studied the effect of turbulence-chemistry interaction in the end-gas auto-ignition under SI engine knocking conditions using LES and a 1-D linear eddy model (LEM). In their work, the pressure evolution due to the premixed flame propagation and end-gas auto-ignition matched qualitatively with experimental data in a rapid compression machine. The effect of turbulence-chemistry interaction on the end-gas auto-ignition was then investigated by extracting data from LES and performing a parametric study using the LEM model. In the parametric study, a linear temperature gradient was prescribed near the boundary and the turbulence intensities were varied.

## 2.2 Models for Ignition in HCCI engines and End-gas Auto-ignition in SI Engines

Depending on how the in-cylinder inhomogeneities and turbulence are treated, the models for the combustion in IC engines can be generally categorized into zero-dimensional models, quasi-dimensional models, and multidimensional models [95, 82]. In the zero-dimensional models, or so-called zone models [95, 82, 3], each zone is considered as a perfectly stirred reactor where zero-dimension assumption is applied. In the zone models, thermodynamic and mixture states are averaged within the chamber (single-zone models) or within individual zones (multi-zone models). The effects of

the in-cylinder inhomogeneities and turbulence on the ignition are neglected within zones under the zero-dimension assumption. In the quasi-dimensional model, a flame front is introduced to separate the burned and unburned zones [95, 142]. In the burned and unburned zones, zero-dimension assumption is applied and the effects of the in-cylinder inhomogeneities and turbulence on the ignition are neglected. The multidimensional modeling of IC engines can be categorized into RANS and LES. In the multidimensional models, the effects of the in-cylinder inhomogeneities and turbulence on the ignition can be considered by the mixing and turbulence models. The effect of turbulence-chemistry interaction on the ignition may also be considered by turbulent combustion models.

In the modeling of combustion in IC engines using multidimensional models, chemistry models that describe the hydrocarbon oxidation need to be used to model the ignition of premixed mixtures. In the multidimensional models, chemistry models can be used directly to model the ignition of premixed mixtures. In these models, the ignition of premixed mixtures is assumed to be controlled by chemical kinetics only, and the turbulence-chemistry interaction is neglected [69]. Kong et al. [69] introduced a turbulent timescale into the detailed chemistry model to account for the turbulence-chemistry interaction in the ignition of premixed mixtures empirically. To model the effect of the turbulence-chemistry interaction on the ignition of premixed mixtures, turbulent combustion models such as the flamelet model [29], the CMC model [120, 145], and the transported PDF model [72, 15, 155] can be used in the multidimensional modeling framework.

Since the ignition of premixed mixtures is governed by the chemical kinetics, the development of chemistry models by increasing the complexity of species and reactions is one of the major focuses in the development of models for the ignition. In this section, the development of the chemistry models for the ignition of premixed mixtures is firstly reviewed, and the application of the chemistry models in multi-dimensional models and zone models for IC engines, which neglect the turbulence-chemistry interaction, are introduced. Then, models for the ignition that account for the turbulence-chemistry interaction are reviewed, and their applications are introduced.

### 2.2.1 Chemistry Models

#### 2.2.1.1 Empirical Correlations

Livengood and Wu [88] proposed an integral method based on empirical correlations for the ignition delay to model the ignition of premixed mixtures. In the integral method, the ignition delay of the process can be modeled by

$$\int_{t=0}^{t=t_c} \frac{1}{\tau} dt = 1, \quad (2.1)$$

where  $t_c$  is the time ignition happens, i.e. the ignition delay of the ignition process.  $\tau$  is the ignition delay under constant pressure and temperature at each time step.  $t$  is the time coordinate. The ignition delay under constant pressure and temperature is approximated by an empirical correlation based on the global Arrhenius reaction rate:

$$\tau = Ap^{-n} \exp\left(\frac{B}{T}\right), \quad (2.2)$$

where  $A$ ,  $n$ , and  $B$  are empirical model constants,  $p$  and  $T$  are the pressure and temperature at each time step. The model constants are carefully fitted with experimental data to reproduce the ignition delay under different thermodynamic conditions. Douaud and Eyzat [39] modified the empirical correlation by introducing a fuel-dependent term into the model constant  $A$ :

$$A = A_1 \left( \frac{OCTN}{100} \right)^{A_2}, \quad (2.3)$$

where OCTN is the volumetric percentage of iso-octane in the PRF fuels,  $A_1$  and  $A_2$  are empirical model constants.

Due to the simplicity, the integral method based on empirical correlations have been widely used in the modeling of end-gas auto-ignition in SI engines [53, 37] and have been extended to modeling ignition in HCCI engines as well [37]. However, the empirical correlations can not capture the NTC effect in ignition problems. Therefore, the integral method using empirical correlations can not predict the ignition delay accurately when the NTC effect is prominent [37]. A detailed review on the ignition modeling using the integral method can be found in [37].

### 2.2.1.2 Simplified Chemistry Models

To capture the low temperature kinetics in the ignition of premixed mixtures in IC engines, models based on the chemistry of hydrocarbon oxidation were developed [122]. Halstead et al. [48, 49] proposed a simplified chemistry model, the Shell model, which consists of five generic species and eight generalized chain reactions for the hydrocarbon oxidation. In the Shell model, the low temperature kinetics in the ignition can be captured by the chain reactions, including the chain initiation,

propagation, branching, and termination, and by carefully fitting the kinetic parameters [49, 122]. Schapertons and Lee [122] used the the Shell model in a 2-D modeling of knock and reported good predictions of knock tendencies compared with data collected from rapid compression machines. Eckert et al. [42] used the Shell model to predict occurrences of knock in an SI engine using RANS. Good agreement with experimental data on the predictions of knock occurrences under different engine speeds was reported. Kong et al. [68] applied the Shell model to study the charge ignition in HCCI engines using RANS.

Recently, Misdariis et al. [93] proposed a two-step chemistry model for the modeling knock in IC engine using LES. The two-step chemistry model includes a global reaction of hydrocarbon and a reversible reaction between CO and CO<sub>2</sub>. The two reactions in the model followed the Arrhenius form. The pre-exponential constant in the global reaction was varied between two constants,  $A_{AI}$  and  $A_{prop}$ , depending on the mixture temperature. With the varying pre-exponential constant and the carefully fitted kinetics constants based on experimental data, the two-step chemistry model can reproduce both the laminar flame speed and the auto-ignition delay. The reversible reaction was added to reproduce the adiabatic flame temperature. Misdariis et al. [94] used the two-step chemistry model with the thickened flame for LES (TFLES) model to study the effect of wall heat transfer on knock in an SI engine.

### 2.2.1.3 Detailed/Reduced Chemistry Models

To model the ignition of premixed mixtures under wide ranges of operating conditions in IC engines, reduced or detailed chemical mechanisms have been developed and used in the modeling of ignition [149, 11, 152]. The detailed chemical mechanisms usually consist of over hundreds of species and involve over several hundreds of

reactions. The ignition delay and laminar flame speeds calculated from the detailed chemical mechanisms are validated against experimental data collected in shock tubes under wide ranges of thermodynamic conditions. The reduced chemical mechanisms usually consist of over tens of species and are developed from detailed chemical mechanisms by conducting chemistry sensitivity study [152]. The ignition delay and laminar flame speeds calculated from the reduced chemical mechanisms are validated against results from detailed chemical mechanisms or from experimental data.

Detailed or reduced chemistry models have been used in multidimensional models to study the ignition of premixed mixtures. Liang et al. [80] used a reduced chemical mechanism for the ignition of iso-octane/air mixtures in the RANS of knock in an SI engine. Shao and Rubland [125] proposed a knock propensity criterion based on HO<sub>2</sub> concentration through the RANS study of knock with reduced chemical mechanism.

The effect of turbulence-chemistry interaction on the ignition is neglected by using chemistry models directly for the mean reaction rate approximation in the multidimensional modeling of engines. To account for the turbulence-chemistry interaction, a simple method was proposed by Kong and coworkers [69, 70, 71] by introducing a turbulent timescale into the detailed chemistry model. In their model, the reaction rate for species  $i$  is written as

$$\omega_i = \frac{Y_i^* - Y_i}{\tau_{kin,i} + f\tau_{turb}}, \quad (2.4)$$

where  $Y_i$  and  $Y_i^*$  are the current concentration and equilibrium concentration of species  $i$ , respectively.  $\tau_{kin,i}$  is the kinetic timescale of species  $i$ , which is evaluated from the detailed chemistry model.  $\tau_{turb}$  is the turbulent timescale defined by the eddy turn over time, which is approximated by  $\frac{Ck}{\varepsilon}$ .  $C$  is a model constant,  $k$  and  $\varepsilon$  are the turbulent kinetic energy and its dissipation rate, respectively.  $f$  is a progress variable.

Kong and coworkers [69, 70, 71] used this simple modification to the detailed chemistry model to study the ignition in HCCI engines using RANS.

Multidimensional CFD with reduced or detailed chemistry models can provide accurate prediction of the ignition delay in a wide ranges of operation conditions in IC engines. However, due to the restriction of the computational cost, reduced or detailed chemistry models are usually used in the RANS to study the ignition problems in IC engines.

#### 2.2.1.4 Tabulated Kinetics Ignition Model

To retain the benefits of using detailed chemical kinetics in the modeling of ignition and to reduce the computational cost in multidimensional CFD, tabulated kinetics ignition (TKI) models have been used for the study of ignition of premixed mixtures. Pires da Cruz [31] proposed a tabulation method under the integral method framework to model the ignition in HCCI and diesel engines. In the tabulation method, the ignition delay database was created *a priori* using detailed chemistry calculation with the temperature, pressure, equivalence ratio, and residual gas percentage as the inputs. The local delay in each cell at each time step during the simulation was interpolated from the ignition delay database. Then the integral method was used to model the local auto-ignition. Colin et al. [28] improved the tabulation method and proposed a TKI model for the charge ignition in HCCI engines. The tabulated ignition delay model lead to overestimation of the auto-ignition delay when low temperature heat release is prominent [28]. In the TKI model, the cool flame heat release and the chemical progress rate were added into the ignition delay database. The cool flame delay was still modeled using the integral method. After the cool flame delay, the

reaction progress was modeled by the chemical progress rate, which was interpolated from the database.

The TKI models have been used for the study of knock in SI engines [75, 45, 44, 114, 116, 41] and charge ignition in HCCI engines [28, 141]. Truffin and Colin [141] studied the effect of thermal stratifications on the ignition in HCCI engines using the TKI model. Breda et al. [20] and Chevillard et al. [24] employed the TKI model in RANS to study knock in GDI engines. Lecocq et al. [75] and Fontanesi et al. [45] conducted qualitative studies of knock tendency on engine speed and spark timing using the TKI model. Fontanesi et al. [44] investigated the effect of electrodes orientation and spark plug position on CCV and knock with the TKI model. Robert et al. [114] used the TKI model and demonstrated that LES is able to predict the in-cylinder pressure variability, knock occurrence frequency and onset of knock by comparing with experimental data. Robert et al. [115] used the TKI model in LES to study the super knock in a downsized SI engine.

### 2.2.2 Multizone Models

In the zone models, the effects of inhomogeneities, turbulence, and turbulence-chemistry interaction on the ignition in each zones are neglected. The ignition of premixed mixtures in each zones is assumed to be controlled by chemical kinetics only. The development of the models for the ignition of premixed mixtures under the zone model framework is mainly focused on increasing the complexity of the chemistry models.

Bradley and coworkers [19, 18] used the empirical correlation by Douaud and Eyzat [39] in a single-zone model to study auto-ignition under IC engine conditions.

Chen et al. [23] modified the empirical correlation to consider the EGR effect on the ignition and used in a two-zone model to predict knock in SI engines.

Detailed or reduced chemistry models have been used in the zone models to study the ignition of premixed mixtures. Leppard [78] and Westbrook et al. [149] adopted the detailed chemical mechanisms in single-zone models to study the end-gas auto-ignition under SI engine knocking conditions. Single-zone models employing detailed chemical kinetics were also used to study the charge ignition in HCCI engines [132, 26, 4]. Ferguson et al. [43] used the detailed chemical kinetics in a two-zone model to study knock in an SI engine. Li et al. [79] used reduced chemical kinetics in a two-zone model to study the heat release in an SI engine. In the modeling of charge ignition in HCCI engines, multi-zone models with detailed or reduced chemical kinetics were used [153, 3, 2, 1, 9, 10]. Xu et al. [153] compared the ignition modeling using a six-zone model and a single-zone model in an HCCI engine and reported significant improvements in matching with test data when using the multi-zone model.

Aceves and coworkers [3, 2, 1] developed a multi-zone model that can be coupled in RANS to account for the turbulent mixing before the ignition in HCCI engines. In their multi-zone model, the mixing, diffusion, and heat transfer are not considered between zones. Babajimopoulos et al. [9] and Barth et al. [10] developed fully coupled multi-zone models with RANS to study the ignition in HCCI engines. In their multi-zone model, at each time step, the the multi-zone model and RANS flow solver are two-way coupled. Recently, Pal et al. [102] used a multi-zone model coupled with RANS to study knock in a cooperative fuel research (CFR) engine. In their multi-zone model, a reduced chemical mechanism for the end-gas auto-ignition was used.

### 2.2.3 Transport Probability Density Function Model

To account for the turbulence-chemistry interaction in the ignition problems in IC engines, transport PDF models have been used [72, 15, 155]. In the PDF method, a transport equation for the joint PDF of the reactive scalars is solved [72, 15]. Kraft et al. [72] proposed a transported PDF model based on the stochastic reactor model for ignition in HCCI engines, in which the PDF is assumed to be spatially homogeneous. Bhave [12] applied a spatially homogeneous PDF model in the study of ignition in an HCCI engine with EGR. Bisetti et al. [15] used a spatially homogeneous PDF model to study the ignition under HCCI conditions with thermal stratification. They compared the results from the PDF model with DNS data and investigated the performance of three mixing models in the transport PDF method. Zhang et al. [155] proposed a fully transported PDF model and studied the effect of turbulence-chemistry interaction on the ignition in HCCI engines. In their work, the joint PDF of forty species and enthalpy was solved. They reported that the turbulence-chemistry interaction effect is non-negligible in low swirl cases, and that effect becomes increasing important as the swirl increases. Linse et al. [84] and D'Adamo et al. [32, 33] proposed a PDF model to account for the CCV and stochastic feature of knock in SI engines.

### 2.2.4 Enthalpy-Based Flamelet Model

Cook and Pitsch [29] developed an enthalpy-based flamelet model for the charge ignition in HCCI engines. In HCCI engines, stratification in enthalpy field develops due to the wall heat transfer, and the stratification is expected to affect the ignition in HCCI engines [29]. In the enthalpy-based flamelet model, the transport equations for the species mass fractions in physical space are transformed to the system aligned

with enthalpy gradients. In their model, enthalpy is the total enthalpy containing the sensible and chemical parts. Cook et al. [30] used the enthalpy-based flamelet model to study the charge ignition in HCCI engines with thermal inhomogeneity and reported superior performance over the multi-zone models.

### 2.2.5 Total-Enthalpy-Based Conditional Moment Closure Model

Recently, Salehi et al. [120] proposed a CMC model for the ignition of premixed heptane-air mixtures with temperature inhomogeneity under HCCI conditions. In their work, total enthalpy is taken as a conditioning variable. With the primary closure hypothesis in CMC [67, 14] and homogeneous mixture assumption, the total-enthalpy-based CMC leads to a similar formulation to the enthalpy-based flamelet model. The turbulence-chemistry interaction is accounted for in CMC through the conditional SDR term and the resolution of the species concentration in the conditioning variable space. In their work, the total-enthalpy-based CMC model was assessed *a posteriori* using 2-D DNS of ignition under HCCI conditions. The total-enthalpy-based CMC model showed good predictions of the ignition delay for cases with low levels of thermal stratification. However, large conditional fluctuations were observed for cases with high levels of thermal stratification (100 K), which lead to underpredictions of the ignition delay. Salehi et al. [119] proposed a doubly-conditioned CMC model, where the scalar dissipation rate is taken as the second conditioning variable in addition to enthalpy, and reported improved prediction for the ignition delays for HCCI cases with high levels of temperature inhomogeneity.

## Chapter 3: Conditional Moment Closure Method for Ignition of Premixed Mixtures with Temperature Inhomogeneity

In this chapter, the CMC method for the ignition of premixed mixtures in IC engines with temperature inhomogeneity is described. In Sec. 3.1, the fundamentals of the CMC method for turbulent reacting flows are introduced. The widely used moment closure method for turbulent flow problems is summarized, and its drawback of for turbulent reacting flow problems is discussed. Following the introduction to the CMC method, its major applications in non-premixed and premixed combustion modeling are summarized. In Sec. 3.2, the enthalpy-based CMC models for the ignition of premixed mixtures with temperature inhomogeneity are presented. The advantage and challenge of using sensible enthalpy as the conditioning variable over using total enthalpy are discussed.

### 3.1 CMC Method for Turbulent Reacting Flows

#### 3.1.1 Governing Equations

The governing equations for turbulent reacting flow problems are given by the conservation of mass, momentum, energy, and species [108].

- Conservation of mass

$$\frac{\partial \rho}{\partial t} + \frac{\partial(\rho u_i)}{\partial x_i} = 0, \quad (3.1)$$

where  $\rho$  is the density,  $u_i$  and  $x_i$  are the velocity and coordinate component of direction  $i$ , respectively.  $t$  is the time coordinate.

- Conservation of momentum

$$\frac{\partial(\rho u_j)}{\partial t} + \frac{\partial(\rho u_i u_j)}{\partial x_i} = -\frac{\partial p}{\partial x_j} + \frac{\partial \tau_{ij}}{\partial x_i} + \rho \sum_{k=1}^N Y_k f_{k,j}, \quad (3.2)$$

where  $p$  is the static pressure,  $Y_k$  is the mass fraction of species  $k$ ,  $f_{k,j}$  is the volumetric body force acting on species  $k$  in the  $j$  direction,  $N$  is the number of species.  $\tau_{ij}$  is the viscous stress tensor, and for Newtonian fluids it follows,

$$\tau_{ij} = -\frac{2}{3}\mu \frac{\partial u_k}{x_k} \delta_{ij} + \mu \left( \frac{\partial u_i}{\partial x_j} + \frac{\partial u_j}{\partial x_i} \right), \quad (3.3)$$

where  $\mu$  is the dynamic viscosity,  $\delta_{ij}$  is the Kronecker delta.

- Conservation of Energy

With the low Mach number assumption, Fick's law for the species molecular diffusion, and the unity Lewis number assumption (molecular diffusion coefficients for all the species equal the thermal diffusion coefficient), the conservation of energy in terms of enthalpy can be written as,

$$\frac{\partial(\rho h)}{\partial t} + \frac{\partial(\rho u_i h)}{\partial x_i} = \frac{\partial p}{\partial t} - \frac{\partial}{\partial x_i} \left( \rho D \frac{\partial h}{\partial x_i} \right) + \dot{Q}, \quad (3.4)$$

where  $D$  is the thermal diffusion coefficient,  $\dot{Q}$  is the energy source term due to radiation.  $h$  is the enthalpy of the mixture defined as,

$$h = \sum_{k=1}^N Y_k h_k = \sum_{k=1}^N Y_k \left( \Delta h_{f,k}^\circ + \int_{T_0}^T C_{pk} dT \right), \quad (3.5)$$

where  $h_k$  is the enthalpy of species  $k$ ,  $C_{pk}$  is the specific heat of species  $k$ , at constant pressure.  $\Delta h_{f,k}^\circ$  and  $\int_{T_0}^T C_{pk} dT$  are the enthalpy of formation and sensible enthalpy of species  $k$ , respectively.

- Conservation of Species Mass

Using Fick's law for the species molecular diffusion, the conservation equation for the species mass can be written,

$$\frac{\partial(\rho Y_k)}{\partial t} + \frac{\partial(\rho u_i Y_k)}{\partial x_i} = \frac{\partial}{\partial x_i} \left( \rho D_k \frac{\partial Y_k}{\partial x_i} \right) + \dot{\omega}_k, \quad (3.6)$$

where  $Y_k$  is the mass fraction of species  $k$ ,  $D_k$  is the diffusion coefficient of species  $k$  into the rest of the mixture.  $\dot{\omega}_k$  is the reaction rate of species  $k$ .

The reaction rate term in Eq. (3.6) is the net production or consumption rate of species  $k$ . To get its mathematical form, let's assume the reactions can be represented by a chemical system of  $N$  species reacting with  $M$  reactions as,

$$\sum_{k=1}^N \nu'_{kj} \mathcal{M}_k \rightleftharpoons \sum_{k=1}^N \nu''_{kj} \mathcal{M}_k \quad \text{for } j = 1, M. \quad (3.7)$$

where  $\mathcal{M}_k$  is the chemical symbol of species  $k$ ,  $\nu'_{kj}$  and  $\nu''_{kj}$  are the molar stoichiometric coefficients of species  $k$  in reaction  $j$ . Then the reaction rate of species  $k$  is written as,

$$\dot{\omega}_k = \sum_{j=1}^M (\nu''_{kj} - \nu'_{kj}) \left( K_{fj} \prod_{k=1}^N (\rho Y_k)^{\nu'_{kj}} - K_{rj} \prod_{k=1}^N (\rho Y_k)^{\nu''_{kj}} \right), \quad (3.8)$$

where  $K_{fj}$  and  $K_{rj}$  are the forward and reverse rate constants of reaction  $j$ , respectively. Following the Arrhenius law, the forward reaction rate constant of reaction  $j$  is written as,

$$K_{fj} = A_{fj} T^{\beta_j} \exp \left( -\frac{T_{aj}}{T} \right), \quad (3.9)$$

where  $A_{fj}$  is the pre-exponential constant,  $\beta_j$  is the temperature exponent,  $T_{aj}$  is the activation temperature. The reverse reaction rate constant  $K_{rj}$  can then be obtained through a chemical equilibrium calculation [108].

In the numerical research on the turbulent reacting flow problems, the aforementioned governing equations are solved. In general, the methods to solve the governing equations can be categorized as: Reynolds Averaged Navier Stokes (RANS), Large Eddy Simulation (LES), and Direct Numerical Simulation (DNS) [108].

For DNS, the instantaneous governing equations are solved directly, without any models for the turbulent fluxes or chemical reactions. The smallest length and time scales are resolved, and all the flow information in the domain are obtained. DNS can be regarded as a ‘numerical experiment’, and can provide detailed data for validating other models. However, in order to resolve the smallest length and time scales in turbulent reacting flows, DNS requires tremendous amount of computational resources. The turbulent flow problems involve wide range of length scales, and the ratio between the largest length scale and the smallest scale is proportional to the Reynolds number of the problem. The chemical reactions in turbulent reacting flow problems add more complexity to discussion of the length and time scales. The smallest chemical length and time scales can be much smaller than the smallest turbulent scales in some conditions. Therefore, due to its demanding computational cost, the application of DNS is still restricted to problems with low Reynolds number, or with simplified geometries, or with simplified chemical schemes in turbulent reacting flows.

For LES, the governing equations are filtered and solved in the filtered form. The filtering process is essentially a spatial-averaging process, and only the length scales above the LES filter size are resolved. Generally in the LES, the large scale eddies that are dependent on the geometry of the problem are resolved, while the smallest scales that display universal behavior are not resolved [108]. In the filtered form of the governing equations, there are unclosed terms, the sub-grid flux terms and filtered

chemical reaction terms, which require modeling. The detailed introduction to the subgrid-scales (SGS) models used in the LES can be found in [108]. The closure of these terms based on the idea of the widely used moment closure method will be summarized below. LES has been widely used in the academic field on the research of turbulent reacting flows, and is receiving more and more attention on the application to engineering problems.

For RANS, the governing equations are ensemble-averaged and solved in the averaged form. Due to the averaging operation, there are unclosed terms in the averaged governing equations: the turbulent flux terms and averaged chemical reaction terms, which require modeling. The detailed introduction to the turbulence models used in the RANS can be found in [108]. RANS has been widely used in the industry on the modeling of turbulent reacting flow problems.

### 3.1.2 Moment Closure Method

In the study of turbulent non-reacting and reacting flows, the moment closure methods have been widely used [81]. In the moment closure methods, first moments are means, second moments are variances and covariances about the means. The equations for any level of moments have unclosed terms involving higher moments, which are modeled by lower moments to achieve closure.

In LES, the governing equations are filtered. In variable density reacting flows, the Favre filtering of a variable  $f$  is often used:

$$\bar{\rho}\tilde{f}(\mathbf{x}) = \int \rho f(\mathbf{x}') F(\mathbf{x} - \mathbf{x}') d\mathbf{x}', \quad (3.10)$$

where  $\mathbf{x}$  represents the spatial coordinates,  $\rho$  and  $\bar{\rho}$  are the density and averaged density, respectively.  $F(\mathbf{x})$  is the LES filter function. In the Favre-filtering, a filtered quantity is weighted by density, which leads to the equations similar to those obtained for constant density flows. After the filtering, the instantaneous variable  $f$  is decomposed into the Favre filtered part and the sub-grid part as,

$$f = \tilde{f} + f'', \quad (3.11)$$

where  $\tilde{f}$  is the Favre filtered part.  $f''$  is the sub-grid part, which is the unresolved fluctuation about the filtered quantity.

Applying the Favre filtering operation to the governing equations in Sec. 3.1.1, and if the body force and the external energy source terms can be neglected, the governing equations in the filtered form can be written as [108]:

- Conservation of mass

$$\frac{\partial \bar{\rho}}{\partial t} + \frac{\partial (\bar{\rho} \tilde{u}_i)}{\partial x_i} = 0, \quad (3.12)$$

where  $x_i$  is the coordinate component of direction  $i$ ,  $t$  is the time coordinate.

$\tilde{u}_i$  is the filtered velocity of direction  $i$ .

- Conservation of momentum

$$\frac{\partial (\bar{\rho} \tilde{u}_j)}{\partial t} + \frac{\partial (\bar{\rho} \tilde{u}_i \tilde{u}_j)}{\partial x_i} = -\frac{\partial \bar{p}}{\partial x_j} + \frac{\partial \bar{\tau}_{ij}}{\partial x_i} + \frac{\partial}{\partial x_j} \bar{\rho} (\widetilde{u_i u_j} - \widetilde{u_i} \widetilde{u_j}), \quad (3.13)$$

where  $\bar{p}$  is the filtered pressure,  $\bar{\tau}_{ij}$  is the filtered viscous stress tensor.  $\bar{\rho} (\widetilde{u_i u_j} - \widetilde{u_i} \widetilde{u_j})$  are the sub-grid stresses.

- Conservation of energy

$$\frac{\partial (\bar{\rho} \tilde{h})}{\partial t} + \frac{\partial (\bar{\rho} \tilde{u}_i \tilde{h})}{\partial x_i} = \frac{\partial \bar{p}}{\partial t} - \frac{\partial}{\partial x_i} \overline{\left( \rho D \frac{\partial h}{\partial x_i} \right)} + \frac{\partial}{\partial x_i} \bar{\rho} (\widetilde{u_i h} - \widetilde{u_i} \widetilde{h}), \quad (3.14)$$

where  $\tilde{h}$  is the filtered enthalpy,  $\bar{\rho} (\widetilde{u_i h} - \widetilde{u}_i \widetilde{h})$  are the sub-grid enthalpy fluxes.

- Conservation of species mass

$$\frac{\partial(\bar{\rho}\widetilde{Y}_k)}{\partial t} + \frac{\partial(\bar{\rho}\widetilde{u}_i\widetilde{Y}_k)}{\partial x_i} = \frac{\partial}{\partial x_i} \overline{\left( \rho D_k \frac{\partial Y_k}{\partial x_i} \right)} + \frac{\partial}{\partial x_i} \bar{\rho} (\widetilde{u_i Y_k} - \widetilde{u}_i \widetilde{Y}_k) + \bar{\omega}_k, \quad (3.15)$$

where  $\widetilde{Y}_k$  and  $\bar{\omega}_k$  are the filtered specie mass fraction and filtered reaction rate of species  $k$ , respectively.  $\bar{\rho} (\widetilde{u_i Y_k} - \widetilde{u}_i \widetilde{Y}_k)$  are the sub-grid species fluxes.

In LES, the filtered quantities, which are the first order moments of the corresponding instantaneous variables, are resolved. The sub-grid stresses and the sub-grid fluxes involve variances and covariances of the filtered quantities, which are the second order moments. The filtered reaction rate terms also involve higher order moments of the filtered temperature and filtered species mass fractions if assuming the reaction rates follow the Arrhenius form. The terms involve second or higher order moments are unclosed and require modeling. In the moment closure method, these second or higher order moment terms are modeled by the resolved lower moments.

In the moment closure method framework, there are several models for those unclosed terms. Detailed introduction to the specific models is beyond the scope of this work. The following summary of the closure models for the unclosed terms serves only as a demonstration of the moment closure methodology. More comprehensive discussion of the specific models can be found in [108].

- Sub-grid stresses  $\mathcal{T}_{ij} = \bar{\rho} (\widetilde{u_i u_j} - \widetilde{u}_i \widetilde{u}_j)$

The sub-grid stresses can be modeled using the Smagorinsky subgrid-scale model as,

$$\mathcal{T}_{ij} = -\mu_t \left( \frac{\partial \widetilde{u}_i}{\partial x_j} + \frac{\partial \widetilde{u}_j}{\partial x_i} - \frac{2}{3} \delta_{ij} \frac{\partial \widetilde{u}_k}{\partial x_k} \right) + \frac{1}{3} \delta_{ij} \mathcal{T}_{kk}, \quad (3.16)$$

where  $\mu_t$  is the subgrid-scale dynamic viscosity and can be modeled as

$$\mu_t = \bar{\rho} C_S \Delta^2 |\tilde{S}|. \quad (3.17)$$

$\mathcal{T}_{kk}$  can be modeled as

$$\mathcal{T}_{kk} = 2\bar{\rho} C_I \Delta^2 |\tilde{S}|^2. \quad (3.18)$$

In Eq. (3.17) and Eq. (3.18),  $C_S$  and  $C_I$  are two model parameters,  $\Delta$  is the LES filter size.  $\tilde{S}_{ij}$  is the filtered shear stress as  $\tilde{S}_{ij} = \frac{1}{2} \left( \frac{\partial \tilde{u}_i}{\partial x_j} + \frac{\partial \tilde{u}_j}{\partial x_i} \right)$ . Its norm is defined as  $|\tilde{S}| = \left( 2\tilde{S}_{ij}\tilde{S}_{ij} \right)^{1/2}$ .

- Sub-grid scalar fluxes  $\bar{\rho} \left( \widetilde{u_i \phi} - \widetilde{u_i} \widetilde{\phi} \right)$

The sub-grid fluxes of scalar  $\phi$ , which can be enthalpy  $h$  or species mass fraction  $Y_k$ , can be modeled with the gradient assumption as,

$$\bar{\rho} \left( \widetilde{u_i \phi} - \widetilde{u_i} \widetilde{\phi} \right) = - \frac{\mu_t}{Sc_\phi} \frac{\partial \widetilde{\phi}}{\partial x_i}, \quad (3.19)$$

where  $Sc_\phi$  is the turbulent Schmidt number of scalar  $\phi$ .

- Filtered reaction rate  $\overline{\dot{\omega}_k}$

To demonstrate how the filtered reaction rate is closed using low-order moments in the moment closure method, the modeling of the filtered reaction rate of the fuel in a one-step irreversible reaction is presented below. The one-step irreversible reaction between fuel (F) and oxidizer (O) takes the form:



Assuming the reaction rate of the fuel follows the Arrhenius law,

$$\dot{\omega}_F = -A\rho^2 T^{\beta_1} Y_F Y_O \exp \left( -\frac{T_A}{T} \right), \quad (3.21)$$

where  $A$  is the pre-exponential constant,  $\beta_1$  is the temperature exponent.  $Y_F$  and  $Y_O$  are the mass fractions of fuel and oxidizer, respectively.  $T_A$  is the activation temperature. Applying the decomposition in Eq. (3.11), the filtered reaction rate term can be expressed using the Taylor series expansion as,

$$\bar{\omega}_F = -A\bar{\rho}^2 \tilde{T}^{\beta_1} \tilde{Y}_F \tilde{Y}_O \exp\left(-\frac{T_A}{\tilde{T}}\right) \left[ 1 + \left(\frac{T_A}{\tilde{T}}\right)^2 \frac{\widetilde{T''^2}}{\widetilde{T^2}} + \frac{\widetilde{Y_F'' Y_O''}}{\widetilde{Y_F Y_O}} + \dots \right]. \quad (3.22)$$

To close the filtered species transport equation, terms with higher order contributions in Eq. (3.22) are neglected:

$$\bar{\omega}_F = -A\bar{\rho}^2 \tilde{T}^{\beta_1} \tilde{Y}_F \tilde{Y}_O \exp\left(-\frac{T_A}{\tilde{T}}\right). \quad (3.23)$$

The closure of the filtered reaction rate using the Taylor series expansion of the Arrhenius form of the reaction rate demonstrates the idea of moment closure method. However, it is not practical to use the first-order Taylor series expansion to achieve closure due to the large truncation errors. Second-order or even higher order of Taylor series expansion need to be used to maintain accuracy. Alternatively, closure can be achieved by using algebraic models.

The moment closure methods have proved to be very useful in predictions for a wide range of flows in turbulent non-reacting flows [67]. However, the application of the methods in reacting flow problems are not satisfying due to the highly non-linear reaction rate terms and large fluctuations of reacting scalars about the first moments. The closure of the mean reaction rate terms are the main objective of turbulent combustion models. The conditional moment closure method for the closure of the mean reaction rate terms in turbulent reacting flows is introduced below.

### 3.1.3 Conditional Moment Closure Method

Klimenko [66] and Bilger [14] proposed the CMC method independently for turbulent reacting flow problems. The primary hypothesis for the CMC method is that the fluctuations of reacting scalars are strongly correlated with those of one key quantity, which will be the conditioning variable. The moments of the reacting scalars are only evaluated at locations where certain conditions are satisfied. The condition in CMC is the conditioning variable takes a certain value. These moments are the conditional moments in CMC, and are functions of the conditioning variable. The fluctuations of the reacting scalars about their conditional moments are the conditional fluctuations. The conditional fluctuations are expected to be much smaller than the unconditional ones under the primary hypothesis, which contributes to the accurate modeling of the mean reaction rate terms.

Figure 3.1 is used to illustrate the process of conditional averaging, and the expectation that the conditional fluctuations are smaller than unconditional ones. The schematic shows the scatter plot of temperature and the mixture fraction, and the conditionally averaged temperature profile conditioning on the mixture fraction in a non-premixed combustion problem. The maximum temperature is at locations where the mixture is stoichiometric and the mixture fraction is  $f_{st}$ . It can be seen that temperature is a non-linear function of the mixture fraction. The fluctuation of temperature about its mean is large, which is the variance of temperature of all the data in the scatter plot. Then, if the range of the mixture fraction is divided into several bins based on its value, the whole data set can be sorted into the bins. Within each bin, the mean of temperature can be evaluated, which is shown by the red solid circle Fig. 3.1. Within each bin, the fluctuation of temperature can also be

evaluated, which is the variance about the mean. Since the mean and fluctuation are evaluated on the condition that the mixture fraction takes a certain value, they are the conditional mean and the corresponding conditional fluctuation. And the mixture fraction is the conditioning variable. It is clear that the conditional fluctuations are smaller than the unconditional fluctuation. The performance of CMC depends on the correlation between the conditioning variable and the reacting scalars. The stronger the correlations is, the smaller the conditional fluctuations are, and the better the closure is.

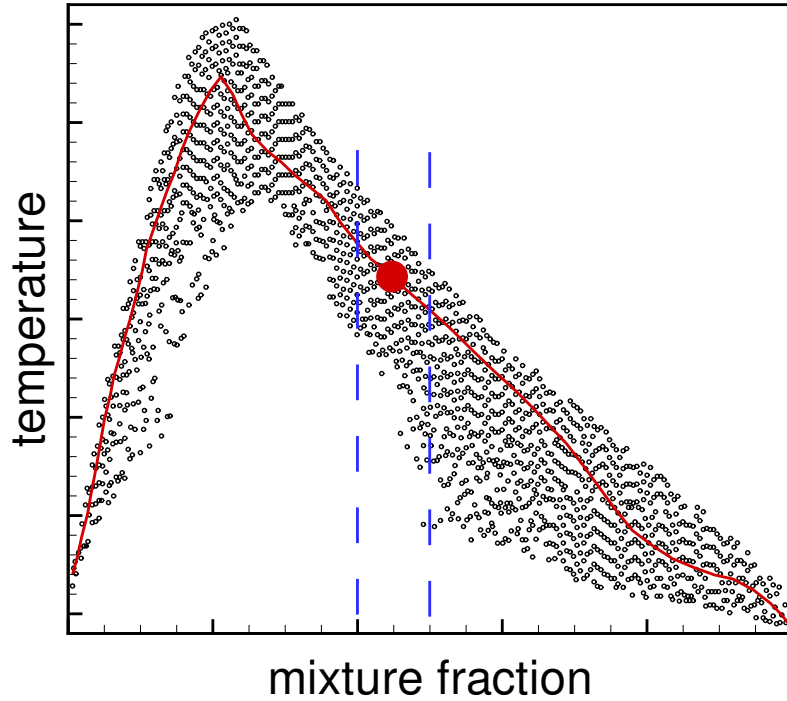


Figure 3.1: Schematic showing the conditional average and fluctuations. Each black circle represents a pair of measured temperature and the mixture fraction. The red solid line shows the temperature averaged with the condition that the mixture fraction takes a particular value. Practically, the conditional average is obtained by taking an average for samples having a certain small range of the mixture fraction, which is represented by the blue dashed lines. The red solid circle is the averaged temperature in that particular bin, i.e. the conditionally averaged temperature. The degree of scatter within the region bounded by the dashed lines represents conditional fluctuations.

The derivation of the CMC equations can either follow a joint PDF method by Klimenko [66] or a decomposition method by Bilger [14]. Here the decomposition method is adopted and the derivation is summarized below.

From Sec. 3.1.1, the transport equation for species mass fraction is

$$\rho \frac{\partial Y_k}{\partial t} + \rho u_i \frac{\partial Y_k}{\partial x_i} = \frac{\partial}{\partial x_i} \left( \rho D_k \frac{\partial Y_k}{\partial x_i} \right) + \dot{\omega}_k. \quad (3.24)$$

The transport equation for the conditioning variable takes the following form:

$$\rho \frac{\partial \xi}{\partial t} + \rho u_i \frac{\partial \xi}{\partial x_i} - \frac{\partial}{\partial x_i} \left( \rho D_\xi \frac{\partial \xi}{\partial x_i} \right) = \dot{S}_\xi, \quad (3.25)$$

where  $\xi$  is the conditioning variable,  $\dot{S}_\xi$  is the source term. When  $\xi$  is a conserved scalar,  $\dot{S}_\xi = 0$ .

In CMC, the density-weighted conditionally filtered scalar is defined as,

$$Q_\phi(\eta; \mathbf{x}, t) = \frac{\int \rho \phi \delta(\xi(\mathbf{x}, t) - \eta) F(\mathbf{x} - \mathbf{x}') d\mathbf{x}'}{\int \rho \delta(\xi(\mathbf{x}, t) - \eta) F(\mathbf{x} - \mathbf{x}') d\mathbf{x}'}, \quad (3.26)$$

where  $\phi$  is a reacting scalar.  $\eta$  is the sample space variable for the conditioning variable,  $\xi$ .  $\delta$  is the Dirac delta function.  $F(\mathbf{x})$  is an LES filter.  $t$  and  $\mathbf{x}$  are the time and space coordinates. To be consistent with the format in literature [67, 14], the following notation is adopted:

$$Q_\phi(\eta; \mathbf{x}, t) = \frac{\langle \rho \phi | \eta \rangle}{\rho_\eta}, \quad (3.27)$$

where the angular brackets denote the LES filtering subject to the condition on the right of the vertical bar,  $\langle () | \eta \rangle \equiv \langle () | \xi(\mathbf{x}, t) = \eta \rangle$  and  $\rho_\eta \equiv \langle \rho | \eta \rangle$ . With this definition, a scalar, such as the mass fraction of species  $k$ ,  $Y_k$  can be decomposed into the conditionally filtered part, i.e. the conditional mean (first-order conditional moment), and its conditional fluctuation:

$$Y_k(\mathbf{x}, t) = Q_k(\eta; \mathbf{x}, t) + y_k(\mathbf{x}, t), \quad (3.28)$$

where  $Q_k(\eta; \mathbf{x}, t)$  and  $y_k(\mathbf{x}, t)$  are the conditional mean species mass fraction of species  $k$  and its conditional fluctuations, respectively. The conditional fluctuations satisfy

$$\langle \rho y_k(\mathbf{x}, t) | \eta \rangle = 0. \quad (3.29)$$

Substituting this decomposition into the time and spacial derivatives of the scalar, we obtain:

$$\frac{\partial Y_k}{\partial t} = \frac{\partial Q_k}{\partial t} + \frac{\partial y_k}{\partial t} + \frac{\partial Q_k}{\partial \xi} \frac{\partial \xi}{\partial t}, \quad (3.30)$$

$$\frac{\partial Y_k}{\partial x_i} = \left( \frac{\partial Q_k}{\partial x_i} + \frac{\partial y_k}{\partial x_i} + \frac{\partial Q_k}{\partial \xi} \frac{\partial \xi}{\partial x_i} \right). \quad (3.31)$$

Here for brevity,  $Q_k(\eta; \mathbf{x}, t)$  and  $y_k(\mathbf{x}, t)$  are written as  $Q_k$  and  $y_k$ , respectively. When we substitute Eqs. (3.30) and (3.31) into the species transport equation Eq.(3.24) and take the conditional averaging, we can get:

$$\begin{aligned} & \rho_\eta \frac{\partial Q_k}{\partial t} + \rho_\eta \langle u_i | \eta \rangle \frac{\partial Q_k}{\partial x_i} - \rho_\eta \langle N_\xi | \eta \rangle \frac{\partial^2 Q_k}{\partial \eta^2} \\ & + \langle \frac{\partial Q_k}{\partial \eta} \left[ \rho \frac{\partial \xi}{\partial t} + \rho u_i \frac{\partial \xi}{\partial x_i} - \frac{\partial}{\partial x_i} \left( \rho D_k \frac{\partial \xi}{\partial x_i} \right) \right] | \eta \rangle = \langle \dot{\omega}_k | \eta \rangle + e_y + e_Q, \end{aligned} \quad (3.32)$$

where  $N_\xi$  is the scalar dissipation rate of the conditioning variable  $\xi$  as  $N_\xi = D_\xi \frac{\partial \xi}{\partial x_i} \frac{\partial \xi}{\partial x_i}$ .

In Eq. (3.32),

$$e_y = - \langle \left( \rho \frac{\partial y_k}{\partial t} + \rho u_i \frac{\partial y_k}{\partial x_i} - \frac{\partial}{\partial x_i} \left( \rho D_k \frac{\partial y_k}{\partial x_i} \right) \right) | \eta \rangle, \quad (3.33)$$

$$e_Q = \langle \left[ \frac{\partial}{\partial x_i} \left( \rho D_k \frac{\partial Q_k}{\partial x_i} \right) + \rho D_k \frac{\partial \xi}{\partial x_i} \frac{\partial}{\partial x_i} \left( \frac{\partial Q_k}{\partial \eta} \right) \right] | \eta \rangle. \quad (3.34)$$

The term  $e_y$  represents the contribution from the turbulent fluctuation  $y_k$ , and can be closed as [14]

$$e_y = - \frac{\nabla \cdot (\langle \rho \mathbf{v} y_k | \eta \rangle P(\eta))}{P(\eta)}, \quad (3.35)$$

where  $\mathbf{v}$  is the conditional fluctuation of the velocity, and  $P(\eta)$  is the PDF of the conditioning variable. It is suggested that in flows without stabilization regions,  $e_y$

can be neglected [14]. The term  $e_Q$  represents the contribution from the molecular diffusion and thus is negligible when Reynolds number is high. In this work, both  $e_y$  and  $e_Q$  are neglected.

With  $e_y$  and  $e_Q$  being neglected, and substituting Eq. (3.25) into Eq. (3.32), the CMC equations become,

$$\frac{\partial Q_k}{\partial t} + \langle u_i | \eta \rangle \frac{\partial Q_k}{\partial x_i} = -v_\eta \frac{\partial Q_k}{\partial \eta} + \langle N_\xi | \eta \rangle \frac{\partial^2 Q_k}{\partial \eta^2} + \frac{\langle \dot{\omega}_k | \eta \rangle}{\rho_\eta}, \quad (3.36)$$

where  $v_\eta$  is the convective velocity in  $\eta$  space and follows

$$v_\eta = \langle \frac{\partial}{\partial x_i} \left( (D_\xi - D_k) \frac{\partial \xi}{\partial x_i} \right) + \frac{1}{\rho} \dot{S}_\xi | \eta \rangle. \quad (3.37)$$

With the unity Lewis number assumption,  $v_\eta$  can be simplified to  $v_\eta = \langle \frac{1}{\rho} \dot{S}_\xi | \eta \rangle$ . After solving the CMC equations, the Favre filtered species mass fraction  $\tilde{Y}_k$  can be obtained as,

$$\tilde{Y}_k = \int_{\eta_{min}}^{\eta_{max}} Q_k \tilde{P}(\eta) d\eta, \quad (3.38)$$

where  $\eta_{min}$  and  $\eta_{max}$  are the minimum and maximum values of the conditioning variable, respectively.  $\tilde{P}(\eta)$  is the Favre PDF of the conditioning variable.

In Eq. (3.36) and Eq. (3.38), the major quantities that require closure models are the conditionally averaged reaction rate term,  $\langle \dot{\omega}_k | \eta \rangle$ , and the mixing statistics of the conditioning variable, including  $N_\xi$  and  $P(\eta)$ .

- Conditionally averaged reaction rate  $\langle \dot{\omega}_k | \eta \rangle$

The conditional fluctuations of reactive scalars are usually much smaller than the unconditional ones. Based on this observation and assuming the conditional fluctuations are negligible, the conditionally averaged reaction rate can be approximated using the first order CMC closure [67],

$$\langle \dot{\omega}_k | \eta \rangle = \dot{\omega}(\rho_\eta, Q_k, Q_T), \quad (3.39)$$

where  $Q_k$  and  $Q_T$  are the density-weighted conditionally filtered species mass fractions and temperature, respectively.

- Mixing statistics of the conditioning variable

The mixing statistics of interest in CMC include the conditional SDR and the PDF of the conditioning variable. The effects of turbulence-chemistry interaction, which refers to the turbulent mixing, chemical reaction, and molecular diffusion interacting with each other in turbulent reacting flows, are accounted for in CMC through the conditional SDR and the resolution of the species concentration in the conditioning variable space.

The mixing statistics of a conserved scalar have been extensively investigated [54, 105, 144]. For the closure of PDF, a presumed PDF, such as the Beta PDF, is often used. The closure of SDR can be achieved by an algebraic model [107] or a dimensional analysis [55]. Unlike a conserved scalar, the modeling of the mixing statistics of a reacting scalar is considered a challenge. The closure of the PDF of a reacting scalar can be achieved by solving its transport equation [57]. And the SDR can be modeled by algebraic models [137]. The discussion on the closure of the PDF and conditional SDR is presented in detail in Sec. 3.2.

### 3.1.4 Applications of CMC in Turbulent Reacting Flows

The CMC method is initially developed for non-premixed combustion [67], where the mixture fraction is usually taken as the conditioning variable. In non-premixed combustion, the mixing between the fuel stream and the oxidizer stream can be characterized by the mixture fraction:

$$f = \frac{\beta - \beta_o}{\beta_f - \beta_o}, \quad (3.40)$$

where  $\beta$  can be the mass fraction of an inert tracer introduced with the fuel [67]. The subscripts  $f$  and  $o$  indicate the fuel stream and the oxidizer stream, respectively. The mixture fraction is an ideal candidate for the conditioning variable. That is because the mixture fraction is closely correlated with other reacting scalars in non-premixed combustion. With the strong correlation the conditional fluctuations are small.

The CMC method has been successfully applied to various non-premixed combustion problems such as the lifted jet flames [117, 64, 97], the bluff-body flame [62, 140], extinction and re-ignition in homogeneous isotropic turbulence [74, 63], spray auto-ignition [151], and combustion in diesel engines [124, 150], etc.

Despite the success in applying the CMC method in non-premixed combustion, fewer studies have been conducted to extend the CMC method to premixed combustion. There are two major challenges when extending the CMC method to premixed combustion. The first challenge is the choice of an appropriate conditioning variable that is closely correlated with the reacting scalars. In non-premixed combustion, the mixture fraction is a natural choice for the conditioning variable [67]. In premixed combustion, several variables that can characterize the reaction progress in different problems have been proposed to be the choice for the conditioning variable, which are described below. The second challenge is the closure of the mixing statistics of the conditioning variable. For problems where the conditioning variable is based on a reacting scalar, its mixing will be significantly affected by the chemical reactions. The PDF and SDR of reacting scalars are qualitatively different from those of a conserved scalar and the closure is challenging.

Swaminathan and Bilger [136] proposed a scaled sensible enthalpy as the conditioning variable as

$$c = \frac{h_s - h_s^u}{h_s^b - h_s^u}, \quad (3.41)$$

where  $h_s$  is sensible enthalpy. Superscript  $u$  and  $b$  indicate the unburned and burned mixture sides, respectively. With the scaled sensible enthalpy, they studied the first-order closure of the conditional reaction rate and various other terms in the CMC equations *a priori* with DNS data for hydrogen/air flames. Martin et al. [92] used a modified scaled sensible enthalpy as the conditioning variable,

$$c = \frac{h_s - h_s^{ad}}{h_s^{ad} - h_s^u}, \quad (3.42)$$

where  $h_s^{ad}$  is the sensible enthalpy at adiabatic equilibrium state. This CMC model was tested on a premixed flame stabilized by a backward-facing step. Thornber et al. [139] used a scaled oxygen mass fraction as the conditioning variable,

$$c = \frac{Y_{O2}^u - Y_{O2}}{Y_{O2}^u - Y_{O2}^b}. \quad (3.43)$$

Their model was applied to model the flame in a lean premixed slot bunsen burner. Amzin et al [7] used a scaled fuel mass fraction as the conditioning variable,

$$c = \frac{Y_f}{Y_f^u}. \quad (3.44)$$

And their work focuses on the conditional mean scalar dissipation rate modeling in premixed flames.

### 3.2 Spatially-Integrated CMC Model for the Ignition of Premixed Mixtures in IC engines

Recently, Salehi et al. [120] proposed a CMC model for the ignition of premixed heptane/air mixtures with temperature inhomogeneity under HCCI conditions. In

their work, enthalpy is taken as a conditioning variable. And because the spacial dependence of the source term in the enthalpy equation is negligible in low Mach number flows, the PDF and SDR of enthalpy can be approximated by models for conserved scalar mixing. In their work, good predictions of the ignition delay are reported for cases with low level of thermal stratification. However, large conditional fluctuations are observed for cases with high levels of thermal stratification (100 K), which lead to underprediction of the ignition delay. Wang and Kim [145] proposed a CMC model for the ignition of premixed mixtures with temperature inhomogeneity for HCCI, where sensible enthalpy is chosen as the conditioning variable. A mapping method was proposed to model the PDF and SDR of sensible enthalpy from those of enthalpy. In their work, the predictions for the conditional heat release rates are improved due to the suppressed conditional fluctuations of temperature. The PDF and conditional SDR are also well captured by the mapping method.

The previous works [120, 119, 145] suggest that the CMC model has significant potential in modeling the ignition of premixed mixtures accurately. Currently, the effort to apply the CMC method in modeling knock in SI engines has not been reported, which is one of the major subjects in this work. In this section, the enthalpy-based CMC models for the ignition of premixed mixtures in IC engines are introduced. The CMC based on enthalpy is referred to as total-enthalpy-based CMC model, and shorted as CMCh<sub>t</sub>. The CMC based on sensible enthalpy is referred to as sensible-enthalpy-based CMC model, and shorted as CMCh<sub>s</sub>. Here total enthalpy, which contains the chemical and sensible parts, is used for enthalpy to differentiate from sensible enthalpy.

As introduced in Ch. 1, knock in SI engines results from the auto-ignition of the end-gas before the consumption by the premixed flame fronts. The term ‘end-gas’ refers to the unburned mixtures ahead of the premixed flame fronts. Therefore, to model the occurrence of knock, both the premixed flame propagation and the end-gas auto-ignition should be correctly modeled. In this work, the modeling of knock occurrence is conducted in the LES context. The propagation of the premixed flame fronts is modeled by a FPF method [61]. And the auto-ignition of the end-gas is modeled by the enthalpy-based CMC methods.

In FPF, the propagation of the flame fronts are tracked by a filtered progress variable  $\tilde{c}_\psi$ , which is 0.0 in the unburned region and 1.0 in the burned region. The end-gas region is the set of locations where the unburned mixtures take up. The end-gas region can be identified using an end-gas index function,  $H(c_\psi^* - \tilde{c}_\psi)$ , where  $H(\tilde{c}_\psi)$  is a Heaviside function and  $c_\psi^*$  is a small value. When  $\tilde{c}_\psi \leq c_\psi^*$ ,  $H(c_\psi^* - \tilde{c}_\psi)$  is 1.0, indicating the end-gas region. Otherwise  $H(c_\psi^* - \tilde{c}_\psi)$  is 0.0. When there is no premixed flame fronts present, for example the charge ignition in HCCI engines and the fuel oxidation before the spark discharge in SI engines,  $H(c_\psi^* - \tilde{c}_\psi)$  is 1.0 in the whole cylinder.

With the end-gas index function, the density weighted conditionally filtered reacting scalar in the end-gas region is defined as,

$$Q_\phi(\eta; \mathbf{x}, t) = \frac{\int \rho \phi \delta(h - \eta) H(c_\psi^* - \tilde{c}_\psi) F(\mathbf{x} - \mathbf{x}') d\mathbf{x}'}{\int \rho \delta(h - \eta) H(c_\psi^* - \tilde{c}_\psi) F(\mathbf{x} - \mathbf{x}') d\mathbf{x}'}, \quad (3.45)$$

where  $h$  is the conditioning variable in the enthalpy-based CMC, and  $\eta$  is the sample space variable for  $h$ . From Sec. 3.1.3, with the primary closure hypothesis and the high Reynolds number assumption, the equations for the conditionally filtered species

mass fractions in the end-gas region are written as

$$\frac{\partial Q_k}{\partial t} + \langle u_i | \eta \rangle \frac{\partial Q_k}{\partial x_i} = -v_\eta \frac{\partial Q_k}{\partial \eta} + \langle N_\xi | \eta \rangle \frac{\partial^2 Q_k}{\partial \eta^2} + \frac{\langle \dot{\omega}_k | \eta \rangle}{\rho_\eta}, \quad (3.46)$$

where  $v_\eta$  is the convective velocity in  $\eta$  space,  $v_\eta$  for CMCh and CMChs will be presented below. The  $\langle () | \eta \rangle$  denotes the LES filtering in the end-gas region subject to the condition on the right side of the vertical bar, as defined in Eq. (3.45). Interfacial terms due to the introduction of the Heaviside function in Eq. (3.46) are also neglected.

For the ignition of premixed mixtures in IC engines, the mixture is assumed to be homogeneously mixed and only the temperature inhomogeneity is considered. The spatial dependence of the mixture composition is negligible under the homogeneous assumption. In CMC, the conditionally filtered quantities have much weaker spatial dependence than their unconditional counterparts [67]. Therefore, the spatial dependence of  $Q_k$  is assumed to be negligible, i.e.  $Q_k(\eta; \mathbf{x}, t)$  becomes  $Q_k(\eta; t)$ . With such an assumption, the transport equations for  $Q_k(\eta; t)$  can be obtained by integrating the CMC equations, Eq. (3.46), over the end-gas region:

$$\frac{\partial Q_k}{\partial t} = -v_\eta^* \frac{\partial Q_k}{\partial \eta} + \langle N_\xi | \eta \rangle^* \frac{\partial^2 Q_k}{\partial \eta^2} + \langle W_k | \eta \rangle, \quad (3.47)$$

where  $Q_k(\eta; t)$  is written as  $Q_k$ , the superscript,  $*$ , denotes the volume-averaged quantity.  $\langle W_i | \eta \rangle$  is the integrated conditionally filtered reaction rate normalized by the total end-gas volume. This method is referred to as the spatially-integrated CMC method in this work.

Under the assumption that the conditional fluctuations of reactive scalars are small, the integrated conditionally filtered reaction rates can be approximated using

the first order CMC [67],

$$\langle W_i | \eta \rangle = \dot{\omega}_i(\rho_\eta, Q_i, Q_T), \quad (3.48)$$

where  $Q_T$  is the conditionally averaged density-weighted temperature.

After solving the conditionally filtered scalars in CMC, the unconditional quantities, i.e. the filtered scalars in LES, in the end-gas region are obtained as

$$\tilde{\phi} = \int_0^1 Q_\phi \tilde{P}(\eta) d\eta, \quad (3.49)$$

where  $\tilde{P}(\eta)$  is the Favre PDF or the filtered density function (FDF) of the conditioning variable.

The CMC equations in the enthalpy-based CMC models for the ignition of premixed mixtures share a similar formulation. The first-order closure of the conditionally filtered reaction rates, and the mapping back of the filtered scalars in LES are also same in format. These are summarized above. As discussed above, the defining of a suitable conditioning variable and the modeling of its PDF and SDR are the major challenges in extending CMC in ignition of premixed mixtures. These differences in the enthalpy-based CMC models are emphasized below.

### 3.2.1 Total-Enthalpy-Based CMC Model

For the total-enthalpy-based CMC, total enthalpy,  $h_t$ , is the conditioning variable. The transport equation for total enthalpy in low Mach number flows [108] is

$$\rho \frac{\partial h_t}{\partial t} + \rho u_i \frac{\partial h_t}{\partial x_i} - \frac{\partial}{\partial x_i} \left( \rho D \frac{\partial h_t}{\partial x_i} \right) = \frac{Dp}{Dt}, \quad (3.50)$$

where  $D$  is the molecular diffusivity, and unity Lewis number assumption is used.

From Eq. (3.37), the convective velocity is

$$v_\eta = \left\langle \frac{1}{\rho} \frac{D\tilde{p}}{Dt} | \eta_t \right\rangle, \quad (3.51)$$

where  $\tilde{p}$  is the filtered pressure in LES.  $\eta_t$  is the sample space variable for total enthalpy.

The total enthalpy equation resembles that for a conserved scalar, except for the additional pressure-time-derivative term, which does not have spacial dependence under the low Mach number assumption. The mixing statistics of total enthalpy, including the PDF and SDR, can be approximated using the mixing models for a passive scalar [54, 105, 13, 145]. Here a Beta function is used to approximate the FDF of total enthalpy. The first two moments of total enthalpy, the filtered total enthalpy  $\tilde{h}_t$ , and the sub-filter variance  $\tilde{h}_t''^2$ , are needed to establish the assumed Beta FDF. The dissipation rate of total enthalpy is  $N_{ht} = D\nabla h_t \cdot \nabla h_t$ . The filtered dissipation rate can be approximated by the equilibrium model [107]. The conditional SDR for CMcht is then obtained as,

$$\langle N_{ht} | \eta_t \rangle^* = \frac{\langle \rho \tilde{N}_{ht} | \eta_t \rangle}{\langle \rho | \eta_t \rangle}. \quad (3.52)$$

### 3.2.2 Sensible-Enthalpy-Based CMC Model

The key underlying assumption of CMC is the existence of a scalar that shows strong correlations with other reacting scalars. The strong correlation allows for accurate estimation of chemical reaction rates using the conditionally averaged reacting scalars. The performance of CMC depends on the degree of correlations between the conditioning variable,  $\xi$ , and the reacting scalar,  $\phi$ . Here, sensible enthalpy is chosen as a conditioning variable in CMChs for the ignition of premixed mixtures.

The key advantage of using sensible enthalpy as the conditioning variable is that sensible enthalpy is strongly correlated with temperature as

$$h_s = \int_{T_1}^{T_2} c_p dT, \quad (3.53)$$

where  $h_s$  is the sensible enthalpy of the mixture.  $c_p$  is the constant pressure heat capacity, which is a function of temperature and mixture composition. For ignition and combustion of hydrocarbon fuels, chemical reaction rates show strong nonlinear dependence on temperature, leading to the sensitivity of the reaction rates to temperature. For the samples having a particular value of sensible enthalpy, temperature fluctuations are expected to be small throughout an ignition process. As a result, the estimation of the reaction rates can be made accurate. Sensible enthalpy was suggested as a conditioning variable for premixed combustion firstly by Bilger [14]. Kronenburg [73] adopted sensible enthalpy as a second conditioning variable in the double-conditioning CMC for non-premixed combustion to capture local extinction.

The transport equation for sensible enthalpy in low Mach number flows [108] is

$$\rho \frac{\partial h_s}{\partial t} + \rho u_i \frac{\partial h_s}{\partial x_i} - \frac{\partial}{\partial x_i} \left( \rho D \frac{\partial h_s}{\partial x_i} \right) = \frac{Dp}{Dt} + \dot{\omega}_T, \quad (3.54)$$

where  $D$  is the molecular diffusivity, and unity Lewis number assumption is used.  $\dot{\omega}_T$  is the heat release term due to reaction:

$$\dot{\omega}_T = - \sum_{k=1}^N \Delta h_{f,k}^\circ \dot{\omega}_k, \quad (3.55)$$

where  $\Delta h_{f,k}^\circ$  and  $\dot{\omega}_k$  are the enthalpy of formation and reaction rate of the species  $k$ , respectively.  $N$  is the number of species in the mixture. From Eq. (3.37), the convective velocity is

$$v_\eta = \left\langle \frac{1}{\rho} \left( \frac{D\tilde{p}}{Dt} + \widetilde{\dot{\omega}_T} \right) | \eta_s \right\rangle, \quad (3.56)$$

where  $\eta_s$  is the sample space variable for sensible enthalpy.

Contrary to total enthalpy, sensible enthalpy is a reacting scalar, and the modeling of the mixing of reacting scalars is a challenging problem. The difficulty of modeling the mixing of sensible enthalpy stems from the existence of chemical reactions that

tend to steepen scalar gradients. Due to the reaction-induced steepening, the FDF and the dissipation rate of sensible enthalpy are qualitatively different from those of a conserved scalar. The FDF and filtered SDR of sensible enthalpy can be extracted from DNS data [73] for use in the LES. Alternatively, sophisticated models based on their transport equations can be employed to achieve closure. The FDF of sensible enthalpy can be modeled through solving its transport equation using stochastic methods [57]. The dissipation rate of sensible enthalpy can be modeled by solving its transport equation or by algebraic models [137]. Here, a mapping method is presented to model such mixing terms.

The key idea of the mapping method is to use the mapping from a total enthalpy field to a sensible enthalpy field. Sensible enthalpy is related to total enthalpy of the mixture as,

$$h_t = \sum_i Y_i h_{i,t} = \sum_i Y_i (h_{i,s} + \Delta h_{f,i}^\circ) = h_s + \sum_i Y_i \Delta h_{f,i}^\circ, \quad (3.57)$$

where  $h_{t,i}$ ,  $h_{s,i}$ , and  $\Delta h_{f,i}^\circ$  are total enthalpy, sensible enthalpy, and the enthalpy of formation for the species  $i$ , respectively. The mapping between the total enthalpy field and the sensible enthalpy field can be obtained as,

$$\eta_t = \eta_s + \sum_i Q_i \Delta h_{f,i}^\circ(T_0), \quad (3.58)$$

where  $\eta_t$  and  $\eta_s$  are the sample space variable of total enthalpy and of sensible enthalpy, respectively.  $T_0$  is the reference temperature, and  $Q_i$  are solved in sensible enthalpy space in CMChs.

Figure 3.2 shows a typical mapping curve obtained from Eq. 3.58. Using this mapping, the FDF of sensible enthalpy can be modeled as,

$$\tilde{P}(\eta_s) = \tilde{P}(\eta_t) \frac{d\eta_t}{d\eta_s}, \quad (3.59)$$

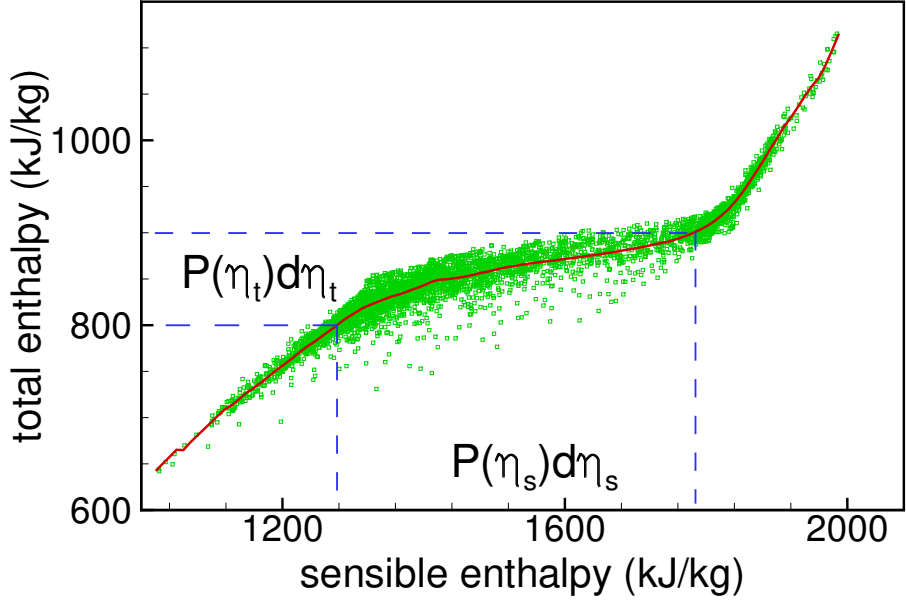


Figure 3.2: Typical (monotonic) mapping curve with scatter plots of total enthalpy on sensible enthalpy from DNS data. The red solid line is obtained from the mapping in Eq. (3.58).  $P(\eta)d\eta$  is the probability of finding the points within the specified enthalpy range. Here,  $P(\eta_t)d\eta_t = P(\eta_s)d\eta_s$ .

where the  $P(\eta_t)$  is the FDF of total enthalpy, and is assumed to be modeled accurately by the beta FDF.

Similarly, the filtered dissipation rate of sensible enthalpy can be related to that of enthalpy as,

$$\widetilde{N}_{hs} \approx \left( \frac{d\tilde{h}_s}{d\tilde{h}_t} \right)^2 \widetilde{N}_{ht}. \quad (3.60)$$

In Eq. (3.60), it is assumed that the gradients of filtered sensible enthalpy are well aligned with those of filtered total enthalpy. The conditionally filtered dissipation rate of sensible enthalpy can be approximated as

$$\langle N_{hs} | \eta_s \rangle \approx \left\langle \left( \frac{dh_s}{dh_t} \right)^2 N_{ht} | \eta_t \right\rangle \approx \langle N_{ht} | \eta_t \rangle \left( \frac{d\eta_s}{d\eta_t} \right)^2. \quad (3.61)$$

It is assumed in Eq. (3.61) that  $\left(\frac{d\widetilde{\eta}_s}{d\eta_t}\right)^2$  and  $\widetilde{N}_{ht}$  are statistically independent, and that  $\langle \left(\frac{d\eta_s}{d\eta_t}\right)^2 | \eta_s \rangle \approx \left(\frac{d\eta_s}{d\eta_t}\right)^2$ . The ‘tilde’ symbol is intentionally omitted inside the conditionally filtering operation  $\langle () | \rangle$  because the LES filtering is included in the operation.

Using the mapping relationship in Eq. (3.58), the FDF and the conditionally filtered SDR of sensible enthalpy can be modeled accurately if the FDF and the conditionally filtered SDR of total enthalpy are provided. However, the above formulations assume monotonicity in the mapping relationship in Eq. (3.58). It is found that at certain stages of ignition, the mapping between sensible enthalpy and total enthalpy can be non-monotonic, which can make the mapping mixing models inaccurate.

Figure 3.3 shows a non-monotonic mapping curve obtained from Eq. 3.58. To remove the monotonic mapping assumption in the modeling of sensible enthalpy FDF, the mapping for FDF is modified as,

$$\widetilde{P}(\eta_{s,i}) = \widetilde{P}(\eta_t) \frac{\delta\eta_t}{\sum_{i=1}^{N_k} \delta\eta_{s,i}}, \quad (3.62)$$

where  $\eta_{s,i}$  are the points in the sensible enthalpy space that intersect with the mapping curve for a given value of total enthalpy,  $\eta_t$ .  $N_k$  is the number of such intersection points. Eq. (3.62) assumes that the FDF of  $\eta_t$  is equally distributed in the corresponding  $\eta_s$  space within the non-monotonic regions, and does not require monotonicity in the mapping. When the mapping is monotonic, Eq. (3.62) becomes equivalent to Eq. (3.59).

To deal with the non-monotonic mapping in the modeling of conditional SDR in Eq. (3.61), a simple averaging approach is proposed. When non-monotonicity is encountered, conditional mean species mass fractions  $Q_i$  in the sensible enthalpy

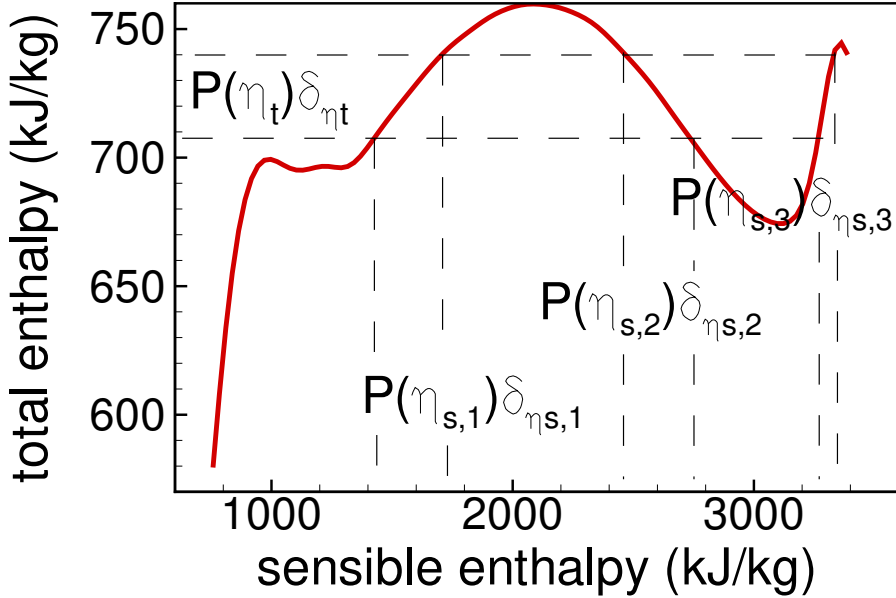


Figure 3.3: A non-monotonic mapping curve and the schematic showing the modification to the PDF mapping. The red solid line is obtained from the mapping in Eq. (3.58), with data from a DNS simulation. A given value of total enthalpy will correspond to multiple values of sensible enthalpy when the mapping is non-monotonic. Here, the total enthalpy range  $\delta\eta_t$  corresponds to three sensible enthalpy ranges, where  $P(\eta_t)\delta\eta_t = \sum_i P(\eta_{s,i})\delta\eta_{s,i}$ .

coordinate are averaged as,

$$Q'_i = \frac{\sum_j^N Q_{i,j}}{N} \quad \text{when } \eta'_t = \eta_t, \quad (3.63)$$

where the summation is taken over all the intersection points of the mapping curve as shown in Fig. 3.4.  $Q_{i,j}$  is the conditional mean mass fraction at the  $j$ -th intersection point.  $N$  is the number of those intersection points.  $\eta'_t$  is the sample space variable for total enthalpy. Using the interpolated species mass fractions, a smoothed mapping curve can be obtained as,

$$\eta'_s = \eta'_t - \sum_i Q'_i \Delta h_{f,i}^\circ(T_0). \quad (3.64)$$

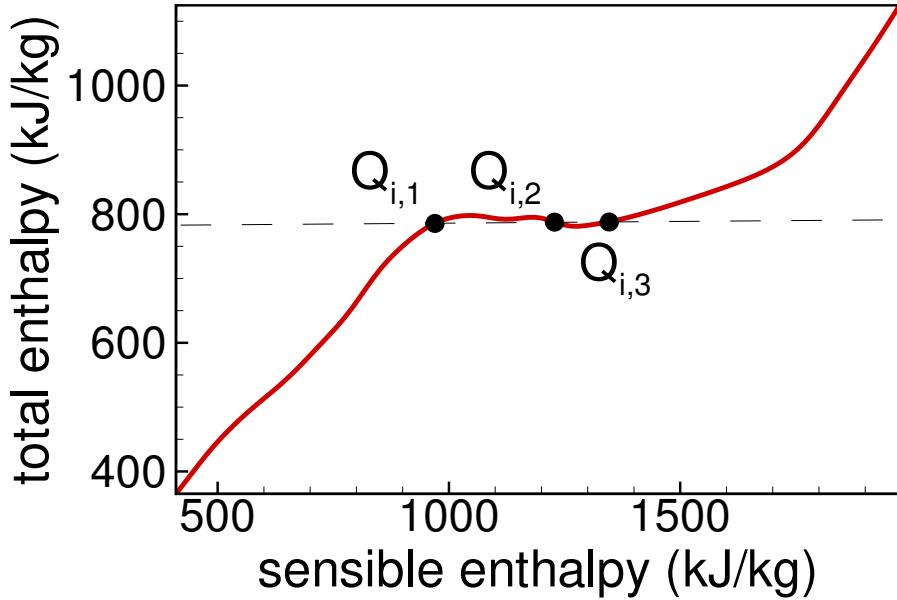


Figure 3.4: Schematic of the modification to the mapping curve for modeling conditional SDR of sensible enthalpy when the mapping is non-monotonic. It has been found that after the modification, the mapping curves become monotonic in the HCCI (fuel-lean) cases.

It has been found that after the modification, the mapping curves become monotonic in the HCCI cases. For the ignition of stoichiometric mixtures, stronger non-monotonic mappings are observed, where this averaging approach can not lead to a smooth monotonic mapping. The reasons leading to this non-monotonic mapping are discussed in Ch. 4.

## **Chapter 4: Validation of the Enthalpy-Based CMC Models Using DNS**

In this chapter, the spatially-integrated enthalpy-based CMC models are validated using data from 2-D DNS of ignition of premixed mixtures under lean and stoichiometric conditions. The ignition of fuel-lean and stoichiometric mixtures correspond to the charge ignition under HCCI conditions and the end-gas auto-ignition under SI engine knocking conditions, respectively. In Sec. 4.1, the spatially-integrated enthalpy-based CMC models for the ignition of premixed mixtures under IC engine conditions are briefly summarized. In Sec. 4.2, the numerical method used in the DNS is summarized. In Sec. 4.3, the validation of the enthalpy-based CMC models under HCCI conditions is presented. In Sec. 4.4, the validation of the enthalpy-based CMC models under SI engine knocking conditions is presented. The major conclusions from the validation studies are summarized at the end of this chapter.

The first three sections in this chapter were previously published as “**Wei Wang and Seung Hyun Kim. Sensible-Enthalpy-Based Conditional Moment Closure Model for Homogeneous Charge Compression Ignition with Temperature Inhomogeneity. Flow, Turbulence and Combustion, (2018): 1-20.**

and are adapted to thesis format.

## 4.1 Spatially-Integrated Enthalpy-Based CMC Models for Ignition of Premixed Mixtures

### 4.1.1 Spatially-Integrated Enthalpy-Based CMC Models

For the ignition of premixed mixtures, the density-weighted conditionally filtered reacting scalar is defined as,

$$Q_\phi(\eta; t) = \frac{\int \rho\phi\delta(h - \eta)F(\mathbf{x} - \mathbf{x}') d\mathbf{x}'}{\int \rho\delta(h - \eta)F(\mathbf{x} - \mathbf{x}') d\mathbf{x}'} \equiv \frac{\langle \rho\phi|\eta \rangle}{\rho_\eta}. \quad (4.1)$$

The end-gas index function  $H(c_\psi^* - \tilde{c}_\psi)$  is neglected in the above definition for the *a priori* analysis of the 2-D DNS data. In the 2-D DNS of ignition of premixed mixtures, there is no premixed flame fronts present before the ignition. Therefore, the end-gas index function  $H(c_\psi^* - \tilde{c}_\psi)$  is 1.0 in the whole computational domain.

With this definition, the transport equations for the conditionally filtered species mass fraction  $Q_k(\eta; t)$  can be obtained by integrating the CMC equations, Eq. (3.46), over the end-gas region:

$$\frac{\partial Q_k}{\partial t} = -v_\eta^* \frac{\partial Q_k}{\partial \eta} + \langle N_\xi|\eta \rangle^* \frac{\partial^2 Q_k}{\partial \eta^2} + \langle W_k|\eta \rangle. \quad (4.2)$$

The unconditional Favre filtered scalar  $\tilde{\phi}$  can be obtained as:

$$\tilde{\phi} = \int_0^1 Q_\phi \tilde{P}(\eta) d\eta. \quad (4.3)$$

### 4.1.2 Closure Models

In Eqs. (4.2) and (4.3),  $\langle W_i|\eta \rangle$ ,  $\langle N_\xi|\eta \rangle$ , and  $\tilde{P}(\eta)$  require closure. The closure models for the enthalpy-based CMC methods are described below and validated for ignition of premixed mixtures under HCCI conditions in Sec. 4.3 and under SI engine knocking conditions in Sec. 4.4.

#### 4.1.2.1 Closure for the Conditional Reaction Rate

Under the assumption that the conditional fluctuations of reactive scalars are small, the conditional reaction rates can be approximated using first order CMC,

$$\langle W_i | \eta \rangle = \dot{\omega}_i(\rho_\eta, Q_i, Q_T). \quad (4.4)$$

#### 4.1.2.2 Closure for the PDF and SDR of the Conditioning Variable

As discussed in Sec. 3.2, the mixing statistics of enthalpy, including the PDF and conditional SDR, can be approximated using the mixing models for a conserved scalar [54, 105, 13, 145]. Here a Beta PDF is used to approximate the distribution of enthalpy.

Contrary to enthalpy, sensible enthalpy is a reacting scalar and the modeling of the mixing of reacting scalars is a challenging problem. The difficulty of modeling the mixing of sensible enthalpy stems from the existence of chemical reactions that tend to steepen scalar gradients. Due to the reaction-induced steepening, the PDF and the dissipation statistics of sensible enthalpy are qualitatively different from those of a conserved scalar. The PDF and SDR of sensible enthalpy can be approximated by data extracted from DNS results [73]. Alternatively, sophisticated models based on their transport equations can be employed to achieve closure. The PDF of sensible enthalpy can be modeled through solving its transport equation using stochastic methods [57]. The dissipation rate of sensible enthalpy can be modeled by solving its transport equation or by algebraic models [137]. Here, a mapping method is presented to model such mixing terms.

The mapping between the enthalpy field and the sensible enthalpy field can be obtained as,

$$\eta_t = \eta_s + \sum_i Q_i \Delta h_{f,i}^\circ(T_0). \quad (4.5)$$

Using the mapping from Eq. (4.5), the PDF of sensible enthalpy can be modeled as,

$$P(\eta_s) = P(\eta_t) \frac{d\eta_t}{d\eta_s}, \quad (4.6)$$

where the  $P(\eta_t)$  is obtained from the presumed PDF method, e.g., the beta PDF [54, 105].

Similarly, the dissipation rate of sensible enthalpy can be related to that of enthalpy as,

$$N_{h_s} \approx \left( \frac{dh_s}{dh_t} \right)^2 N_{h_t}. \quad (4.7)$$

In Eq. (4.7), it is assumed that the gradients of sensible enthalpy are well aligned with those of enthalpy. The conditional dissipation rate of sensible enthalpy can be approximated as

$$\langle N_{h_s} | \eta_s \rangle \approx \langle \left( \frac{dh_s}{dh_t} \right)^2 N_{h_t} | \eta_t \rangle \approx \langle N_{h_t} | \eta_t \rangle \left( \frac{d\eta_s}{d\eta_t} \right)^2. \quad (4.8)$$

It is assumed in Eq. (4.8) that  $\left( \frac{dh_s}{dh_t} \right)^2$  and  $N_{h_t}$  are statistically independent, and that  $\langle \left( \frac{dh_s}{dh_t} \right)^2 | \eta_s \rangle \approx \left( \frac{d\eta_s}{d\eta_t} \right)^2$ .

The above formulations also assume monotonicity in the mapping relationship in Eq. (3.58). To consider the non-monotonic mapping relation, the modeling for the sensible enthalpy PDF can be modified as,

$$P(\eta_{s,i}) = P(\eta_t) \frac{\delta\eta_t}{\sum_{i=1}^{N_k} \delta\eta_{s,i}}. \quad (4.9)$$

Eq. (4.9) assumes that the PDF of  $\eta_t$  is equally distributed in the corresponding  $\eta_s$  space within the non-monotonic regions, and does not require monotonicity in the

mapping. When the mapping is monotonic, Eq. (4.9) becomes equivalent to Eq. (4.6). To deal with the non-monotonic mapping in the modeling of conditional SDR in Eq. (4.8), a simple averaging approach is proposed for ignition of lean mixtures. The details of this mapping approach can be found in Sec. 3.2.

## 4.2 Numerical Methods for the DNS

The low Mach number, variable density formulation is used for all the DNS cases. The mass, momentum, species, and energy conservation equations are solved. For energy conservation, the equation for enthalpy is solved. For multi-component species transport, the Hirschfelder and Curtiss model with the mixture-averaged diffusion coefficients [60, 108] is used, and the correction velocity is added to ensure the overall mass conservation. The equations are solved using a second-order, conservative finite-difference method for DNS and LES [38]. For the velocity, the second-order centered finite difference scheme is used for spatial derivatives. The fifth-order weighted essentially non-oscillatory (WENO) scheme [87] is used for the convection terms in the scalar equations. A second-order semi-implicit Crank-Nicholson method is used for time integration. An operator splitting method is used for the integration of stiff chemical reactions. DVODE [21] is used for the time integration of the chemical reaction part in the operator splitting method. Thermodynamic and transport properties are evaluated using CHEMKIN and TRANSPORT packages [60].

## 4.3 Validation of CMC Models under HCCI Conditions

### 4.3.1 Initial Conditions for the DNS

To validate the enthalpy-based CMC models under HCCI condition, *a priori* analysis with 2-D constant volume DNS of lean n-heptane/air ignition data are conducted. The simulation conditions for the DNS cases are similar to those in Yoo *et al.* [154],

Case	$\phi_0$	$p_0$ (atm)	$\bar{T}_0$ (K)	$T_0'$ (K)	$u'$ (m/s)	$\tau_{ig}$ (ms)	Differential diffusion
1	0.3	40	934	15	0.5	2.155	yes
2	0.3	40	934	30	0.5	2.094	yes
3	0.3	40	934	60	0.5	1.931	yes
4	0.3	40	934	100	0.5	1.676	yes
5	0.3	40	934	60	0.5	1.938	no
6	0.3	40	934	100	0.5	1.671	no

Table 4.1: Initial and simulation conditions for the DNS cases under HCCI conditions. Also shown are the ignition delay times

and are summarized in Table 4.1. For the ignition chemistry, the chemical mechanism of Liu *et al.* [86] is used, which consists of 185 reactions involving 43 species. The computational domain is a square box with periodic boundary conditions. The size of the box is 6.4 mm  $\times$  6.4 mm, and is discretized by 1024  $\times$  1024 grid points for all cases. The initial pressure is  $p_0 = 40$  atm. The initial mixture composition is a homogeneous n-heptane/air mixture with an equivalence ratio,  $\phi_0$ , of 0.3. The velocity fields are prescribed using the Passot-Pouquet [103] spectrum with zero mean velocity, the root mean square (r.m.s.) velocity fluctuations,  $u'$ , of 0.5 m/s, and the most energetic length scale,  $l_e$ , of 1.2 mm. The Kolmogorov scales for the initial fields are around 25  $\mu$ m. The temperature field is initialized using a Passot-Pouquet spectrum modified

for scalars. The mean temperature,  $\bar{T}_0$ , is set to be 934 K. The integral length scale of temperature,  $l_{Te}$ , is 1.2 mm, while the levels of temperature fluctuations in the spectrum are varied. The r.m.s. temperature fluctuations considered here are 15 K, 30 K, 60 K, and 100 K for Cases 1, 2, 3, and 4, respectively. The initial temperature and velocity fields for Case 4 are shown in Fig. 4.1 to illustrate the DNS cases setup.

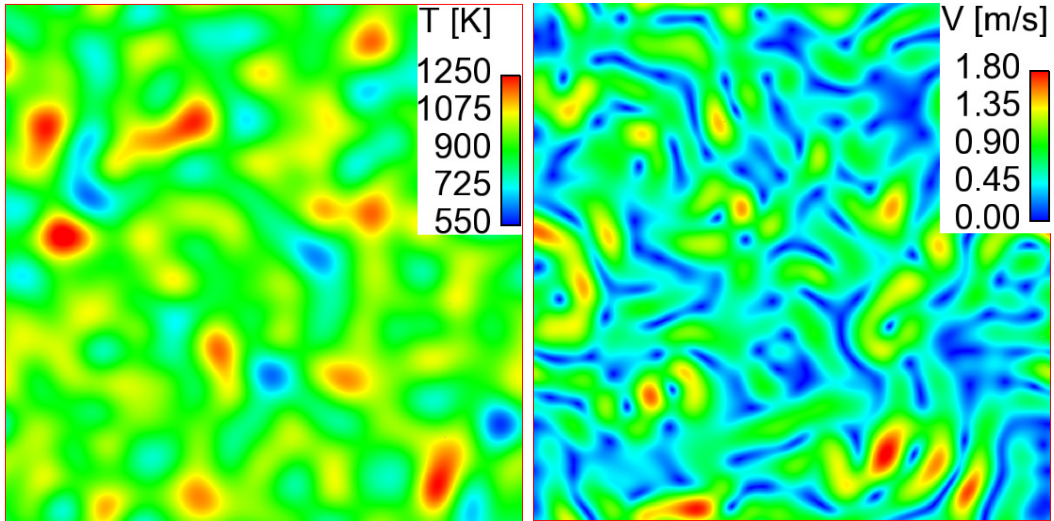


Figure 4.1: Initial temperature field (left) and velocity field for Case 4.

Before conducting the DNS, grid sensitivity and time step sensitivity studies are performed to ensure the smallest scales are fully resolved with the proposed resolution. Firstly, DNS of a 1-D laminar freely propagating flame are conducted under the initial mean temperature and pressure conditions in Table 4.1. With the same resolution as in Table 4.1, the temperature layer is found to be resolved with about 16 grid points, and the H radical layer (a very thin radical layer) about 6 grid points. Then the grid sensitivity and time step sensitivity study are performed for Case 4 on a

$3.2 \text{ mm} \times 3.2 \text{ mm}$  domain, which is of the same size as in the DNS work by Yoo *et al.* [154]. For the grid sensitivity study, three grid resolutions,  $256 \times 256$ ,  $512 \times 512$  and  $1024 \times 1024$ , are studied, which corresponds to a grid size of  $12.5 \mu\text{m}$ ,  $6.25 \mu\text{m}$ , and  $3.125 \mu\text{m}$  respectively. In the work by Yoo *et al.* [154], a grid size of  $5 \mu\text{m}$  was used for Cases 1–3, and a grid size of  $2.5 \mu\text{m}$  was used for Case 4. For the time step sensitivity study, time step sizes in the range of  $0.3 \mu\text{s}$ – $1.2 \mu\text{s}$  were studied for Case 4. The results for the grid and time step sensitivity study in terms of the ignition delay are summarized in Table 4.2. The relative error for the ignition delay is within 0.1% for the grid size of  $6.25 \mu\text{m}$  and the time step of  $1.0 \mu\text{s}$  as compared with the reference simulation with the grid size of  $3.125 \mu\text{m}$  and the time step of  $0.6 \mu\text{s}$ . The time step of  $1 \mu\text{s}$  and the grid size of  $6.25 \mu\text{m}$  is chosen from the sensitivity study.

Case	$N_x$	$dx (\mu\text{m})$	$dt (\mu\text{s})$	$\tau_{ig}$ (ms)	Err (%)
S1	512	6.25	1.2	1.7202	0.105
S2	512	6.25	1.0	1.7205	0.087
S3	512	6.25	0.6	1.7208	0.070
S4	512	6.25	0.3	1.7217	0.018
S5	256	12.5	0.6	1.5876	7.805
S6	1024	3.125	0.6	1.7220	0.000

Table 4.2: Grid and time step sensitivity study for Case 4

### 4.3.2 Results and Discussion

The enthalpy-based CMC models, CMCh<sub>t</sub> and CMCh<sub>s</sub>, are validated *a priori* with the DNS data. The emphasis is placed on the effects of the choice of a conditioning variable on conditional fluctuations of reacting scalars and the reaction rate

closure. The performance of the models based on the mapping method for PDF and conditional dissipation rates of sensible enthalpy are also investigated. When presenting the results, a normalized sample space variable,  $\zeta$ , and a normalized time,  $t^*$  are used. The sample space variable  $\eta$  is normalized by using the minimum and maximum of the corresponding enthalpy at a given time,  $\eta_{min}$  and  $\eta_{max}$ , as,

$$\zeta = \frac{\eta - \eta_{min}}{\eta_{max} - \eta_{min}}. \quad (4.10)$$

The time is normalized by the ignition delay time  $\tau_{ig}$ ,

$$t^* = \frac{t}{\tau_{ig}}. \quad (4.11)$$

Here  $\tau_{ig}$  is defined as the time of the maximum heat release rate.

### Temperature fields

Figure 4.2 shows the temperature fields at various ignition stages, along with iso-scalar surfaces of total enthalpy and of sensible enthalpy. For the iso-scalar surfaces, the value of sensible enthalpy is chosen to demarcate ignition spots. The value used in iso-scalar surfaces of total enthalpy is obtained from the mapping relation in Eq. (3.58). In Fig. 4.2, for Case 3 at  $t^* = 0.2$ , where  $t^*$  is the normalized time, the iso- $h_s$  and iso- $h_t$  surfaces overlap with each other, indicating that during an early stage of fuel oxidation total enthalpy is well correlated with sensible enthalpy. At  $t^* = 0.6$ , ignition begins to occur in localized spots with higher temperature. At  $t^* = 0.99$ , the iso- $h_t$  surface deviates from the iso- $h_s$  surface in some regions. For Case 4, a similar trend is observed.

### Conditional fluctuations of reacting scalars

Figure 4.3 shows the conditional r.m.s. fluctuations of the temperature and the fuel

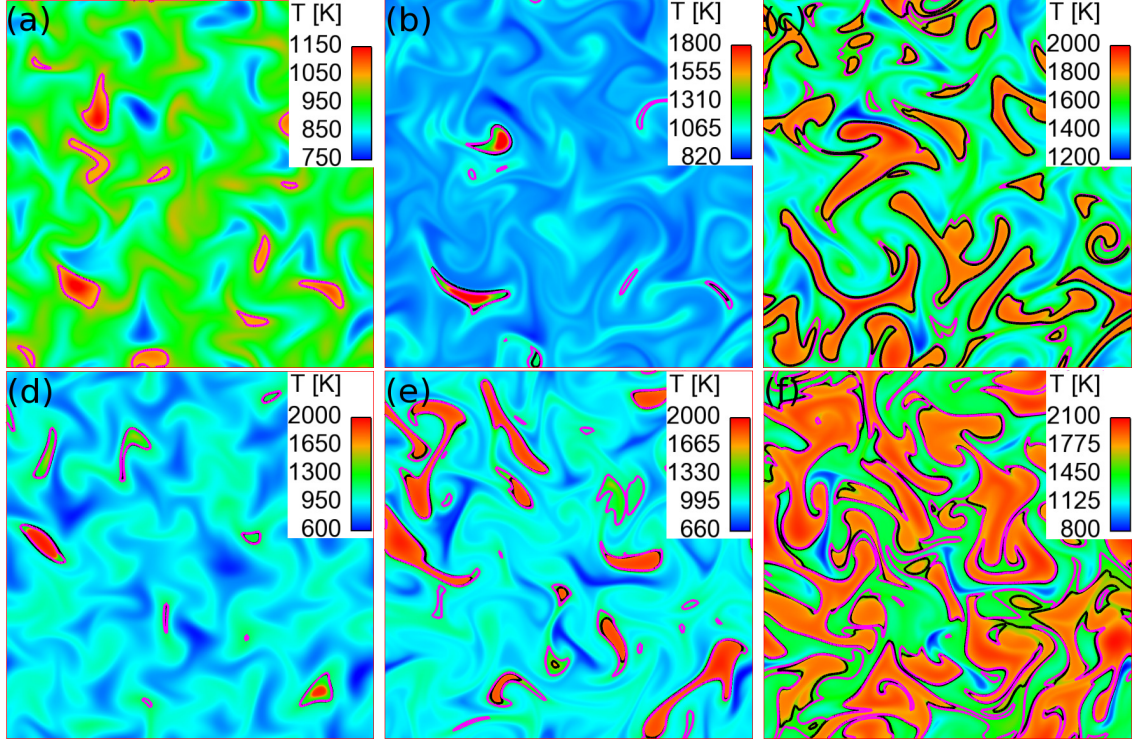


Figure 4.2: Temperature fields and iso-scalar surfaces of sensible enthalpy and of total enthalpy at various stages of ignition. (a)  $t^* = 0.2$  for Case 3 ( $T_0' = 60K$ ), (b)  $t^* = 0.6$  for Case 3 ( $T_0' = 60K$ ), (c)  $t^* = 0.99$  for Case 3 ( $T_0' = 60K$ ), (d)  $t^* = 0.2$  for Case 4 ( $T_0' = 100K$ ), (e)  $t^* = 0.6$  for Case 4 ( $T_0' = 100K$ ), and (f)  $t^* = 0.99$  for Case 4 ( $T_0' = 100K$ ). The magenta contour lines represent iso- $h_t$  surfaces, while the black ones represent iso- $h_s$  surfaces

mass fraction for Case 4, which are represented as error bars on top of the corresponding conditional mean values. The conditional fluctuation is defined as  $\phi'' = \phi - \langle \phi | \eta \rangle$ , representing the deviation from the conditional average  $\langle \phi | \eta \rangle$ . The level of conditional fluctuations shows how the reactive scalars are correlated with the conditioning variable. The smaller fluctuations lead to the better estimation of conditional mean reaction rates. The conditional fluctuations of temperature are substantially reduced when sensible enthalpy is taken as the conditioning variable. This implies the strong

correlation of temperature with sensible enthalpy. The conditional fluctuations of the fuel mass fraction are also reduced for the sensible enthalpy conditioning, while the reduction is not as substantial as that for the temperature.

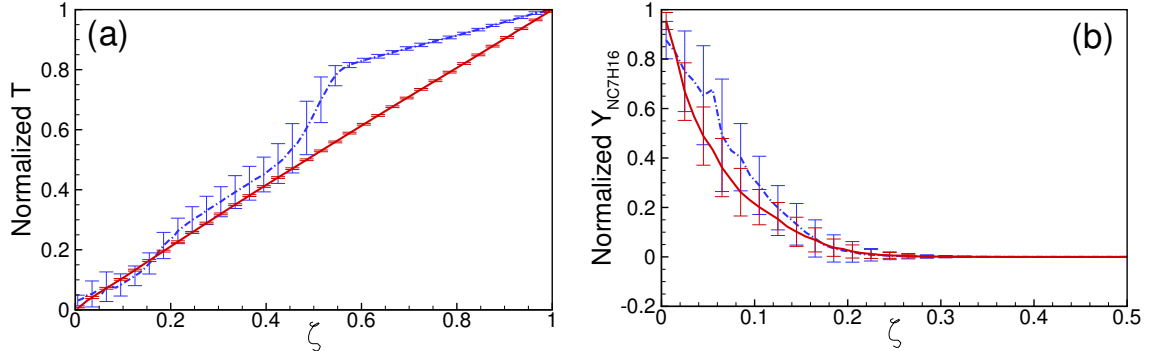


Figure 4.3: Conditional mean and r.m.s. fluctuations of (a) temperature and (b) fuel mass fraction for Case 4 ( $T_0' = 100\text{K}$ ) at  $t^* = 0.99$  (red solid lines: conditional mean based on sensible-enthalpy conditioning, blue dashed-dotted lines: conditional mean based on total-enthalpy conditioning, error bars: conditional r.m.s. fluctuations)

### Heat release rate prediction and reaction rate closure

To illustrate the effects of a conditioning variable on the reaction rate closure, heat release rates for Case 4 at  $t^* = 0.955$  are shown in Fig. 4.4. Together with the conditionally averaged values, the scatter data for heat release rates is also shown. With conditioning, fluctuations of heat release rates for a given value of sensible enthalpy are smaller than those based on total enthalpy conditioning. Such fluctuations are induced by the fluctuations in the species mass fractions, as indicated by the results in Fig. 4.3. For total enthalpy conditioning, both temperature and species mass fractions fluctuate substantially for this case, which leads to more fluctuations around the conditional mean reaction rates. As a result, CMCh<sub>t</sub> leads to the substantial

overprediction of heat release rates. On the other hand, the sensible-enthalpy-based closure, CMChs, leads to an excellent prediction of the conditional mean heat release rates, even with fluctuations in heat release rates around the conditional mean values. This is because temperature fluctuations are substantially suppressed, when sensible enthalpy is used as the conditioning variable. The errors in the first-order reaction rate closure come from non-linearity in reaction rates. The errors due to strong non-linear dependence of the reaction rates on temperature are suppressed in the sensible-enthalpy-based closure.

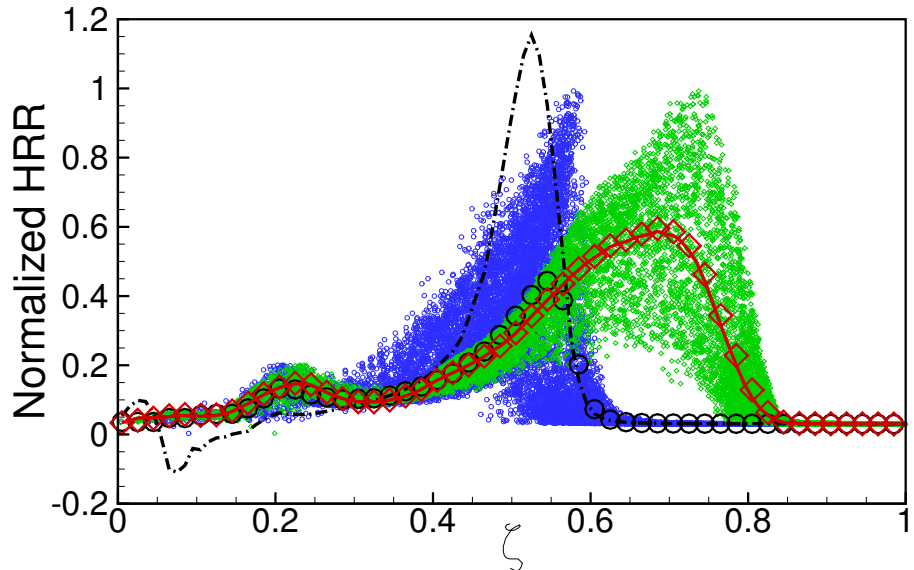


Figure 4.4: Scatter plot and conditional means for heat release rates for Case 4 ( $T_0' = 100K$ ) at  $t^* = 0.955$  (black dashed-dotted line: CMChs, black circles: DNS data with total-enthalpy conditioning, red solid line: CMChs, red diamonds: DNS data with sensible-enthalpy conditioning; small blue and green circles represent the scatter data for heat release rates plotted in the normalized total enthalpy coordinate and in the normalized sensible enthalpy coordinate, respectively)

Figure 4.5 shows the conditionally averaged heat release rates at different time instants for Cases 1, 3 and 4. For Case 3 with  $T'_0 = 60\text{ K}$ , CMCh tends to overpredict the heat release rates as the ignition progresses. For Case 4 with  $T'_0 = 100\text{ K}$ , the CMCh results show substantial deviations from the DNS results at all stages of the ignition process. Results for CMChs are in excellent agreement with the DNS data for all the cases. For Case 1 with  $T'_0 = 15\text{ K}$ , both CMChs and CMCh results are in excellent agreement with the DNS data at all time instants.

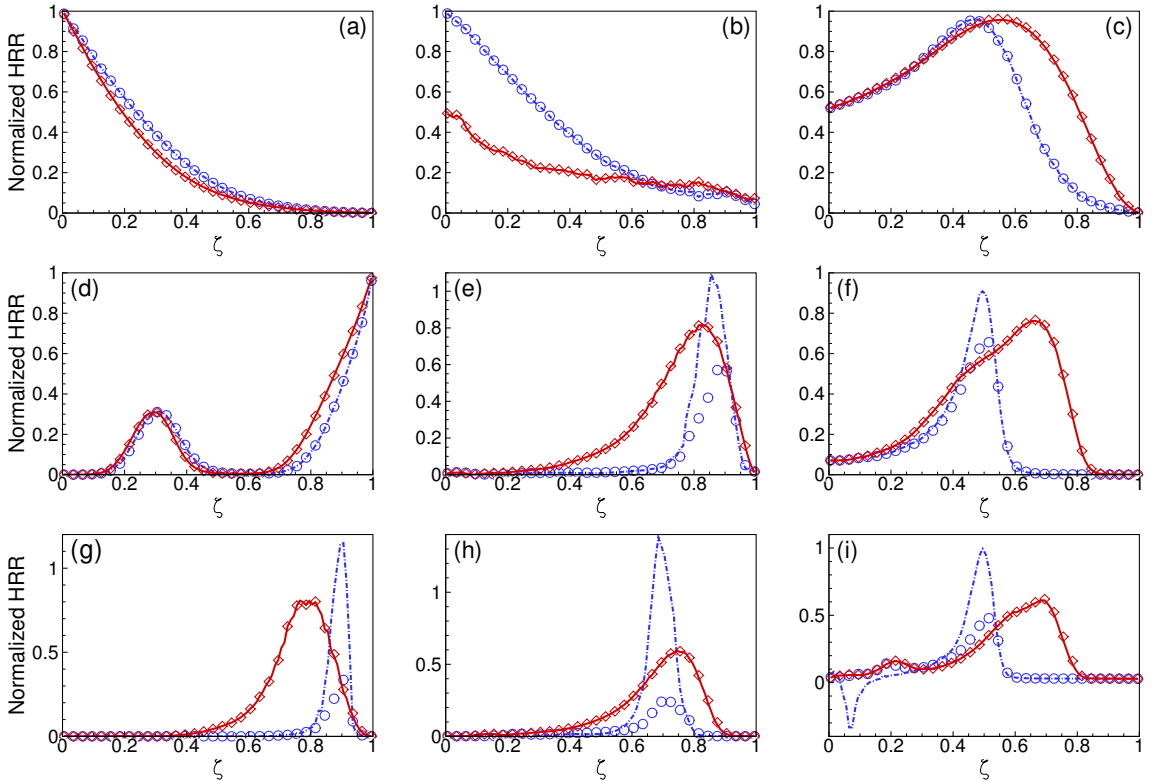


Figure 4.5: Normalized conditional mean heat release rates for Case 1 ( $T'_0 = 15\text{ K}$ ) at (a)  $t^* = 0.2$ , (b)  $t^* = 0.6$ , and (c)  $t^* = 0.99$ ; Case 3 ( $T'_0 = 60\text{ K}$ ) at (d)  $t^* = 0.2$ , (e)  $t^* = 0.6$ , and (f)  $t^* = 0.99$ ; and Case 4 ( $T'_0 = 100\text{ K}$ ) at (g)  $t^* = 0.2$ , (h)  $t^* = 0.6$ , and (i)  $t^* = 0.99$  (blue circles: DNS data with total-enthalpy conditioning, blue dashed-dotted lines: CMCh, red diamonds: DNS data with sensible-enthalpy conditioning, red solid lines: CMChs)

In Figs. 4.6 and 4.7, the conditionally averaged reaction rates of  $\text{H}_2\text{O}_2$  and OH, at different time instants for Cases 1, 3 and 4 are shown. OH and  $\text{H}_2\text{O}_2$  are key species in the ignition of a hydrocarbon-air mixture under HCCI conditions.  $\text{H}_2\text{O}_2$  forms first and remains relatively inert.  $\text{H}_2\text{O}_2$  then decomposes rapidly into OH radicals, leading to rapid ignition [148].

In Fig. 4.6, for Case 1 with  $T'_0 = 15\text{ K}$ , the reaction rates of  $\text{H}_2\text{O}_2$  predicted by CMcht are in good agreement with the DNS data before the thermal runaway. At the time of the maximum heat release rate, the results predicted by CMcht deviate slightly from the DNS data in most reaction layers. Results from CMChs are in excellent agreement with the DNS data. For Case 3 with  $T'_0 = 60\text{ K}$ , CMcht leads to large errors at  $t^* = 0.6$ , when the temperature in some hot regions reaches around 1000K and  $\text{H}_2\text{O}_2$  begins to decompose rapidly. CMChs well captures this change in the  $\text{H}_2\text{O}_2$  reaction. At  $t^* = 0.99$ , large errors remain in the CMcht results, while CMChs performs well. For Case 4 with  $T'_0 = 100\text{ K}$ , CMcht results deviate substantially from the DNS results at all the time instants. CMChs well captures the rates of  $\text{H}_2\text{O}_2$  reactions.

Figure 4.7 shows the assessment of CMChs and CMcht in estimating conditionally averaged reaction rates for the OH mass fraction. A trend is similar to that for  $\text{H}_2\text{O}_2$ . CMcht results in large errors for the OH reaction rates after the  $\text{H}_2\text{O}_2$  decomposition occurs, and CMChs well captures the rates of the OH reactions. While the results from CMChs deviates from the DNS data for Case 1 at  $t^* = 0.6$  and Case 3 at  $t^* = 0.2$  in Fig. 4.7, it is noted that the radical concentrations and reaction rates are very small at these time instants.

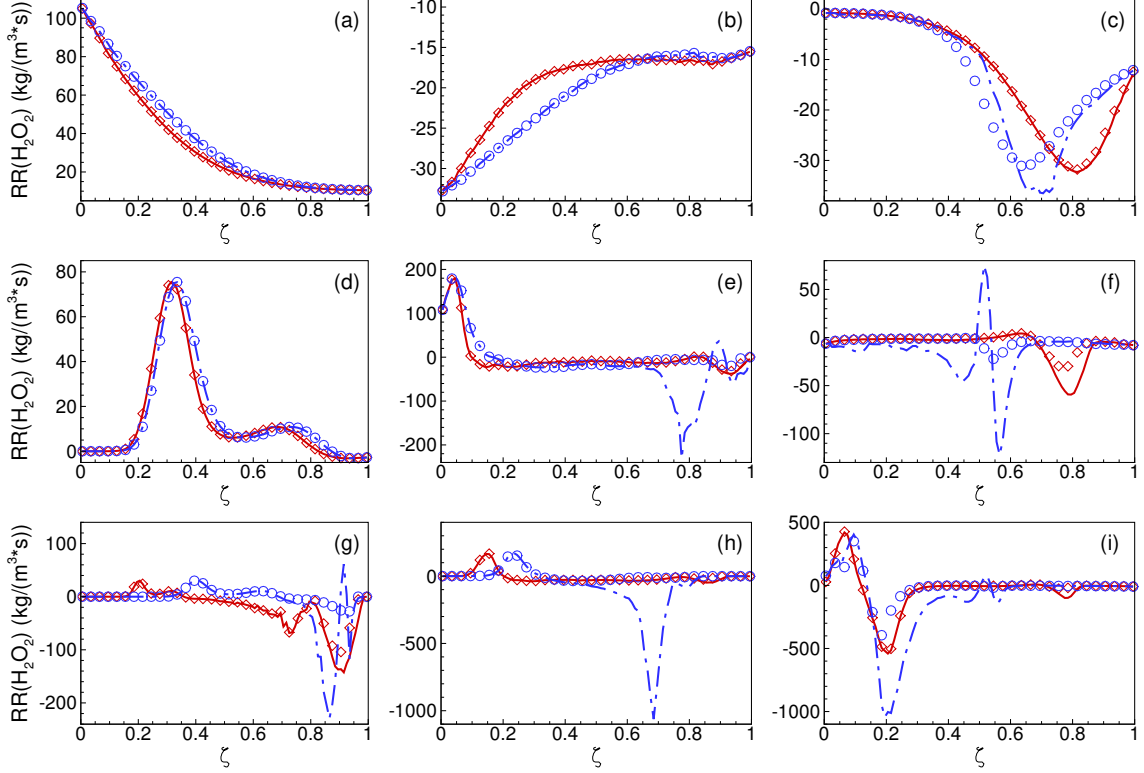


Figure 4.6: Conditional mean reaction rates of  $\text{H}_2\text{O}_2$  for Case 1 ( $T_0' = 15\text{K}$ ) at (a)  $t^* = 0.2$ , (b)  $t^* = 0.6$ , and (c)  $t^* = 0.99$ ; Case 3 ( $T_0' = 60\text{K}$ ) at (d)  $t^* = 0.2$ , (e)  $t^* = 0.6$ , and (f)  $t^* = 0.99$ ; and Case 4 ( $T_0' = 100\text{K}$ ) at (g)  $t^* = 0.2$ , (h)  $t^* = 0.6$ , and (i)  $t^* = 0.99$  (blue circles: DNS data with total-enthalpy conditioning, blue dashed-dotted lines: CMChs, red diamonds: DNS data with sensible-enthalpy conditioning, red solid lines: CMChs)

### Mapping relationship

Figure 4.8 shows the mapping relationship between sensible enthalpy and total enthalpy for Cases 1, 3, and 4. In this *a priori* study, the conditional mean species mass fractions,  $Q_i$ , are obtained by conditionally averaging the DNS data. The original mapping is then obtained using Eq. (3.58). When the mapping is non-monotonic, the reconstructed monotonic mapping is obtained using Eqs. (3.63) and (3.64). For Case 1, the mapping curves are almost linear and monotonic from  $t^* = 0.2$  to  $t^* = 0.99$ ,

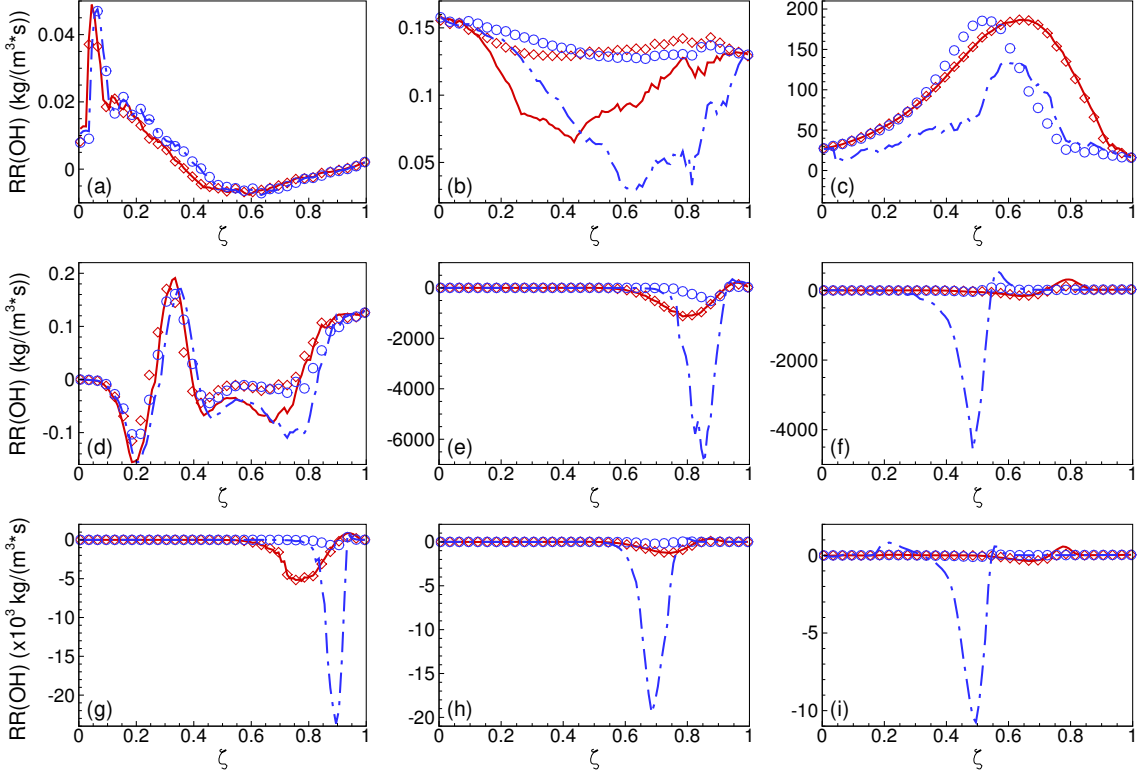


Figure 4.7: Conditional mean reaction rates of OH for Case 1 ( $T_0' = 15K$ ) at (a)  $t^* = 0.2$ , (b)  $t^* = 0.6$ , and (c)  $t^* = 0.99$ ; Case 3 ( $T_0' = 60K$ ) at (d)  $t^* = 0.2$ , (e)  $t^* = 0.6$ , and (f)  $t^* = 0.99$ ; and Case 4 ( $T_0' = 100K$ ) at (g)  $t^* = 0.2$ , (h)  $t^* = 0.6$ , and (i)  $t^* = 0.99$  (blue circles: DNS data with total-enthalpy conditioning, blue dashed-dotted lines: CMChs, red diamonds: DNS data with sensible-enthalpy conditioning, red solid lines: CMChs)

indicating that total enthalpy and sensible enthalpy are closely correlated. The closure of the PDF and the conditional SDR are expected to perform well with this kind of mapping. For Case 3, the mapping at an early stage,  $t^* = 0.2$ , is linear and monotonic. As the ignition occurs and the ignition fronts propagate, the mapping becomes non-linear and non-monotonic. In the flat region of the mapping curve, there are large conditional temperature fluctuations when total enthalpy is chosen as the conditioning variable. For Case 4, the mapping curves are non-linear at all ignition

stages. The mapping curve becomes non-monotonic after  $t^* = 0.2$ . The modified mapping curves are monotonic. The levels of conditional fluctuations in the mapping relation for Cases 1 and 4 are shown in Fig. 4.9.

The non-monotonic part of the mapping curve corresponds to ignition fronts where sensible enthalpy changes rapidly. The non-monotonicity may originate from the NTC, turbulent fluctuations, or the differential diffusion effects. The effects of the differential diffusion are investigated by performing DNS cases with the unity Lewis number assumption. As shown in Fig. 4.10, the differential diffusion effects in the present cases are minor and the mapping is still non-monotonic in the unity Lewis number cases. The chemical mechanism of Liu *et al.* [86] reproduces the NTC effects in the present cases. The NTC effects can lead to non-monotonicity in the mapping, because of the non-monotonic dependence of ignition delay on temperature, which can distort the initially monotonic mapping. The non-monotonic dependence of ignition delay on temperature also tends to increase conditional fluctuations of species mass fractions, especially those of radicals. Fluctuations in heat release rates in Fig. 4.4 are related to such fluctuations in species mass fractions. However, it is found that first-order closure works well even with such conditional fluctuations when sensible enthalpy is taken as a conditioning variable. Overall, the non-monotonicity in the present cases is not substantial. The simple averaging approach in Eqs. (3.63) and (3.64) is found to be sufficient in removing the non-monotonicity in the present cases.

Non-monotonic mapping can also result from the stratification of mixture composition. With a single conditioning variable based on enthalpy, the dependence of ignition delay on the mixture composition can lead to conditional fluctuations of species mass

fractions in ignition fronts. Depending on the correlation between mixture stratification and thermal stratification, non-monotonic mapping can result. Our assumption is that for lean mixtures that are of interest in HCCI, this non-monotonicity can be dealt with an *ad hoc* modification, such as that proposed in Sec. 3.2. When the level of mixture inhomogeneity is beyond the acceptable level, double-conditioning CMC adopting another conditioning variable related to the mixture inhomogeneity needs to be used.

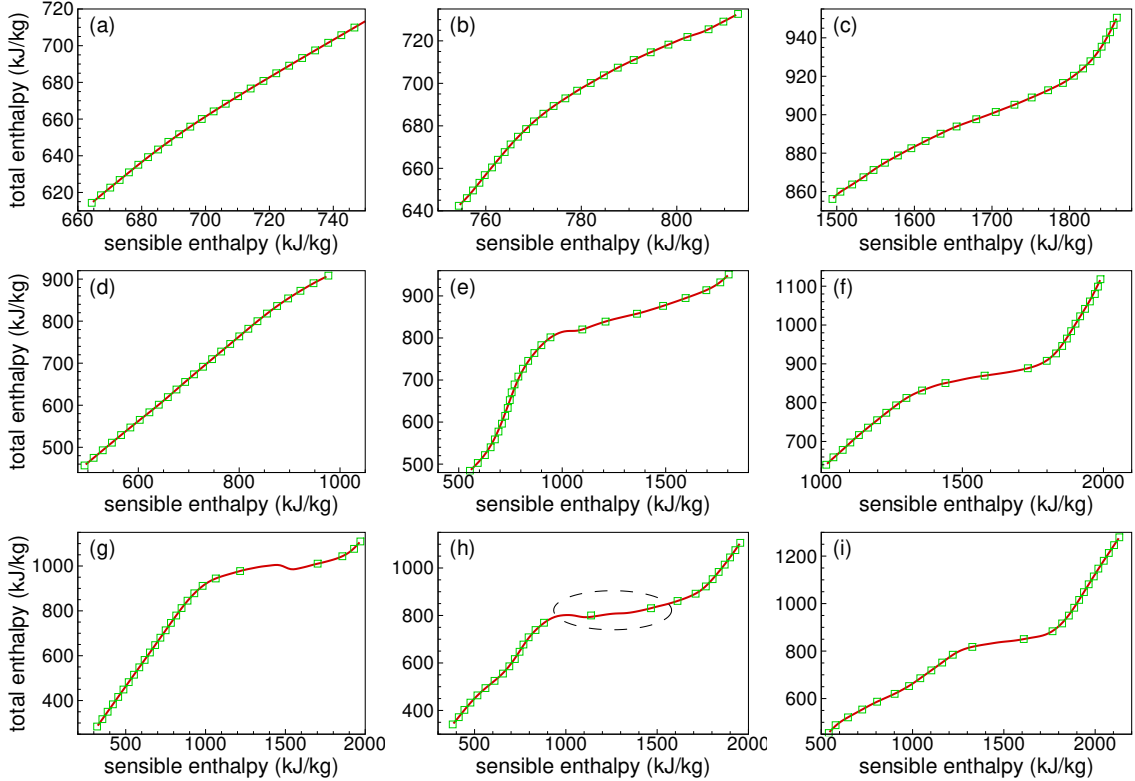


Figure 4.8: Mapping curve for PDF and conditional SDR modeling. (a) Case 1 ( $T_0' = 15K$ ) at  $t^* = 0.2$ , (b)  $t^* = 0.6$ , and (c)  $t^* = 0.99$ . (d) Case 3 ( $T_0' = 60K$ ) at  $t^* = 0.2$ , (e)  $t^* = 0.6$ , and (f)  $t^* = 0.99$ . (g) Case 4 ( $T_0' = 100K$ ) at  $t^* = 0.2$ , (h)  $t^* = 0.6$ , and (i)  $t^* = 0.99$  (red solid lines: original mapping curve  $\eta_t - \eta_s$ , green squares: modified mapping curve  $\eta_t' - \eta_s'$ )

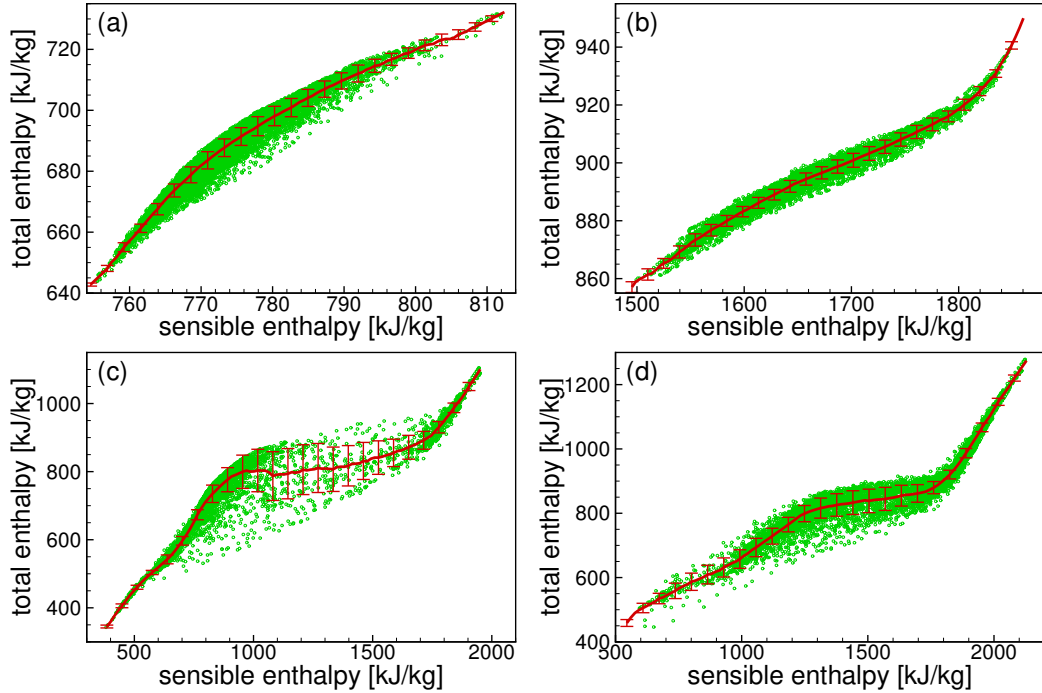


Figure 4.9: Mapping curve and conditional fluctuations. (a) Case 1 ( $T_0' = 15K$ ) at  $t^* = 0.6$ , and (b)  $t^* = 0.99$ . (c) Case 4 ( $T_0' = 100K$ ) at  $t^* = 0.6$ , and (d)  $t^* = 0.99$

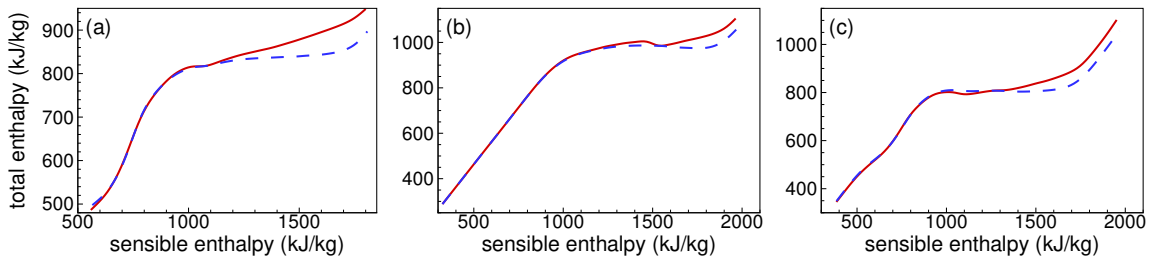


Figure 4.10: Effects of differential diffusion on the mapping curve. (a) Case 3 ( $T_0' = 60K$ ) at  $t^* = 0.6$ , (b) Case 4 ( $T_0' = 100K$ ) at  $t^* = 0.2$ , and (c) Case 4 ( $T_0' = 100K$ ) at  $t^* = 0.6$  (red solid lines: mapping curve  $\eta_t - \eta_s$ , blue dashed lines: mapping curve  $\eta_t - \eta_s$  from the corresponding DNS cases with the unity Lewis number assumption – Cases 5 and 6)

## **PDF and conditional dissipation rates of sensible enthalpy**

To obtain the mean heat release rates and the averages of reacting scalars, including the species mass fractions, density and temperature, the conditional averages weighted by the PDF of the conditioning variable are integrated in the conditioning variable space as in Eq. (5.3). In addition to the conditional averages, the PDF of a conditioning variable is thus of critical importance to accurate prediction. Here, the mapping approach for the PDF of sensible enthalpy is validated.

Figure 4.11 shows the PDFs of sensible enthalpy and of total enthalpy for Cases 1, 3, and 4. The modified monotonic mapping is used to evaluate the sensible enthalpy PDF using Eq. (4.6). The total enthalpy PDF has one peak, and is not far from the Gaussian distribution. The width of PDF tends to decrease with time, as mixing occurs. The PDF of total enthalpy is well described by the presumed beta PDF in the present cases. The PDF of sensible enthalpy shows qualitatively different behaviors. Initially, when ignition is not much progressed, the shape of the sensible enthalpy PDF is similar to that of the total enthalpy PDF. As ignition progresses, ignited hot spots are generated, which makes another peak at higher values of sensible enthalpy. For Case 1, where the initial temperature inhomogeneity is weak, the ignition delay for different mixtures is not significantly different and ignition progresses almost simultaneously. As a result, the entire PDF is moving towards higher values of sensible enthalpy as ignition progresses. As the initial temperature inhomogeneity increases, the PDF of sensible enthalpy shows two peaks, one on the lower sensible enthalpy side for unigated spots and the other on the higher sensible enthalpy side for ignited spots. The proposed model captures all such trends in the evolution of the sensible enthalpy PDF.

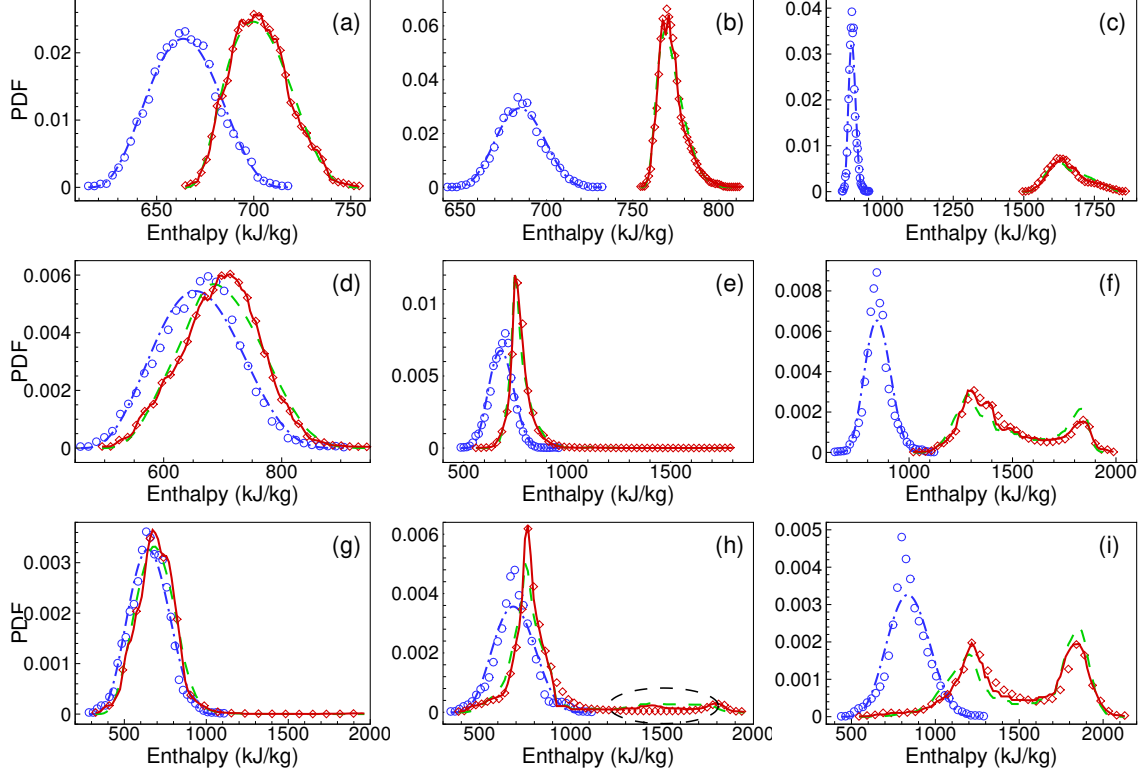


Figure 4.11: PDF of sensible enthalpy and total enthalpy for Case 1 ( $T_0' = 15K$ ) at (a)  $t^* = 0.2$ , (b)  $t^* = 0.6$ , and (c)  $t^* = 0.99$ ; Case 3 ( $T_0' = 60K$ ) at (d)  $t^* = 0.2$ , (e)  $t^* = 0.6$ , and (f)  $t^* = 0.99$ ; and Case 4 ( $T_0' = 100K$ ) at (g)  $t^* = 0.2$ , (h)  $t^* = 0.6$ , and (i)  $t^* = 0.99$  (blue circles: total-enthalpy PDF from DNS, blue dashed-dotted lines: beta PDF for total enthalpy, red diamonds: sensible-enthalpy PDF from DNS, red solid lines: modeled sensible-enthalpy PDF using total-enthalpy PDF from DNS, green dashed lines: modeled sensible-enthalpy PDF using beta PDF for total-enthalpy)

Figure 4.12 shows the comparison of the sensible enthalpy PDFs obtained using the two proposed PDF modeling approaches. When non-monotonicity exists in the mapping, the PDF of sensible enthalpy can be modeled using the two approaches proposed in Sec. 3.2. The first approach, Eq. (4.6), employs the monotonic mapping reconstruction, while the second one, Eq. (4.9), does not require monotonicity in the mapping. Even for Case 4, where the degree of the non-monotonicity is the most

significant, the modeled PDFs using the two approaches are very similar to each other.

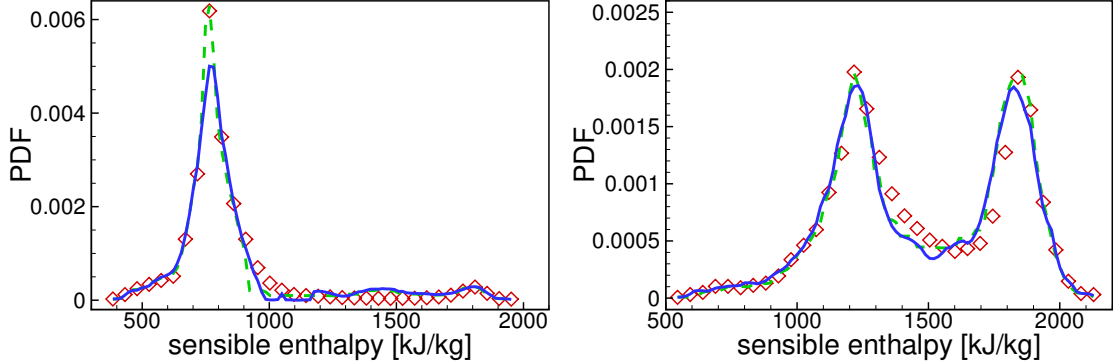


Figure 4.12: Comparison of the PDFs of sensible enthalpy predicted by the two different approaches, Eqs. (4.6) and (4.9), for Case 4 ( $T_0' = 100K$ ) at (a)  $t^* = 0.6$  and (b)  $t^* = 0.99$  (red diamonds: sensible-enthalpy PDF from DNS; green dashed lines: modeled PDF using modified mapping, Eq. (4.6), and DNS PDF for total-enthalpy; blue solid lines: modeled PDF using equal-distribution assumption, Eq. (4.9), and DNS PDF for total-enthalpy)

The modeled conditional dissipation rates for sensible enthalpy are shown in Fig. 4.13. Conditional dissipation rates of sensible enthalpy represent small-scale molecular mixing rates and are responsible for describing turbulence-chemistry interactions at small scales in CMC. The proposed mapping method well reproduces the trends, but leads to the overprediction as the ignition process progresses in Cases 3 and 4. For Case 1, where  $T_0' = 15K$ , the mapping is almost linear and conditional fluctuations in the mapping relation are small as shown in Fig. 4.9. The assumptions made in the modeling are thus well satisfied, and the proposed model works well for this case. As the level of temperature inhomogeneity increases, conditional fluctuations in the mapping relation also increase. Fluctuations in the alignment of

the sensible enthalpy gradient and the total enthalpy gradient, and those in the ratio of the magnitudes of the scalar gradients also become larger. This leads to the overprediction of the conditional dissipation rate across the ignition fronts for Cases 3 and 4. However, for the unburned regions, where conditional fluctuations in the mapping relation are small, the proposed model works well. The conditional scalar dissipation is thus expected to be well predicted until the onset of ignition. The conditional dissipation rates of total enthalpy are from the DNS data, and a model for the conditional dissipation rates of total enthalpy is to be used in actual engine simulation. The improvement of the conditional scalar dissipation model warrants further investigation.

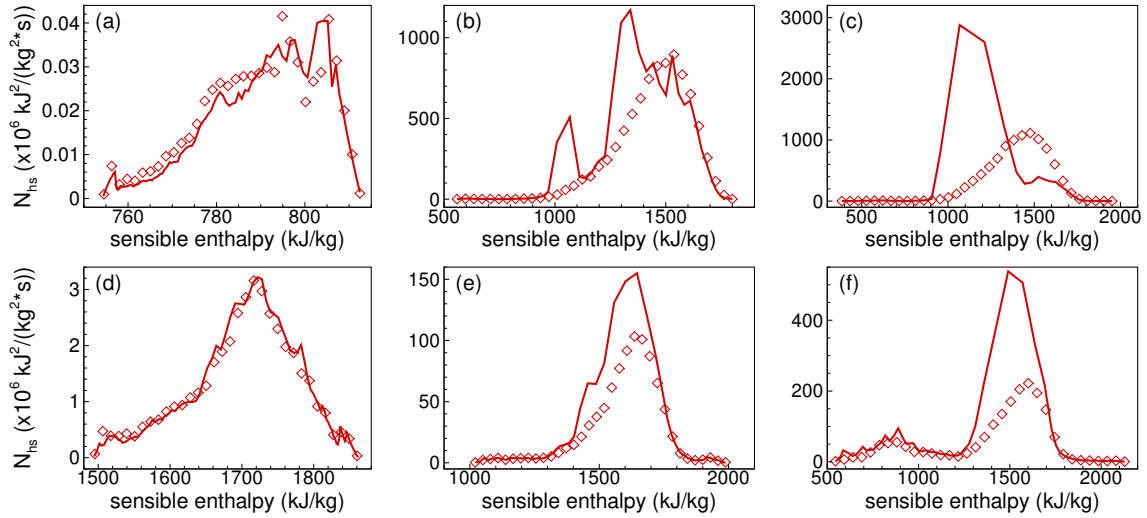


Figure 4.13: Conditional dissipation rates of sensible enthalpy for (a) Case 1 ( $T_0' = 15K$ ) at  $t^* = 0.6$ , (b) Case 3 ( $T_0' = 60K$ ) at  $t^* = 0.6$ , (c) Case 4 ( $T_0' = 100K$ ) at  $t^* = 0.6$ , (d) Case 1 ( $T_0' = 15K$ ) at  $t^* = 0.99$ , (e) Case 3 ( $T_0' = 60K$ ) at  $t^* = 0.99$ , and (f) Case 4 ( $T_0' = 100K$ ) at  $t^* = 0.99$ . (red diamonds: DNS, red solid lines: mapping method)

### Heat release rate

Figure 4.14 shows the time evolution of mean heat release rates for Cases 1, 3, and 4. CMChs produces excellent results when the PDF of sensible enthalpy is taken from DNS. When the PDF of sensible enthalpy is modeled using the mapping method with the presumed beta PDF of total enthalpy, CMChs performs well for Cases 1, 2, and 3 where the initial temperature r.m.s. fluctuations are below 60 K. The monotonic mapping reconstruction, Eqs. (3.63) and (3.64), is used. For Case 4 with the initial temperature r.m.s. fluctuation of 100 K, CMChs overpredicts the mean heat release rates during intermediate stages of ignition, and underpredicts the results near the time when the mean heat release rates reach their maximum. When the PDF of sensible enthalpy is modeled using the mapping method with the total enthalpy PDF taken from DNS, CMChs slightly overpredicts the mean heat release rates during the intermediate stages of ignition. The overprediction is due to the slight overprediction of the PDF across the ignition fronts, as denoted by the black dashed line in Fig. 4.11(h). Even though the overprediction in PDF is small, the heat release rates across the ignition fronts are high, resulting in the slight overprediction in the overall heat release rates in Fig. 4.14(c). Overall, CMChs leads to much improved prediction over CMcht. CMcht performs well when the initial temperature inhomogeneity is small. As the level of temperature inhomogeneity increases, CMcht overpredicts the mean heat release rates.

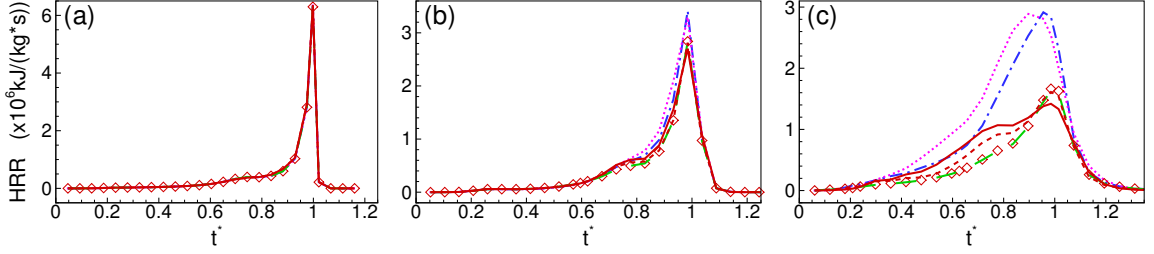


Figure 4.14: Time evolution of total heat release rates for (a) Case 1 ( $T_0' = 15K$ ), (b) Case 3 ( $T_0' = 60K$ ), and (c) Case 4 ( $T_0' = 100K$ ) (red diamonds: DNS, magenta dotted lines: CMCh integrated using the beta PDF for total enthalpy, blue dashed-dotted lines: CMCh integrated using the total enthalpy PDF from DNS data, red solid lines: CMChs integrated using the sensible enthalpy PDF obtained using the mapping method and the beta PDF for total enthalpy, red short-dashed lines: CMChs integrated using the sensible enthalpy PDF obtained using the mapping method and the total enthalpy PDF from DNS data, green long-dashed lines: CMChs integrated using the sensible enthalpy PDF from DNS data)

## 4.4 Validation of CMC Models under SI Engine Knocking Conditions

### 4.4.1 Initial Conditions for the DNS

To validate the enthalpy-based CMC models under knocking condition, *a priori* analysis with 2-D constant volume DNS of PRF-air ignition under stoichiometric conditions data are conducted. The simulation conditions are summarized in Table 4.3.

Case	Fuel	$\phi_0$	$p_0$ (bar)	$\bar{T}_0$ (K)	$T_0'$ (K)	$u'$ (m/s)	$\tau_{ig}$ (ms)	Forcing
7	PRF80	1.0	30	900	20	0.5	2.841	yes
8	PRF80	1.0	30	900	10	0.5	3.212	yes

Table 4.3: Initial and simulation conditions for the DNS cases under knocking conditions. Also shown are the ignition delays

The reduced mechanism for PRF [90] is used, which consists of 861 reactions involving 116 species. The initial pressure,  $p_0$ , are of 30 bar. The initial mean temperature,  $\bar{T}_0$ , is chosen to be in the NTC range for PRF80 fuels. The PRF80 fuel is a mixture of iso-octane and normal heptane, in which the iso-octane takes a volumetric percentage of 80%. The velocity fields are prescribed using the Passot-Pouquet spectrum with  $\bar{u}_0 = 0.0 \text{ m/s}$ ,  $u_0' = 0.5 \text{ m/s}$ , and the most energetic length scale  $l_e = 1.2 \text{ mm}$ . The Kolmogorov length scale for the initial fields are around  $25 \mu\text{m}$ . The temperature field is initialized using a Passot-Pouquet spectrum modified for scalars, with the  $\bar{T}_0$  and  $\bar{T}_0'$  in Table 4.3. The integral length scale of temperature,  $l_{Te}$ , is 1.2 mm for Cases 7, and is 0.6 mm for Case 8. The integral length scale of temperature is reduced for Case 8 to consider the growth of the integral length scale itself in the 2-D mixing.

A periodic computational domain with the size of  $5.0 \text{ mm} \times 5.0 \text{ mm}$  is discretized with  $1024 \times 1024$  grid points initially. This resolution is enough to resolve all the scales before the reactions are substantial. However, the reactive layers become much thinner after the reactions are substantial. From 1-D DNS of freely propagating flames under the initial mean conditions in Table 4.3, the flame fronts are found to be around  $10 \mu\text{m}$ . To fully resolve the thin flame fronts in the stoichiometric cases, the grid is refined to  $3072 \times 3072$  before the reactions are substantial. Due to the more stringent resolution requirement, the computational cost for the stoichiometric cases are more expensive than the lean cases.

In addition to the changes in the resolution, a forcing method is employed in the stoichiometric cases to maintain the turbulence intensity and temperature stratification levels. In the DNS, during the mixing before ignition, the turbulence intensity and thermal stratification will decrease due to decaying. With decaying turbulence,

turbulence level for the DNS configuration can be far from real engine conditions at later stages of simulation, where the end-gas starts igniting. In addition, thermal stratification is known to play a crucial role in end-gas ignition processes. With decaying thermal stratification, the investigation of the thermal stratification effect on ignition can not be quantified. To account for the decaying in turbulence and thermal stratification, the velocity and enthalpy fields are linearly forced before the reactions are substantial to maintain the temperature stratification levels before ignition happens. The forcing method used here follows the idea of linear forcing [89].

#### 4.4.2 Results and Discussion

The enthalpy-based CMC models, CMCh<sub>t</sub> and CMCh<sub>s</sub>, are validated *a priori* with the DNS data. The effects of the choice of a conditioning variable on conditional fluctuations of reacting scalars and the reaction rate closure are investigated. The closure of the PDF and conditional SDR of sensible enthalpy based on the mapping method are also investigated. A normalized sample space variable,  $\xi$ , is used to compare between the results from CMCh<sub>t</sub> and CMCh<sub>s</sub> models. The normalization takes the following form,

$$\xi = \frac{\eta - \eta_{min}}{\eta_{max} - \eta_{min}}, \quad (4.12)$$

where  $\eta$ ,  $\eta_{min}$ , and  $\eta_{max}$  are the sample space variable, its minimum, and maximum of the corresponding enthalpy at a given time, respectively.

##### Temperature and heat release rate evolution

Figure 4.15 shows the temperature and heat release rate evolution for Case 4, 7 and 8. Case 4 is the DNS of n-heptane/air ignition under HCCI conditions, which is summarized in Table 4.1. The results for Case 4 are shown in this section to demonstrate

the more challenging situation for modeling of ignition in the stoichiometric cases than those in the lean cases. As shown in Fig. 4.15, the maximum heat release rates in stoichiometric cases are at least one order of magnitude higher than those in lean cases. Here, the ignition delays  $\tau_{ig}$  are the time duration from the start of simulation till the time when maximum heat release rate happens. The velocity and enthalpy fields in Case 7 and 8 are linearly forced until 2.0 ms and 2.5 ms, respectively. At the time when forcing stop, the meshes are refined from  $1024 \times 1024$  to  $3072 \times 3072$  so that the smallest scales can be well resolved when the reactions are substantial.

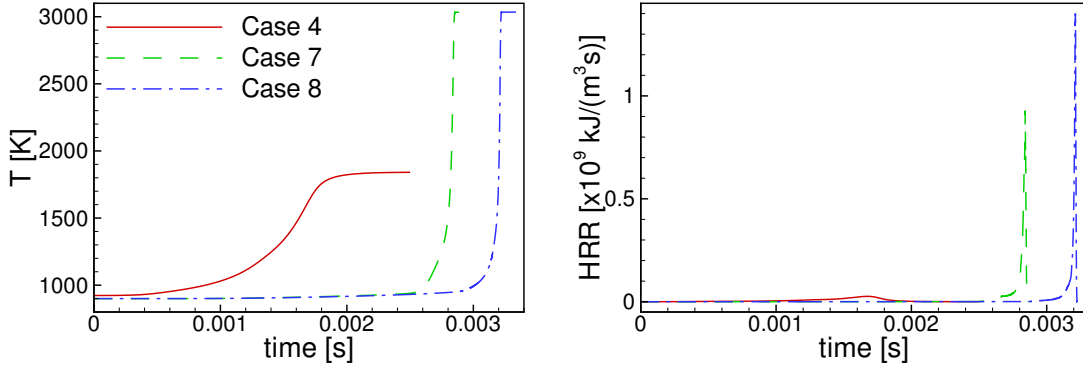


Figure 4.15: Temperature and heat release rate (HRR) evolution for Case 4, 7, and 8.

### Temperature fields

Figure 4.16 shows the temperature fields at various ignition stages, along with iso-scalar surfaces of total enthalpy and of sensible enthalpy. For the iso-scalar surfaces, the value of sensible enthalpy is chosen to demarcate ignition spots. The value used in iso-scalar surfaces of total enthalpy is obtained from the mapping relation in Eq. (3.58). In Fig. 4.16, for Case 7 at  $t^* = 0.6$ , where  $t^*$  is the normalized time,

the iso- $h_s$  and iso- $h_t$  surfaces overlap with each other, indicating that during an early stage of fuel oxidation total enthalpy is well correlated with sensible enthalpy. At  $t^* = 0.88$ , ignition begins to occur in localized spots with higher temperature. At  $t^* = 0.99$ , the iso- $h_t$  surface deviates from the iso- $h_s$  surface in some regions. For Case 8, a similar trend is observed and the results are neglected for brevity.

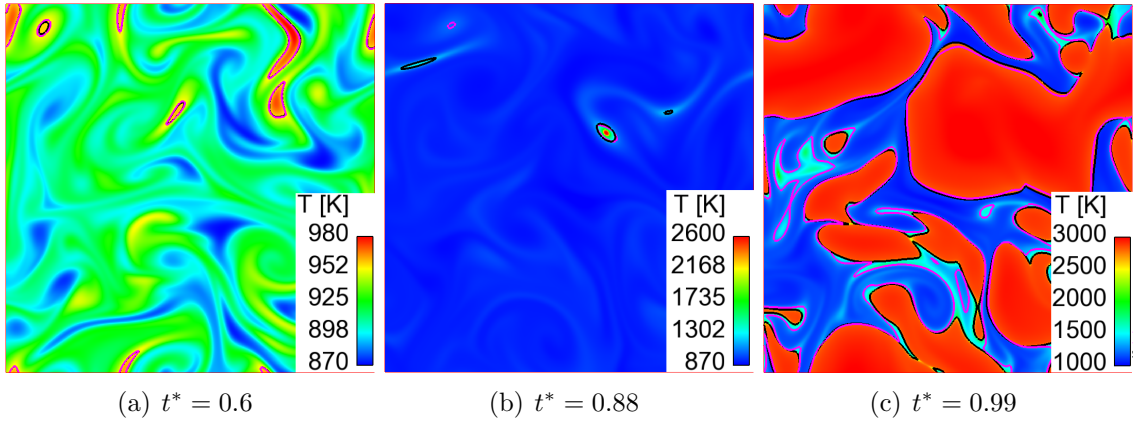


Figure 4.16: Temperature fields and iso-scalar surfaces of sensible enthalpy and of total enthalpy at various stages of ignition for Case 7. (The magenta contour lines represent iso- $h_t$  surfaces, while the black ones represent iso- $h_s$  surfaces.)

### Conditional fluctuations of temperature

Figure 4.17 shows the conditional mean temperature and the conditional r.m.s. fluctuations of temperature. The conditional r.m.s. fluctuations are shown as error bars on top of the corresponding conditional mean temperature. The results at the time  $t^* = 0.99$ , just before the maximum heat release rate approaches, are shown. For the total-enthalpy-based CMC, CMCh<sub>t</sub>, the conditional temperature fluctuations are substantial for the stoichiometric cases even for cases where the initial temperature stratification levels are low. Compared with the lean case Case 4, in which  $T_0' = 100$  K

and the maximum conditional fluctuations are around 200 K, the stoichiometric cases have the maximum conditional fluctuations around 1000 K for CMCh. With large conditional fluctuations, the estimation of chemical reaction rates using the first-order CMC closure may not be accurate enough. For the sensible-enthalpy-based formulation, CMChs, the conditional mean temperature profile is almost linear and the conditional temperature fluctuations are substantially reduced, which implies strong correlation between temperature and sensible enthalpy, as compared with those for CMCh.

### **Heat release rate prediction**

Figure 4.18 shows the conditionally averaged heat release rates at  $t^* = 0.99$ . The conditionally averaged heat release rate is an indicator for overall conditional reaction rates closure. For the lean case Case 4, CMCh gives large errors in the conditional heat release rates prediction for this high level of temperature stratification. For the stoichiometric cases, where even larger temperature conditional fluctuations are observed, CMCh gives substantial errors in the conditional heat release rates prediction even though the temperature stratification levels are low. On the other hand, CMChs gives accurate prediction of the conditional heat release rates for all the cases.

### **PDF and conditional dissipation rates of sensible enthalpy**

Figure 4.19 shows the PDFs of sensible enthalpy and of enthalpy for Cases 7 before ( $t^* = 0.6$ ) and after ( $t^* = 0.99$ ) ignition happens. At  $t^* = 0.6$ , heat release is not substantial, and the field is mixing-dominated. Both enthalpy and sensible enthalpy PDFs resemble the bell shape. At  $t^* = 0.99$ , the sensible enthalpy field is substantially affected by chemical reactions and the PDF has a double-peak shape. The presumed

Beta PDF and the mapping approach correctly capture the development of enthalpy PDF and sensible enthalpy PDF, respectively.

Figure 4.20 shows the conditional dissipation rates of sensible enthalpy for Cases 7 at  $t^* = 0.6$  and  $t^* = 0.99$ . Before substantial heat release happens, the mapping approach results are in good agreement with the DNS results. However, after substantial heat release happens, the mapping approach substantially overpredicts the conditional SDR in most reaction layers due to the strongly non-monotonic mapping between sensible enthalpy and enthalpy. The mapping approach suffers from vanishing gradients at local extrema of the mapping curve. Further investigation is needed to resolve this problem.

## 4.5 Conclusions

The enthalpy-based CMC models are validated *a priori* with 2D DNS data for ignition of lean and stoichiometric homogeneously mixed PRF-air mixtures with temperature inhomogeneity. The major conclusions from the validation studies are:

- The total-enthalpy-based CMC, where enthalpy is taken as the conditioning variable, gives good predictions of the heat release rates in the lean mixtures with low temperature inhomogeneity levels, but leads to substantial overprediction of the heat release rates under the stoichiometric condition regardless of thermal stratification levels.
- The sensible-enthalpy-based CMC is shown to perform well in predicting heat release rates for all conditions considered in this study due to the suppressed conditional temperature fluctuations.

- A mapping method to model conditional SDR and PDF of sensible enthalpy is also assessed. Results show that the mapping method generally well captures the mixing characteristics of sensible enthalpy. The PDF of sensible enthalpy, a reactive scalar, are well modeled in both lean and stoichiometric conditions using the mapping method.
- The mapping method performs well in modeling the conditional SDR of sensible enthalpy in lean conditions. However, due to the existence of strongly non-monotonic mapping, modification is necessary for the modeling of conditional SDR during the ignition of stoichiometric mixtures.

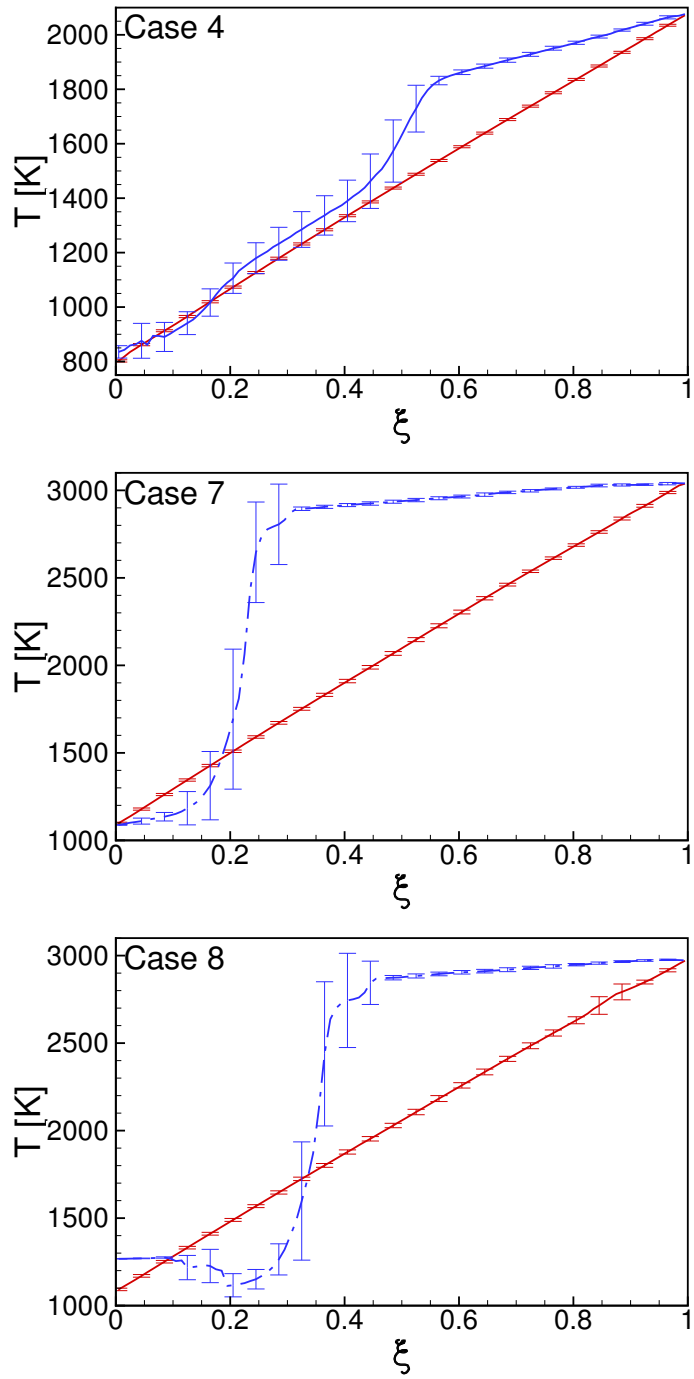


Figure 4.17: Conditional mean and conditional fluctuations of temperature at  $t^* = 0.99$  (red solid lines: CMChs, blue dashed-dotted lines: CMCht, error bars: conditional fluctuations).

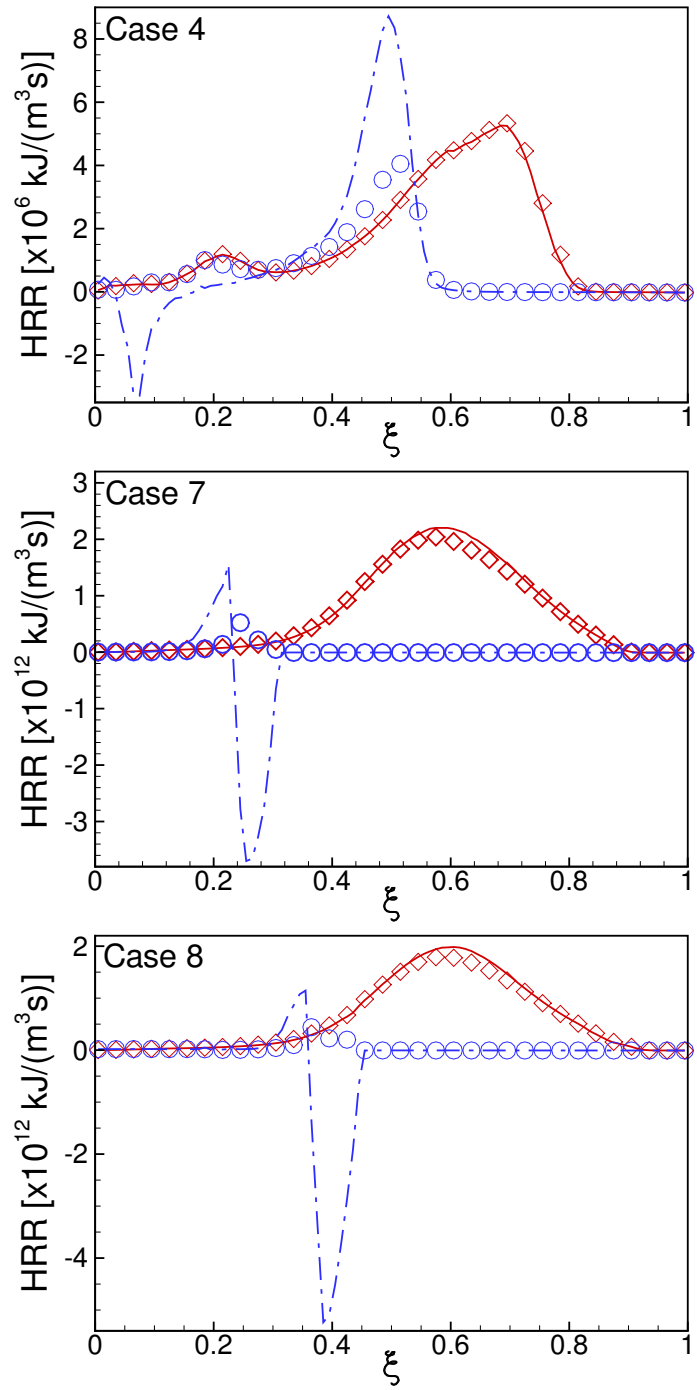


Figure 4.18: Conditional mean heat release rates at  $t^* = 0.99$  (blue circles: DNS data with total-enthalpy conditioning, blue dashed-dotted lines: CMChs model, red diamonds: DNS data with sensible-enthalpy conditioning, red solid lines: CMChs model).

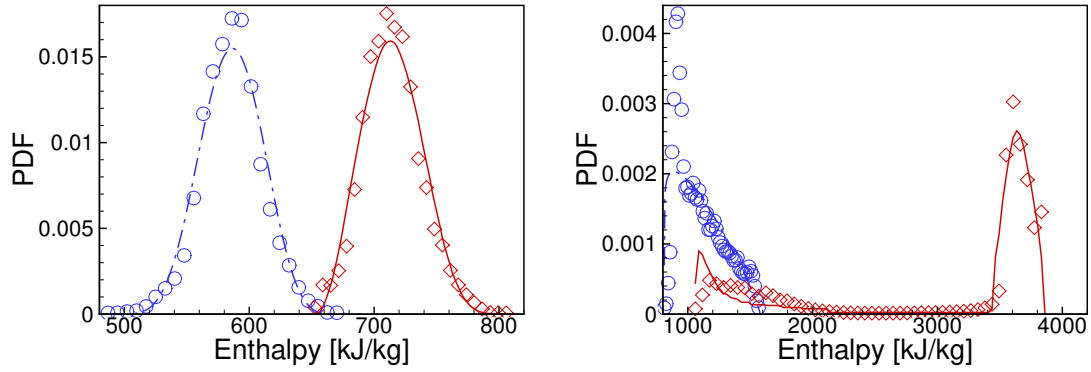


Figure 4.19: PDF of sensible enthalpy and enthalpy for Case 7 at  $t^* = 0.6$  (left), and  $t^* = 0.99$  (right). (blue circles: DNS data with total-enthalpy conditioning, blue dashed-dotted lines: presumed Beta PDF for enthalpy, red diamonds: DNS data with sensible-enthalpy conditioning, red solid lines: mapping-approach modeled PDF for sensible enthalpy.)

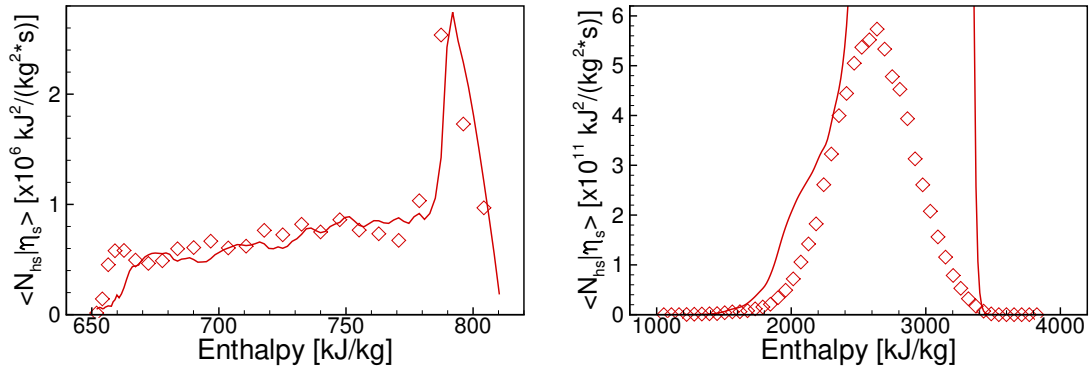


Figure 4.20: Conditional dissipation rates of sensible enthalpy for Case 7 at  $t^* = 0.6$  (left), and  $t^* = 0.99$  (right). (red diamonds: DNS data with sensible-enthalpy conditioning, red solid lines: mapping-approach modeled conditional SDR for sensible enthalpy.)

## **Chapter 5: Application of CMC in LES of Knock using CONVERGE**

In this chapter, the method to apply the CMC model in the prediction of knock in SI engines is presented. Multicycle LES of knocking cases in a GDI engine is conducted using CONVERGE and the spatially-integrated total-enthalpy-based CMC model. The LES results are compared with data from ORNL engine experiments to validate the coupling method and the spatially-integrated total-enthalpy-based CMC model on the prediction of knock in SI engines. In Sec. 5.1, the spatially-integrated total-enthalpy-based CMC model for the prediction of the end-gas auto-ignition in SI engines is described. In Sec. 5.2, the method to apply the CMC model in the prediction of knock in SI engines is described. The CMC model is coupled with a commercial software, CONVERGE, which is responsible for solving the flow fields. In the coupling, the methods to account for the weak mixture inhomogeneity in engine simulations and the pressure-induced oscillation in the enthalpy field in knocking events are presented. A method to reduce the computational cost by solving a subset of species in CONVERGE is developed. In Sec. 5.3, results of multicycle LES of knocking cases in a GDI engine using CONVERGE and the spatially-integrated total-enthalpy-based CMC model are presented. The LES results are compared with data from ORNL engine experiments.

## 5.1 Spatially-Integrated Total-Enthalpy-Based CMC Method for Knock Prediction

### 5.1.1 Spatially-Integrated CMC Method

As described in Ch. 1, knock in SI engines results from the auto-ignition of the end-gas before the consumption by the premixed flame fronts. The term ‘end-gas’ refers to the unburned mixtures ahead of the premixed flame fronts. To accurately predict the occurrence of knock, both the premixed flame propagation and the end-gas auto-ignition should be correctly modeled. In this work, LES is performed to predict the knock occurrence. The propagation of the premixed flame fronts is modeled by the FPF method [61]. And the auto-ignition of the end-gas is modeled by the total-enthalpy-based CMC method with detailed/reduced chemical kinetic mechanisms.

In FPF, the propagation of the flame fronts is described by a filtered progress variable  $\tilde{c}_\psi$ , which is 0.0 in the unburned region and 1.0 in the burned region. The end-gas region can be identified by the end-gas index function,  $H(c_\psi^* - \tilde{c}_\psi)$ , where  $H$  is a Heaviside function and  $c_\psi^* = 0.001$  in this study. When  $\tilde{c}_\psi \leq c_\psi^*$ ,  $H(c_\psi^* - \tilde{c}_\psi)$  is 1.0, indicating the end-gas region. Otherwise  $H(c_\psi^* - \tilde{c}_\psi)$  is 0.0. When there is no premixed flame fronts present, for example the fuel oxidation before the spark discharge in SI engines,  $H(c_\psi^* - \tilde{c}_\psi)$  is 1.0 in the whole cylinder.

With the end-gas index function, the density-weighted conditionally filtered reacting scalar in the end-gas region is defined as,

$$Q_\phi(\eta; t) = \frac{\int \rho \phi \delta(h - \eta) H(c_\psi^* - \tilde{c}_\psi) F(\mathbf{x} - \mathbf{x}') d\mathbf{x}'}{\int \rho \delta(h - \eta) H(c_\psi^* - \tilde{c}_\psi) F(\mathbf{x} - \mathbf{x}') d\mathbf{x}'} \equiv \frac{\langle \rho \phi | \eta \rangle}{\rho_\eta}. \quad (5.1)$$

With this definition, the transport equations for the conditionally filtered species mass fraction  $Q_k(\eta; t)$  can be obtained by integrating the CMC equations, Eq. (3.46),

over the end-gas region:

$$\frac{\partial Q_k}{\partial t} = -v_\eta^* \frac{\partial Q_k}{\partial \eta} + \langle N_\xi | \eta \rangle^* \frac{\partial^2 Q_k}{\partial \eta^2} + \langle W_k | \eta \rangle. \quad (5.2)$$

The filtered scalars in LES,  $\tilde{\phi}(\mathbf{x}, t)$ , can be obtained by integration of the conditional filtered quantities weighted by the FDF of the conditioning variable:

$$\tilde{\phi}(\mathbf{x}, t) = \int_0^1 Q_\phi \tilde{P}(\eta; \mathbf{x}, t) d\eta. \quad (5.3)$$

The FDF  $\tilde{P}(\eta; \mathbf{x}, t)$  has spacial dependencies. The modeling of this local FDF is discussed below in Sec. 5.1.3.

To solve Eq. (5.2) in CMC space and evaluate the filtered scalars in LES using Eq. (5.3), the integrated conditionally filtered reaction rates  $\langle W_i | \eta \rangle$ , local FDF  $\tilde{P}(\eta; \mathbf{x}, t)$ , and the conditionally filtered SDR  $\langle N_\xi | \eta \rangle^*$ , require closure.

### 5.1.2 Closure for Conditional Reaction Rates

Under the assumption that the conditional fluctuations of reactive scalars are small, the integrated conditionally filtered reaction rates can be approximated using the first order CMC:

$$\langle W_i | \eta \rangle = \dot{\omega}_i(\rho_\eta, Q_i, Q_T). \quad (5.4)$$

### 5.1.3 Closure for the Local FDF

As discussed in Sec. 3.2, the mixing statistics of enthalpy, including the FDF and the conditionally filtered SDR, can be approximated using the mixing models for a conserved scalar [54, 105, 13, 145]. Here a Beta function is used to approximate the FDF of enthalpy. The first two moments of enthalpy, the filtered enthalpy  $\tilde{h}_t(\mathbf{x}, t)$ , and its subgrid-scale variance  $\tilde{h}_t''^2(\mathbf{x}, t)$ , are needed to establish the assumed Beta

FDF. The spacial and time dependencies are present in filtered enthalpy and all other filtered quantities in LES. The  $\phi(\mathbf{x}, t)$  is written as  $\phi$  for brevity in below. The filtered enthalpy,  $\tilde{h}_t$ , is resolved and solved for in LES. While the subgrid-scale variance of enthalpy,  $\widetilde{h_t''^2}$ , needs modeling.

In this work, two widely used models for the subgrid-scale variance of passive scalars are implemented. In an algebraic model [107], the subgrid-scale variance of enthalpy is approximated as

$$\bar{\rho}\widetilde{h_t''^2} = C\Delta^2\bar{\rho}|\nabla\tilde{h}_t|^2, \quad (5.5)$$

where  $\Delta$  is the local filter width.  $C$  is a model constant. For simplicity,  $C$  is set to be 0.2 [46], while it can be determined dynamically [107]. In addition to the algebraic model, a transport equation for the subgrid-scale variance of passive scalars by Jimenez *et al.* [55] is also used. The transport equation of the subgrid-scale enthalpy variance can be written as

$$\frac{\partial\bar{\rho}\widetilde{h_t''^2}}{\partial t} + \frac{\partial\bar{\rho}\tilde{u}_i\widetilde{h_t''^2}}{\partial x_i} = \frac{\partial}{\partial x_i}[\bar{\rho}(D + D_T)\frac{\partial\widetilde{h_t''^2}}{\partial x_i}] + 2\bar{\rho}D_T\frac{\partial\tilde{h}_t}{\partial x_i}\frac{\partial\tilde{h}_t}{\partial x_i} - \widetilde{\rho\epsilon_{ht}}, \quad (5.6)$$

where  $D$  and  $D_T$  are the molecular and turbulent diffusivities, respectively.  $\widetilde{\epsilon_{ht}}$  is the subgrid-scale dissipation rate of enthalpy, and is modeled using a classical scaling law below in Sec. 5.1.4.

#### 5.1.4 Closure for the Conditional SDR

The modeling of the SDR of passive scalars is closely related to the modeling of their variance, because the SDR is a sink term in the variance transport equation. In this work, two models for the dissipation rate of enthalpy, which are in accordance with the two models for its variance, are used. In the algebraic model [107], the

normalized filtered dissipation rate is approximated as

$$\widetilde{N}_{ht}(\mathbf{x}, t) = \frac{(D + D_t) \nabla \tilde{h}_t \cdot \nabla \tilde{h}_t}{(\tilde{h}_{tmax} - \tilde{h}_{tmin})^2}, \quad (5.7)$$

where  $\tilde{h}_{tmin}$  and  $\tilde{h}_{tmax}$  are the minimum and maximum of the filtered enthalpy, respectively. The second model for SDR of enthalpy is based on the scaling or dimensional analysis [55]. The filtered SDR of enthalpy is written as

$$\widetilde{N}_{ht}(\mathbf{x}, t) = \widetilde{\epsilon}_{ht} + 2D \frac{\partial \tilde{h}_t}{\partial x_i} \frac{\partial \tilde{h}_t}{\partial x_i} = C_\tau \frac{\tilde{h}_t''^2}{\tau_{ht}} + 2D \frac{\partial \tilde{h}_t}{\partial x_i} \frac{\partial \tilde{h}_t}{\partial x_i}, \quad (5.8)$$

where  $C_\tau$  is a model coefficient, and  $\tau_{ht}$  is a mixing time scale. In the present study,  $C_\tau$  is set to be 10.0, and  $\tau_{ht}$  is estimated as  $\tau_{ht} = \frac{\Delta^2}{D+D_T}$ . The conditional SDR for CMCHt is then obtained as,

$$\langle N_\xi | \eta_t \rangle^* = \frac{\langle \rho \widetilde{N}_{ht}(\mathbf{x}, t) | \eta_t \rangle^*}{\langle \rho | \eta_t \rangle^*}. \quad (5.9)$$

## 5.2 Method to Couple the CMC Model with the Flow Solver for Knock Prediction

In the prediction of knock in SI engines, the CMC model is responsible for modeling the end-gas auto-ignition. The CMC model is coupled with a multidimensional flow solver, which is responsible for solving the flow fields. In the LES of engine knock in this study, a commercial software for 3-D engine simulation, CONVERGE, is used. The spatially-integrated total-enthalpy-based CMC model is coupled with CONVERGE and implemented as UDF. To be consistent with the CONVERGE flow solver, which is a commercial software and the users do not have full access of, a new coupling method is developed. In the coupling with CONVERGE, modifications to the conditioning variable are made to account for the weak mixture inhomogeneity in engine simulations and the pressure-induced oscillation in the enthalpy field in

knocking events. A method to reduce the computational cost by solving a subset of species in CONVERGE is developed.

In the operation or simulation of the GDI engine, different levels of mixture composition stratification may exist near the TDC firing depending on the injection timing and the mixing of evaporated fuel and air. In a homogeneous charge operation, the fuel is injected early in the intake stroke, and a weak level of mixture composition stratification exists near TDC. For instance, in our simulation of an engine experiment under a homogeneous stoichiometric operation, the equivalence ratio,  $\phi$ , ranges mostly between 0.9 and 1.2 near the TDC, while slightly leaner and richer mixtures are also found. The probability distribution of the equivalence ratio from the RANS under a stoichiometric operating condition is shown in Fig. 5.1.

A new coupling method is developed to preserve the mixture composition stratification in the flow solver. The necessity of using the new coupling method rather than the original coupling method, Eq. (5.3), in the spatially-integrated CMC stems from the homogeneous assumption in CMC. The weak mixture composition stratification is modeled in CONVERGE, while in CMC the mixture composition is initialized uniformly under the homogeneous assumption. Using the original coupling method will eliminate the mixture composition stratification in the end-gas. A hybrid coupling method to preserve the mixture composition stratification and to reflect the reaction progress in CMC is developed.

An enthalpy-correction method is applied to the conditioning variable to ensure that the thermal stratification in CMC is consistent with that in CONVERGE. The fluctuation of enthalpy can come from the thermal stratification and the mixture

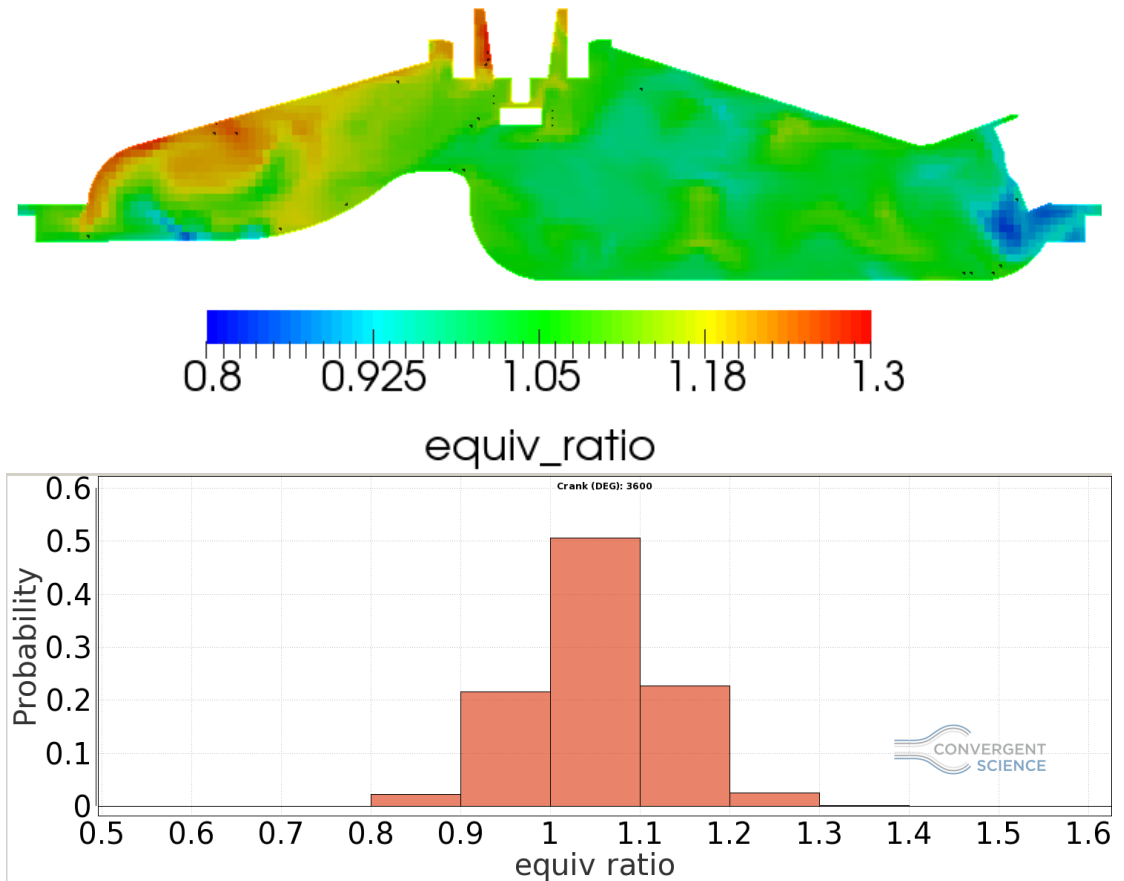


Figure 5.1: In-cylinder equivalence ratio (top) and its probability distribution at TDC (bottom) in RANS.

composition stratification. In CONVERGE, the weak mixture composition stratification is preserved, and the fluctuation of enthalpy comes from both stratifications. In CMC, the mixture composition is initialized uniformly, and the fluctuation of the conditioning variable comes from thermal stratification only. Therefore, using enthalpy from CONVERGE as the conditioning variable leads to inconsistent thermal stratification in CMC and CONVERGE. To remedy this problem, a correction is applied to enthalpy to compensate the dependence of enthalpy on the mixture composition stratification.

In addition to the enthalpy-correction, further modification to the conditioning variable is made by using a pseudoenthalpy when the heat release in the end-gas is substantial. The pseudoenthalpy, which is enthalpy solved under the low Mach number assumption, is used to separate enthalpy fluctuations coming from thermal stratification from the fluctuations induced by pressure wave in knocking events.

Finally, a subset of species, which are the major species responsible for heat release, is solved for in CONVERGE to reduce the computational cost. Since the ignition and turbulence-chemistry interactions are described in CMC, only a subset of species that is responsible for heat release need to be solved in CONVERGE to get the flow fields. A heat-release-based progress variable is proposed to match the heat release in CONVERGE with that in CMC when a subset of species is solved in CONVERGE. This method can save the computational cost in the engine simulation while the prediction of the end-gas auto-ignition is not compromised.

### 5.2.1 Base Approach to Couple the CMC Solver and the CONVERGE Flow Solver

The base approach to couple the CMC solver with the CONVERGE flow solver focuses on ensuring the thermodynamic states of the mixture and the reaction progress in CMC are consistent with those in CONVERGE.

The thermodynamics states of the mixture, including pressure and temperature inhomogeneity, in the flow fields change due to the heat release, heat transfer, piston motion, and mixing. These changes are modeled in CONVERGE and are sent to the CMC solver. Through updating the pressure and temperature inhomogeneity in the CMC solver, the thermodynamic states of the mixture in CMC are consistent with those in CONVERGE.

The chemical reactions in the end-gas region progress under the updated thermodynamic states. The end-gas reaction progress is modeled by the CMC model. To ensure the reaction progress in CONVERGE is consistent with that in CMC, the filtered species mass fractions are updated from CMC solutions through a coupling method. A coupling method that can update the reaction progress and preserve the weak mixture composition stratification in CONVERGE is presented below.

Following Eq. (5.3), the filtered species mass fraction in CONVERGE can be updated as,

$$Coupling - A : \tilde{Y}_i^{n+1} = \int_0^1 Q_i^{n+1} \tilde{P}^n(\eta) d\eta, \quad (5.10)$$

where superscripts  $n$  and  $n + 1$  indicate current step and next step, respectively.  $\tilde{P}(\eta)$  is the local FDF. This coupling is from the original CMC method and referred to as Coupling-A here. In the spatially-integrated CMC method, the conditionally filtered species mass fractions are initialized uniformly, i.e.  $Q_i^0(\eta) = \tilde{Y}_i^u$ , under the

homogeneous mixture assumption. At the first step when CMC is activated, the solution  $Q_i^1$  will be nearly uniform because the end-gas reactions are still at the early stage. Then directly imposing the CMC solutions through Coupling-A will eliminate any mixture composition stratification in CONVERGE.

To preserve the mixture composition stratification in CONVERGE, the coupling is modified

$$\text{Coupling-B} : \tilde{Y}_i^{n+1} = \tilde{Y}_i^n + \int_0^1 (Q_i^{n+1} - Q_i^n) \tilde{P}^n(\eta) d\eta, \quad (5.11)$$

which is referred to as Coupling-B. Coupling-B is preferable when the initial mixture stratification is non-negligible. However, the filtered species mass fractions from Coupling-B are not guaranteed to converge to the final states of the CMC solutions. Thus, when the initial mixture stratification is negligible, Coupling-A is preferable for the numerical stability. Here, to overcome such shortcomings in each coupling method, a hybrid coupling method, Coupling-H, is proposed:

$$\tilde{Y}_i^{n+1} = w \cdot \int_0^1 Q_i^{n+1} \tilde{P}^n(\eta) d\eta + (1.0 - w) \cdot [\tilde{Y}_i^n + \int_0^1 (Q_i^{n+1} - Q_i^n) \tilde{P}^n(\eta) d\eta], \quad (5.12)$$

where  $w$  is a weighting factor.  $w$  is 0 initially. After the end-gas reactions are substantial and the initial mixture stratification is negligible, it increases gradually to 1.0. Such transition is assumed to start when the maximum conditional heat release rate exceeds a threshold.  $w$  is then modeled as

$$w = \begin{cases} 0, & t < t_0 \\ \frac{t}{\tau_h}, & t_0 < t < t_0 + \tau_h \\ 1.0, & t > t_0 + \tau_h \end{cases} \quad (5.13)$$

where  $t_0$  is the time at which the transition between the coupling methods starts, and  $\tau_h$  is a constant to smooth the transition. In the hybrid approach, Coupling-B

is used initially when the mixture stratification is not negligible, while Coupling-A is used at later times when fuel/air mixing has progressed sufficiently.

### 5.2.2 Modifications to Conditioning Variable

#### 5.2.2.1 Enthalpy-Correction to Compensate Enthalpy Fluctuation from Mixture Composition Stratification

In the operation or modeling of the GDI engine, different levels of mixture composition stratification may exist depending on the mixing of evaporated fuel and air. In our simulation of the ORNL engine case under a stoichiometric operation, weak levels of mixture composition stratification are observed. The fluctuation of enthalpy can come from the thermal stratification and the mixture composition stratification. In CONVERGE, the weak mixture composition stratification is preserved, and the fluctuation of enthalpy comes from both stratifications. In CMC, the mixture composition is initialized uniformly, and the fluctuation of the conditioning variable comes from thermal stratification only. Therefore, using enthalpy from CONVERGE as the conditioning variable leads to inconsistent thermal stratification in CMC and CONVERGE. An enthalpy-correction method is developed to compensate the dependence of enthalpy on mixture composition stratification and ensure the thermal stratification in CMC is consistent with that in CONVERGE.

Figure 5.2 shows the dependence of enthalpy on the equivalence ratio for the iso-octane/air mixture at different temperature. For given temperature, enthalpy of the mixture is a linear function of the equivalence ratio, when the differential diffusion effects are negligible. Due to this dependence, the mixture composition stratification introduces enthalpy fluctuations, which affect the evaluation of thermal stratification in CMC.

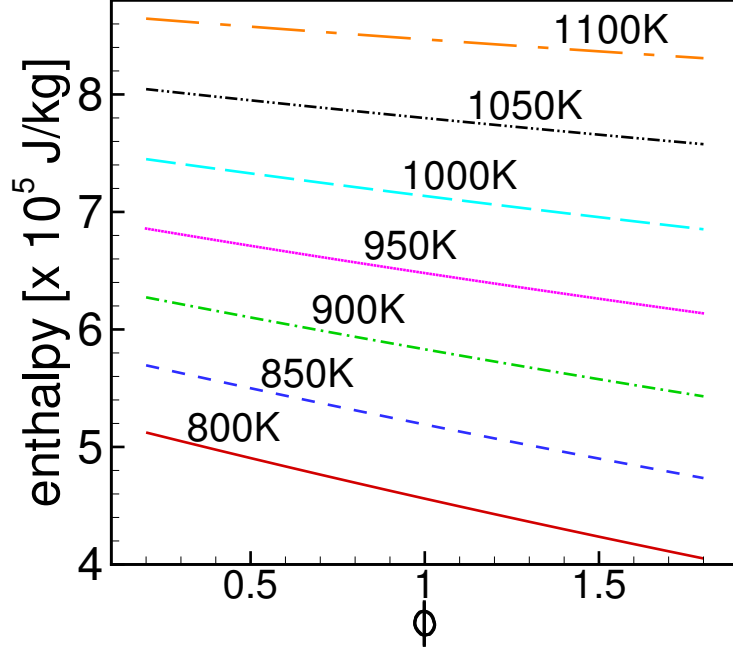


Figure 5.2: Relation of enthalpy  $h_t$  and the equivalence ratio  $\phi$  for the iso-octane/air mixture at different temperature.

An enthalpy-correction method is proposed to compensate the dependence of enthalpy on mixture stratification. The purpose of the compensation is to remove the fluctuations in enthalpy introduced by the weak mixture composition stratification. To reproduce thermal stratification correctly, enthalpy of a mixture with the equivalence ratio  $\tilde{\phi}$  in the flow field is changed to enthalpy of a mixture with the equivalence ratio  $\bar{\phi}$ . During the change, temperature remains the same. Thus, the dependence of enthalpy on the mixture composition stratification is removed, while thermal stratification is preserved. The correction is made based on  $h_t-\phi$  curve for a given value of the temperature  $\tilde{T}$  as,

$$\hat{h}_t = \tilde{h}_t + \frac{\Delta h_t}{\Delta \phi} (\tilde{\phi} - \bar{\phi}), \quad (5.14)$$

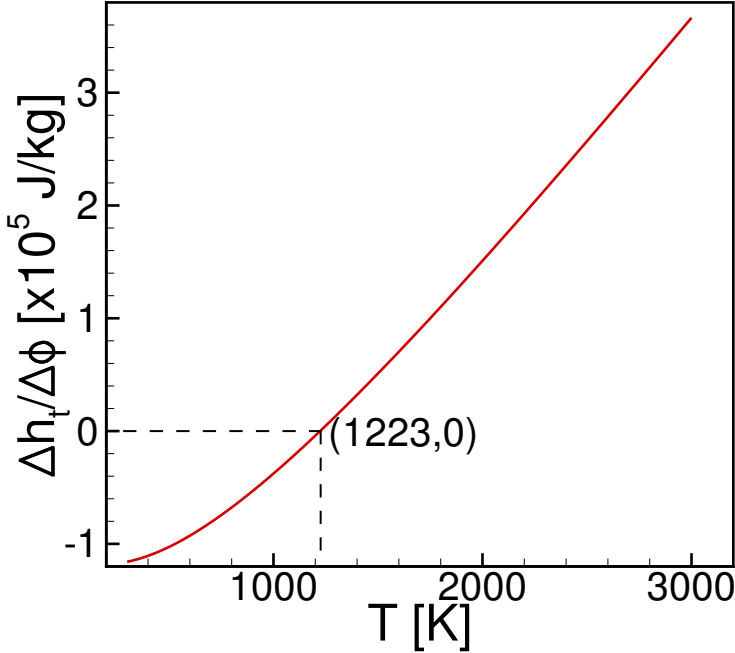


Figure 5.3: Slopes of the  $h_t-\phi$  curves as a function of the temperature for the iso-octane/air mixture.

where  $\hat{h}_t$  is the corrected-enthalpy, and  $\tilde{h}_t$  is the uncorrected enthalpy.  $\frac{\Delta h_t}{\Delta \phi}$  is the slope of the  $h_t-\phi$  relation at given temperature  $\tilde{T}$ , which is shown in Fig. 5.3 for the iso-octane/air mixture.  $\tilde{\phi}$  is the local filtered equivalence ratio and  $\bar{\phi}$  is the equivalence ratio of perfectly-premixed fuel/air mixtures in CMC. When the corrected-enthalpy is used as the conditioning variable, the thermal stratification in the CONVERGE flow field is reproduced in CMC.

### 5.2.2.2 Pseudo-Enthalpy to Separate Pressure-Wave-Induced Enthalpy Fluctuation

In the LES of knock, pressure oscillations will be present when knock occurs. The pressure oscillations in the end-gas region will lead to oscillations in the filtered enthalpy field, which is referred to as the pressure-wave-induced enthalpy fluctuations

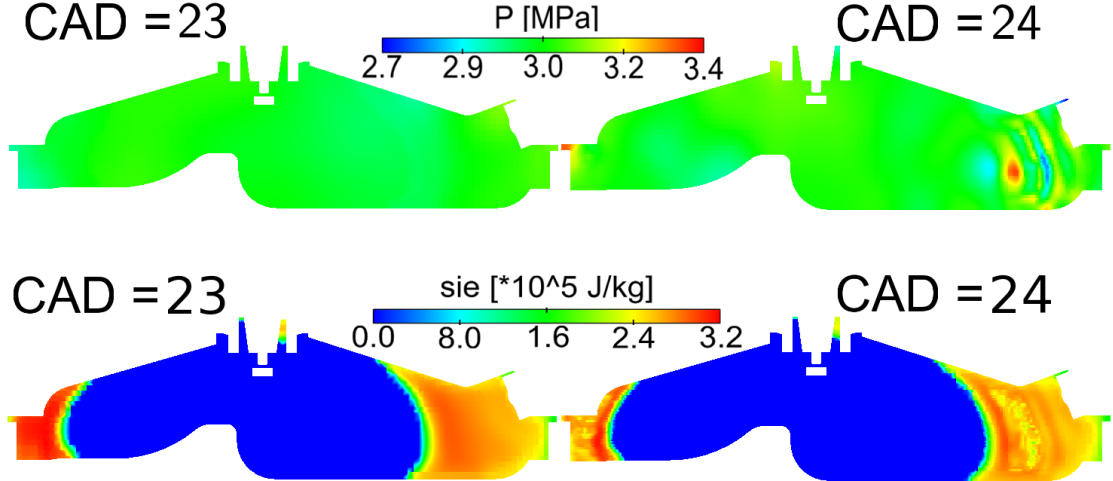


Figure 5.4: Pressure and specific internal energy fields at the time of knocking.

in this work and is due to the pressure-dilatation work. A pseudo-enthalpy, which is enthalpy solved under low Mach number assumption, is used as the conditioning variable when heat release in the end-gas region becomes significant. The use of the pseudo-enthalpy can separate enthalpy fluctuations coming from thermal stratification from the fluctuations induced by pressure wave in knocking events, which ensures the thermal stratification in CMC is consistent with that in CONVERGE when pressure-dilatation work is non-negligible.

Figure 5.4 shows the pressure and specific internal energy (SIE) fields before and at the time of knocking. It can be seen that, before knocking, the pressure field is almost uniform. After the end-gas ignites, pressure oscillations propagate in the end-gas region. This leads to oscillations in the SIE field through the pressure-dilatation work. For the essentially same reason, pressure oscillations lead to fluctuations of enthalpy.

To remedy this problem, the low Mach number assumption is applied to the equation of enthalpy. In other words, instead of enthalpy in a real compressible flow,

the pseudo-enthalpy that separates pressure-wave-induced enthalpy fluctuations from thermal-stratification-related fluctuations is used as a conditioning variable when the heat release becomes significant. For that purpose, in addition to an energy equation solved in CONVERGE, another equation for the pseudo-enthalpy is solved. The pseudo-enthalpy equation can be written as,

$$\frac{\partial \bar{\rho} \tilde{h}_{t,lma}}{\partial t} + \frac{\partial \bar{\rho} \tilde{h}_{t,lma} \tilde{u}_i}{\partial x_i} = \frac{d \tilde{p}^*}{dt} + \frac{\partial}{\partial x_i} \left[ \bar{\rho} (\tilde{D} + D_t) \frac{\partial \tilde{h}_{t,lma}}{\partial x_i} \right], \quad (5.15)$$

where  $\tilde{h}_{t,lma}$  is the pseudo enthalpy,  $\tilde{p}^*$  is the volume-averaged thermodynamic pressure in the end-gas.

For the spatially-integrated total-enthalpy-based CMC model, the filtered enthalpy of the mixture is evaluated from the filtered SIE before heat release and associated pressure oscillation become significant. Once the heat release becomes substantial, the filtered enthalpy is taken from the filtered pseudo enthalpy to separate the pressure-wave-induced enthalpy fluctuations from thermal-stratification-related fluctuations. Thus,

$$\tilde{h}_t = \begin{cases} \tilde{e} + \frac{\tilde{p}}{\bar{\rho}}, & t < t_{threshold} \\ \tilde{h}_{t,lma}, & t \geq t_{threshold}, \end{cases} \quad (5.16)$$

where  $\tilde{e}$  is the filtered SIE solved in the energy equation.  $\tilde{h}_t$  is the filtered enthalpy,  $\tilde{h}_{t,lma}$  is the filtered pseudo enthalpy.  $t_{threshold}$  is the time when the maximum conditional heat release rate reaches a user specified threshold (the same threshold in the transition of the coupling method in Sec. 5.2.1). The pseudo enthalpy field is initialized by the filtered enthalpy field at the transition step to ensure a smooth transition.

### 5.2.3 Reducing Computational Cost by Solving a Subset of Species in CONVERGE

In the LES of knock, a reduced chemical mechanism consisting of about 100 species is used to describe the ignition of iso-octane/air mixtures [101, 152] in CMC. Since the ignition and turbulence-chemistry interactions are described in CMC, it is not necessary to solve the full set of species in the flow solver to get the flow fields. Only a subset of major species that is responsible for heat release can be solved in CONVERGE to get the flow fields. This approach can substantially reduce the computational cost. A heat-release-based progress variable is proposed to match the heat release in CONVERGE with that in CMC when only a subset of species is solved in CONVERGE.

Since the filtered species mass fractions in CONVERGE are updated from the CMC solution, the sum of the filtered mass fractions of the major species will be less than unity. Although the filtered mass fractions can be normalized in CONVERGE to ensure conservation, this simple normalization leads to a mismatched heat release between CONVERGE and CMC. This mismatch in the heat release is found to affect the ignition progress. To deal with this problem, the amount of mass fraction not distributed into the filtered mass fractions in CONVERGE, here referred to as the deficit mass fraction, should be redistributed into the filtered mass fractions based on the reaction progress in CMC.

The deficit mass fraction is defined as,

$$\tilde{Y}_d^* = 1 - \sum_k^{N_m} \int_0^1 Q_k \tilde{P}(\eta) d\eta = 1 - \sum_k^{N_m} \tilde{Y}_k^*, \quad (5.17)$$

where  $\tilde{Y}_d^*$  is the deficit mass fraction that has to be redistributed,  $\tilde{Y}_k^*$  is the filtered species mass fraction before redistribution,  $N_m$  is the number of species solved for in

CONVERGE, i.e. the species subset size. If  $N_m$  equals the total number of species in CMC,  $\tilde{Y}_d$  is zero. This deficit mass fraction is distributed into IC<sub>8</sub>H<sub>18</sub>, O<sub>2</sub>, CO<sub>2</sub>, H<sub>2</sub>O according to the reaction progress in CMC, while satisfying atoms conservation. The stoichiometric coefficients for complete oxidation of IC<sub>8</sub>H<sub>18</sub> and O<sub>2</sub> into CO<sub>2</sub> and H<sub>2</sub>O in the single-step global reaction are used in the distribution.

The reaction progress in CMC can be represented by a progress variable  $c$ . Here, two progress variables are considered: a progress variable based on the filtered fuel mass fraction  $c_f$ , and a progress variable based on the cumulative heat release  $c_h$ . The progress variable based on the filtered fuel mass fraction is defined as

$$c_f = 1.0 - \frac{\tilde{Y}_f^*}{\tilde{Y}_f^u}, \quad (5.18)$$

where  $\tilde{Y}_f^u$  is the filtered unburned fuel mass fraction. The progress variable based on heat release is defined as

$$c_h = \frac{-\sum_i^N \int_0^1 Q_i P(\eta) d\eta h_{f,i} + \sum_i^N \tilde{Y}_i^u h_{f,i}}{-\sum_i^N \tilde{Y}_i^b h_{f,i} + \sum_i^N \tilde{Y}_i^u h_{f,i}}, \quad (5.19)$$

where the summation is done over the whole species set considered in CMC, and  $N$  is the number of species in the whole set.  $\tilde{Y}_i^u$  is the filtered species mass fraction of species  $i$  assuming that the mixture is unburned.  $\tilde{Y}_i^b$  is the filtered mass fraction of species  $i$  assuming that the mixture is completely burned.  $h_{f,i}$  is the enthalpy of formation. The numerator is the local heat release evaluated from CMC solutions, which the denominator is the heat release for when burned completely.

### 5.2.3.1 Results: Effects of Deficit Mass Deposit on Ignition Delay Prediction

The effects of the species subset size and the deficit mass deposit method on the ignition delay prediction are studied. The setup of the cases here are similar to the

DNS validation cases in Ch. 4. The major differences are that the cases studied here are LES simulations using CONVERGE and the spatially-integrated CMCh model. The conditions are summarized below. LES of ignition of homogeneous iso-octane/air mixtures with temperature inhomogeneity in a 2-D constant-volume box are conducted. The computational domain is a square box with a length of 3 mm. The periodic boundary conditions are used. The iso-octane and air mixture with an equivalence ratio of 1.0 is initialized uniformly. The velocity fields are initialized by the Passot-Pouquet spectrum [103] with  $\tilde{u}_0 = 0.0 \text{ m/s}$ ,  $\tilde{u''}_0 = 1.0 \text{ m/s}$ . The temperature field is initialized by the Passot-Pouquet spectrum modified for scalars with  $\tilde{T}_0 = 800 \text{ K}$  and  $\tilde{T''}_0 = 10 \text{ K}$ . The integral length scales for both velocity and temperature fields are 1.2 mm. The dynamic structure model is used for subgrid-scale turbulence modeling. The reduced chemical mechanism for PRF [101, 152] is used. In CONVERGE, three species subsets are considered: the 7 major species ( $\text{C}_8\text{H}_{18}$ ,  $\text{O}_2$ ,  $\text{N}_2$ ,  $\text{CO}_2$ ,  $\text{H}_2\text{O}$ ,  $\text{CO}$ , and  $\text{H}_2$ ), 13 species (7 major species and other minor species), and all the 121 species. Cases with different initial pressures, 20 bar, 30 bar, 40 bar and 50 bar, are studied. The thermodynamic conditions are relevant to engine conditions near TDC.

Figure 5.5 shows the pressure evolution in the LES cases. It can be seen that using 7 major species with the fuel-mass-fraction-based progress variable  $c_f$ , the ignition delays are underpredicted (around 10%) for the four cases. When 13 species are used in CONVERGE, the ignition delays are still underpredicted by around 4%. This underprediction is because of the overprediction of heat release in CONVERGE than that in CMC. This overprediction can be explained by considering the oxidation process in the ignition. The fuel is initially decomposed into intermediates, before

being converted completely into the final combustion products. By using the reaction progress  $c_f$ , all chemical energy contained in the fuel is assumed to be converted into heat completely, neglecting the fuel dissociation and related intermediates. As a result, heat release is overestimated, which leads to the overprediction of pressure rise in CONVERGE. This changes the evolution of enthalpy and thus ignition delay in CMC. The use of the heat-release-based progress variable  $c_h$  is found to substantially improve the prediction of ignition delays. Even when the 7 major species are solved for in CONVERGE, the prediction is within 1% error as compared with that using all the species. Based on this, in LES of knock described below, the 7 major species are solved for in CONVERGE, while the heat-release-based progress variable is used to deposit the deficit mass.

#### 5.2.4 Summary of the Coupling between CMC and CONVERGE

In the prediction of knock in SI engines, the CMC model is responsible for modeling the end-gas auto-ignition, and the CONVERGE flow solver is responsible for solving the flow fields. The coupling between the CMC solver and the CONVERGE flow solver focuses on ensuring the thermodynamic states of the mixture and the reaction progress in CMC are consistent with those in CONVERGE. A hybrid coupling method to preserve the mixture composition stratification and to reflect the reaction progress in CMC is developed. An enthalpy-correction method is developed to separate the enthalpy fluctuation coming from thermal stratification from the fluctuation coming from weak mixture composition stratification. A pseudoenthalpy is used to separate enthalpy fluctuations coming from thermal stratification from the fluctuations induced by pressure wave in knocking events. Through these modifications to the

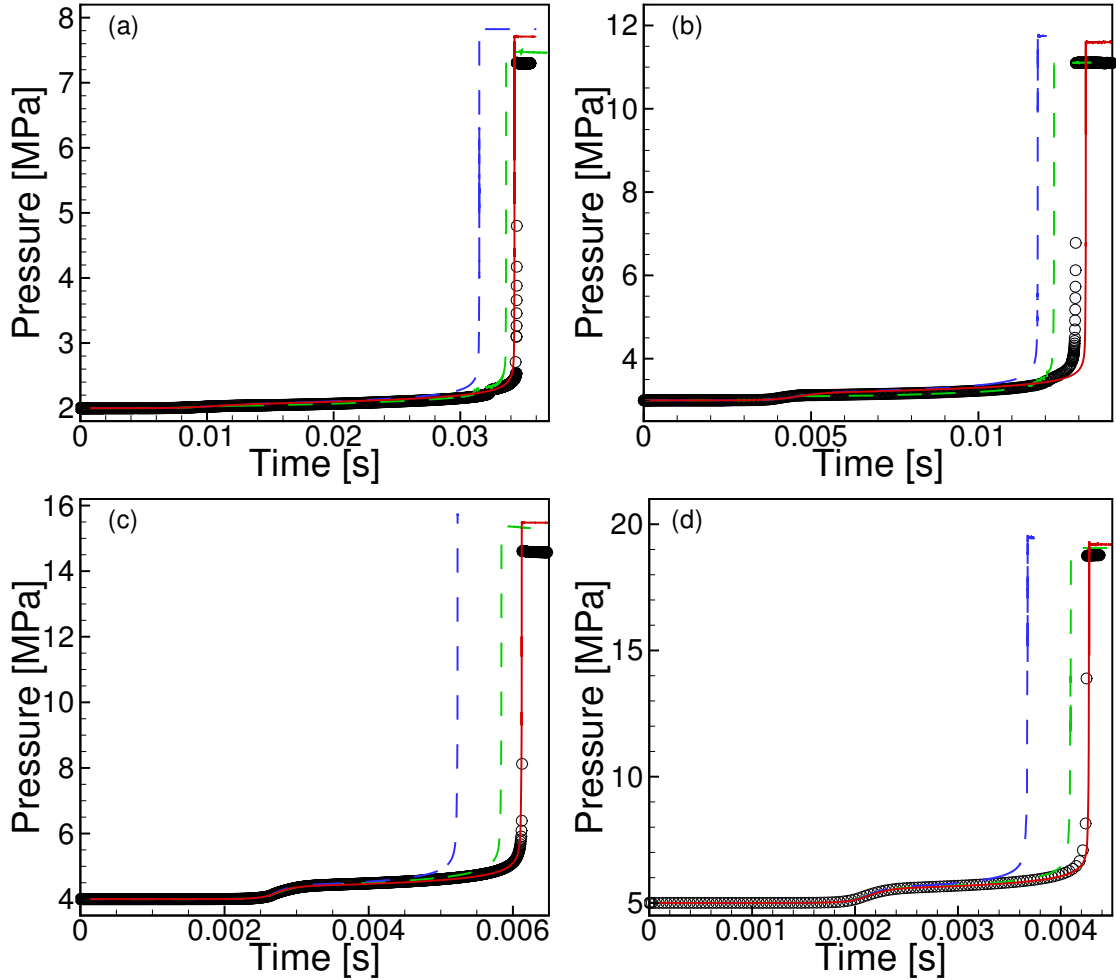


Figure 5.5: Pressure evolution showing the ignition delays for the 2-D constant volume ignition cases. (a)  $P_0 = 20$  bar. (b)  $P_0 = 30$  bar. (c)  $P_0 = 40$  bar. (d)  $P_0 = 50$  bar (Black circles: 121 species, green dashed lines: 13 species with the fuel-mass-fraction-based progress variable for deficit mass deposition, blue dashed lines: 7 major species with the fuel-based progress variable for deficit mass deposition, red solid lines: 7 major species with the heat-released-based progress variable for deficit mass deposition).

conditioning variable, the consistency of thermal stratification is ensured. A method to reduce the computational cost by solving a subset of species in CONVERGE is developed. And a heat-release-based progress variable is proposed to redistribute the deficit mass.

## 5.3 Multicycle LES of Knock in a GDI Engine with Total-Enthalpy-Based CMC for Knock Prediction

To validate the coupling method and the spatially-integrated total-enthalpy-based CMC model on the prediction of knock, multicycle LES of reference knocking cases in a GDI engine is conducted. The results are compared with data from ORNL engine experiments. In the LES of knock, a commercial software for 3-D engine simulation, CONVERGE, is used for solving the flow fields. The CMC model is responsible for modeling the end-gas auto-ignition. The FPF method [61] is responsible for modeling the premixed flame propagation. The FPF method has been implemented into CONVERGE UDF by Yunde Su. In the validation study, the onsets of knock from multicycle LES of the base knocking case are compared with those from experimental data. The effects of the spark timing retarding and wall temperature on the occurrence of knock are also investigated.

### 5.3.1 GDI Engine Specifications and Operating Conditions

The simulations are conducted on a single-cylinder version of the GM LNF 2.0L 4-cylinder-design turbocharged GDI engine. Figure 5.6 shows the geometry of the GDI engine used in the LES. The engine specifications and the operating conditions in this validation study are summarized in Table 5.1. More details about the GDI engine configurations can be found in [138, 133].

The operating conditions for the validation cases selected from the ORNL engine experiments are summarized in Table 5.2. The case R018 is the base knocking case for the validation of the knock prediction. Pressure oscillations were observed in most of cycles in the experiments. In R018, the engine is operated with intake air

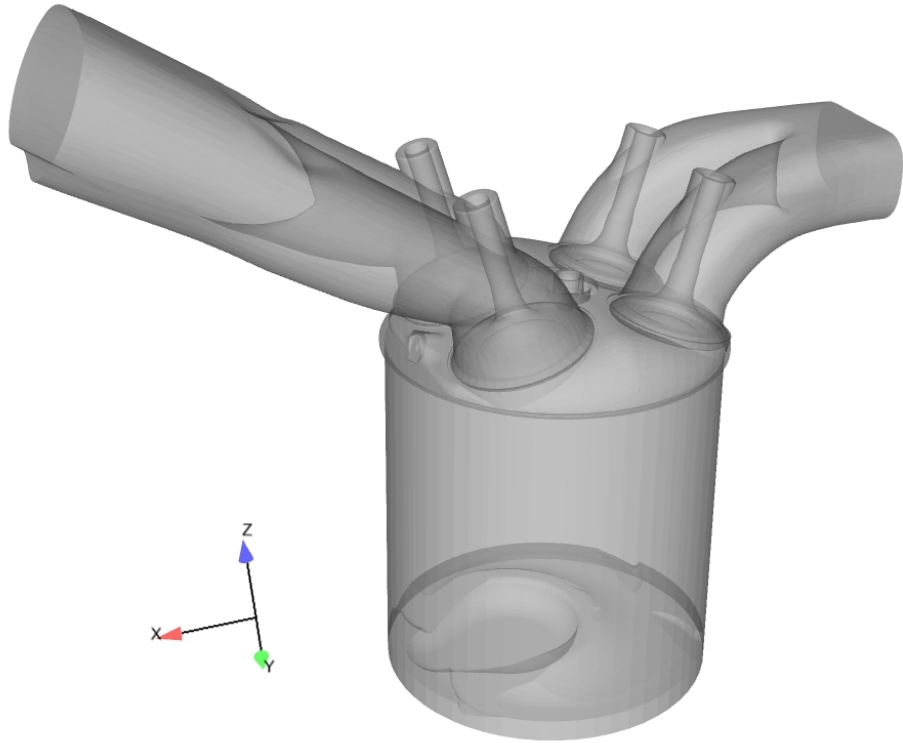


Figure 5.6: Surface geometry of the GM GDI engine used in the LES.

temperature of  $39.10^{\circ}C$  and injection fuel temperature of  $53.28^{\circ}C$ . The flow rates of the air and fuel streams are kept constant in the experiments. The mean intake manifold pressure is 1.41 bar, and the fuel injection pressure is 100 bar. The spark timing (ST) in R018 is at 2.99 crank angle degree (CAD) before TDC. For cases R019 and R020, ST is retarded, while the other conditions remain unchanged from those of R018.

### 5.3.2 Conditions and Models in LES

The base mesh size for the LES is 2.4 mm. The adaptive mesh refinement (AMR) is used in CONVERGE to refine the grids in the cylinder and grids where the scalar

Stroke	86 mm
Bore	86 mm
Connecting Rod	145.5 mm
Compression Ratio	9.0
Fuel	Iso-octane
Equivalence Ratio	1.0
Engine Speed	1000 RPM
Spray Timing	440 CAD
Intake Valve Open (IVO)	308 CAD
Intake Valve Close (IVC)	600 CAD
Exhaust Valve Open (EVO)	130 CAD
Exhaust Valve Close (EVC)	408 CAD

Table 5.1: GDI engine specifications and operating conditions in the LES validation study.

Case	ST (CAD)	$\bar{T}_{airin}$ ( $^{\circ}C$ )	$\bar{P}_{airin}$ (bar)	$\bar{T}_{fin}$ ( $^{\circ}C$ )	knocking
R018	-2.99	39.10	1.41	53.28	strong
R019	-1.59	39.13	1.41	53.27	light
R020	-0.19	39.08	1.41	53.20	no

Table 5.2: Summary of the conditions for the validation cases chosen from the ORNL engine experiments. The spark timing (ST) is relative to TDC firing, which is at 0 CAD. Negative sign indicates the ST is before the TDC.

gradients are large. The fixed embedding [112] is also used to refine the grids in the cylinder and grids in the intake and exhaust systems when the valves are open. After the refinement, the mesh size is 0.6 mm in the cylinder, and 0.3 mm near flame fronts. The total number of computational cells ranges from 2.5 million to 10.5 million. The work by Pal et al. [101] and Robert et al. [114, 115] suggest that a minimum grid size

of about 0.25 mm to 0.5 mm is sufficient for modeling the combustion and knock in SI engines.

The liquid fuel is injected through an injector with six nozzles, whose diameters are 0.39 mm. The injection spray follows a solid-cone spray type, and the size of the droplets at the nozzle exits is determined based on the nozzle diameter. The breakup of the droplets is modeled by the Kelvin-Helmholtz Rayleigh-Taylor (KH-RT) model [110, 58]. The drag on droplets is modeled by the dynamic drop drag model [85, 6]. The Frössling evaporation model [6] is used for the evaporation of the fuel droplets. A wall-film model [100] is used for the spray-wall interaction. The one-equation dynamic structure model [109] is used for the subgrid-scale stresses. For combustion, the FPF method [61] is used to model the premixed flame propagation and the spatially-integrated total-enthalpy-based CMC method is used to model the end-gas auto-ignition. The reduced chemical mechanism for PRF [101, 152], which consists of 121 species and 538 reactions, is used for the hydrocarbon oxidation in CMC. DVODE [21] is used for the time integration of the stiff chemical reaction terms in CMC.

Constant temperature boundary conditions are used for the walls. The wall temperature for different surfaces are summarized in Table 5.3. The wall temperature for different surfaces are determined by referring to the recommended values for engine simulation from CONVERGE, knock modeling literature, and the cooling techniques used for the engine in this study. The cylinder head, liner, and the piston crown are usually well cooled by the coolants, and the temperature are set according to the coolant temperature. The temperature of the spark plug is higher than that of the cylinder head and the value is taken from recommended value from CONVERGE.

Cylinder head	450 K
Cylinder liner	450 K
Piston crown	450 K
Spark plug	600 K
Intake runner	350 K
Intake valve stem	450 K
Intake valve face	550 K
Exhaust runner	725 K
Exhaust valve	725 K

Table 5.3: Wall temperature boundary conditions for the LES.

However, because of the lack of measurements and the insufficient knowledge about the heat transfer on the intake and exhaust valves faces, there are higher uncertainties in determining the wall temperature for the intake valve faces and exhaust valve faces. In this study, a literature review about the wall temperature conditions used in the modeling of knock [94, 101, 114, 33] is performed to try to minimize the uncertainty. From the literature review, the wall temperature for the intake and exhaust valves range from around 500 K to around 800 K. Robert et al. [114] used 784 K for the exhaust valves wall temperature in their LES of knock in an SI engine. Misdariis *et al.* [94] studied the effect of wall temperature on knock using the conjugate heat transfer (CHT) method for the same engine in [114]. And in their case, the wall temperature of the exhaust valves is modeled to be around 690 K. In our study, the exhaust valves wall temperature is set to be 725 K. The engine configuration and operating condition in our study is comparable to those in their work [114, 94].

### **5.3.3 Validation of the Total-Enthalpy-Based CMC Model on Knock Prediction**

#### **5.3.3.1 Verification of the Case Set Up**

Before conducting the multicycle LES, the case set up with the conditions and models summarized before is verified. The verification focuses on comparing the amount of air breathed in per cycle and the cylinder pressure at TDC of the combustion stroke from LES with those from the experimental data. These two parameters have significant influence on determining the mixture composition and thermodynamic conditions in the cylinder. Two consecutive engine cycles for R018 are simulated with the conditions and models described above using LES. The data from the first cycle is discarded, and data from the second cycle is used to compare with the averaged data from the corresponding ORNL experiment. In the experiment, the amount of air breathed into the cylinder is 0.8309 kg per cycle, and the cylinder pressure at TDC of the combustion stroke is 2.46 MPa. These values are cycle-averaged values from the 5000 cycles in the experiment. In the second cycle of the LES, the amount of air breathed in is 0.8289 kg, which is 0.2% less than the cycle-averaged experimental data. The cylinder pressure at TDC after compression is 2.52 MPa, which is 2.4% higher than the cycle-averaged pressure from the experiment.

#### **5.3.3.2 Multi-Cycle LES of a Knocking Case**

LES of sixteen consecutive cycles of the GDI engine is conducted with the conditions and models summarized above. Data from the first cycle is discarded to exclude the influence from the initial conditions. Data from the remaining fifteen consecutive cycles are used to compare with the data from the corresponding ORNL engine experiments. It is to be noted that Robert et al.[114] suggested that fifteen LES cycles

are sufficient to recover the essential statistics of knock in the experiments for their cases.

In the multicycle LES, the total-enthalpy-based CMC model is activated at 30 CAD before TDC, when the mean temperature in the end-gas region reaches around 600 K. It is assumed that the reaction activity below this temperature has negligible influence on the knock occurrence. The transport equation model [55] for the subgrid-scale variance and the associated scalar dissipation rate modeling are used. The threshold of the maximum conditional heat release rate for the transition of the coupling method (from Coupling-B to Coupling-A) and the conditioning variable (from enthalpy evaluated from SIE to pseudo-enthalpy) is taken as  $10 \text{ kJ}/(\text{m}^3\text{s})$ . The bounds of the conditioning variable are clipped based on its probability to reduce the influence of the region with the very low probability to those with higher probability. The values outside the probability range from  $5 \times 10^{-4}$  to  $1 - 5 \times 10^{-4}$  are excluded.

### Scalar Fields during End-Gas Auto-Ignition

The propagation of the premixed flame fronts and the auto-ignition of the end-gas are shown in Fig. 5.7. For R018, the spark is discharged at -2.99 CAD. At 0 CAD, premixed flame fronts develop from the spark kernel and propagate in the cylinder. The turbulent premixed flame fronts are wrinkled by the in-cylinder turbulence, as shown by the isotherm after 15 CAD. The transition and propagation of the premixed flame fronts are modeled by the FPF method. At 24 CAD after TDC (aTDC), the end-gas auto-ignition spots are observed.

Figure 5.8 shows the temperature and fuel mass fraction fields. It can be seen that at the top right corners there are two ignition spots in the end-gas region having temperature over 1500 K and the fuel consumed.

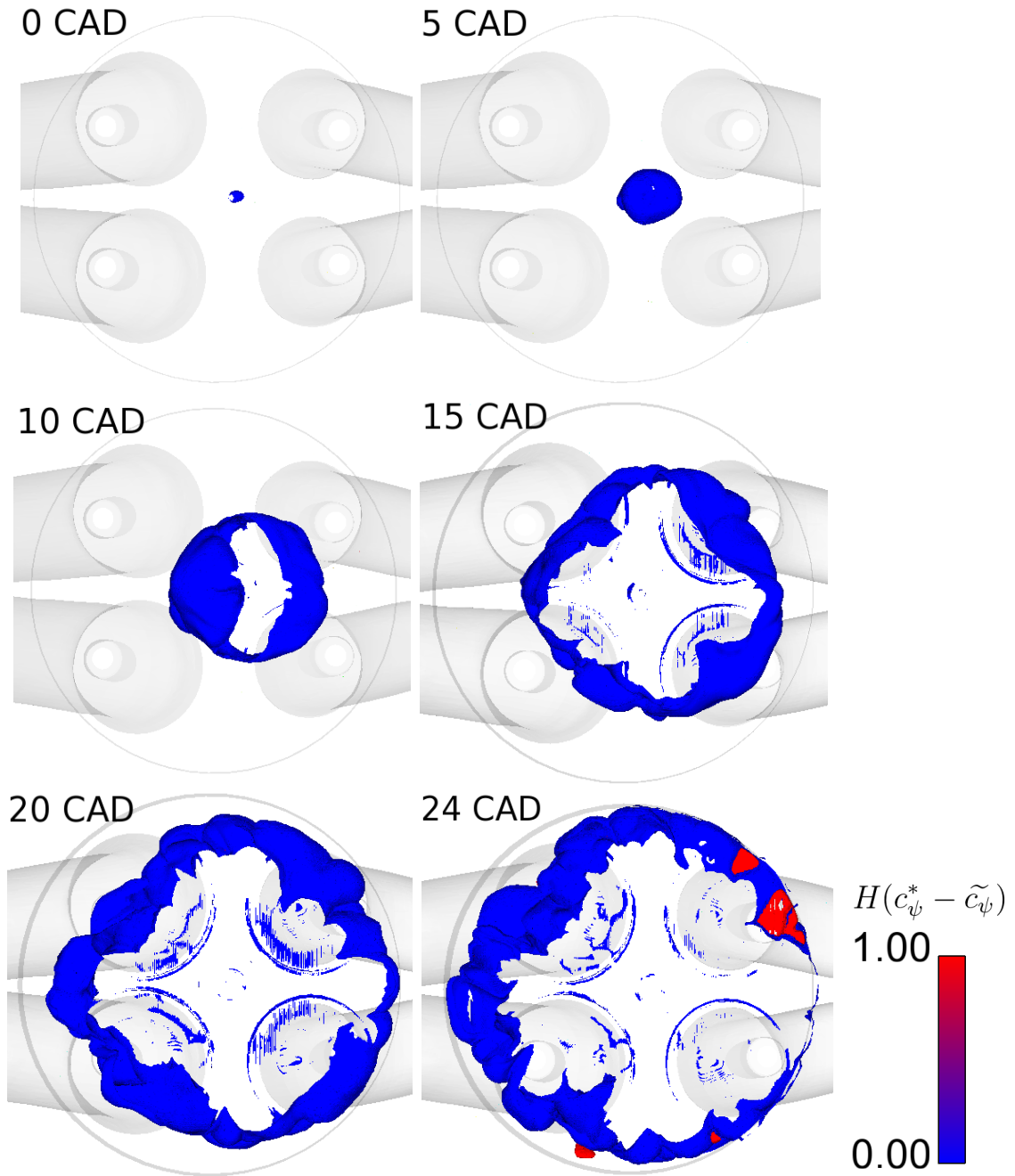


Figure 5.7: Isotherm for temperature of 1500 K, colored by the end-gas index function  $H(c_\psi^* - \tilde{c}_\psi)$  for one LES cycle (Cyc8). In the end-gas region  $H(c_\psi^* - \tilde{c}_\psi)$  is 1.0, otherwise it is 0.0. The isotherm of 1500 K is chosen to represent the the flame fronts of the premixed flame and the ignition fronts of the end-gas auto-ignition. End-gas auto-ignition occur at multiple locations at 24 CAD aTDC, as indicated by the red isotherm. The view is in the positive  $z$  direction, from piston to the cylinder head.

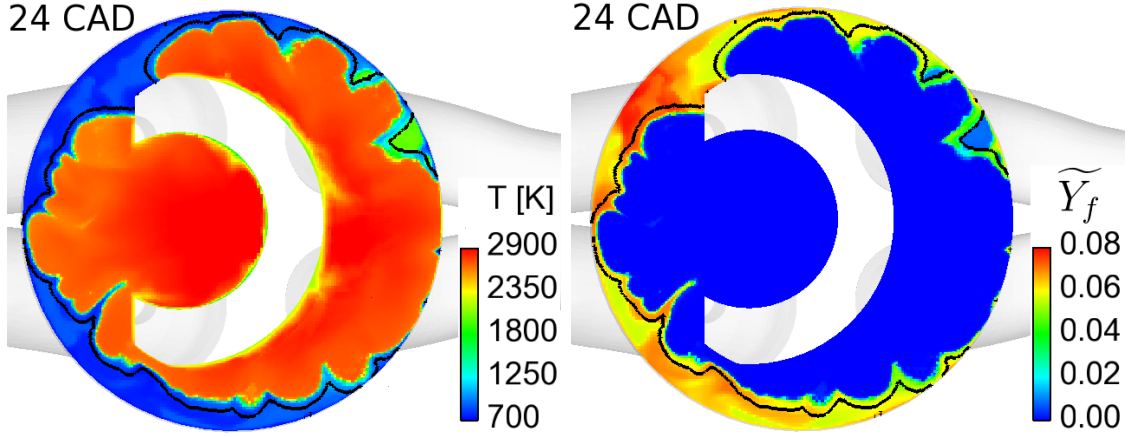


Figure 5.8: Temperature (left) and fuel mass fraction (right) fields at 24 CAD aTDC for Cyc8. The black lines are contours of the progress variable,  $\tilde{c}_\psi$ , of 0.001. In the burned region,  $\tilde{c}_\psi = 1.0$ . In the end-gas region,  $\tilde{c}_\psi < 0.001$ . The region beyond the black contours towards the liner walls are the end-gas region. The fields are on a cut-plane in the  $z$  direction, showing two auto-ignition locations in the end-gas.

Figure 5.9 shows the pressure fields before and after the end-gas auto-ignition. End-gas auto-ignition first occurs at 21 CAD aTDC for Cyc8. At 20 CAD aTDC, the magnitude of the pressure variation on the cut-plane is 0.5 bar. At 25 CAD aTDC, the magnitude of pressure oscillations increases to 2.0 bar. This pressure oscillation is due to the rapid heat release when end-gas auto-ignition occurs.

### Pressure Profile in Multicycle LES of R018

Figure 5.10 shows the in-cylinder pressure at a probed location for the fifteen cycles. The pressure profile from LES are plotted on top of the pressure profile of 50 cycles randomly selected from the 5000 cycles for the experiment R018. The cycle-to-cycle variations (CCV) are well reproduced using the FPF model. Reproducing the CCV is of significant importance in modeling knock. However, the work on CCV is not the focus of this thesis study and is the contribution of others in our research group.

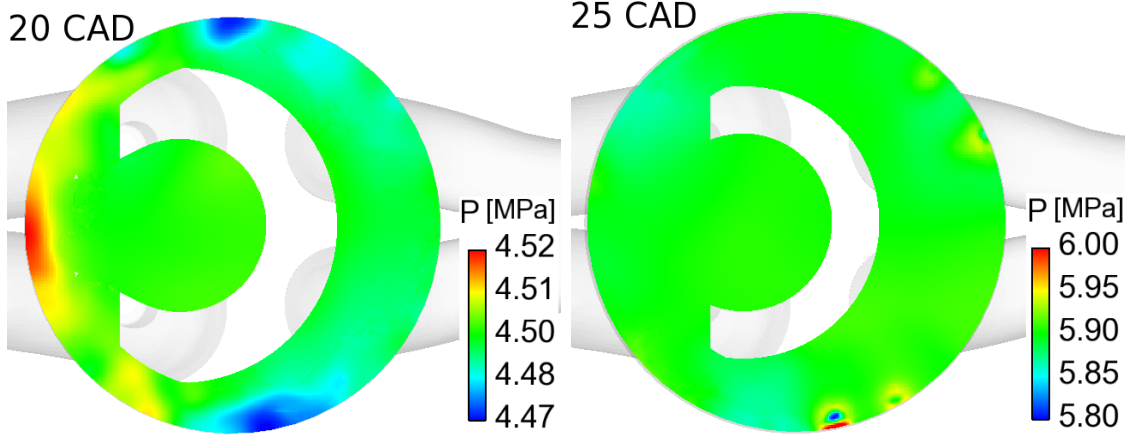


Figure 5.9: Pressure fields at 20 CAD aTDC and at 25 CAD aTDC for Cyc8. End-gas auto-ignition first occurs at 21 CAD aTDC for Cyc8. At 20 CAD aTDC, the magnitude of the pressure variation on the cut-plane is 0.5 bar. At 25 CAD aTDC, the magnitude of pressure oscillations is 2.0 bar. When the pressure oscillation amplitudes exceed 1 bar, it is considered as a knocking cycle in the ORNL experiments.

The discussion on CCV is not included in this work. With the pressure rising due to combustion being well captured by the FPF method, the thermodynamic conditions for the bulk end-gas are considered correctly predicted. Pressure oscillations due to the end-gas auto-ignition are observed in all the fifteen cycles. The pressure oscillations start at around the peaks of the pressure profile, and matches well with those from the experiments. The amplitudes of pressure oscillations are comparable to those in the experimental data. For instance, Fig. 5.11 shows the comparison between the measured pressure from engine experiments and the probed pressure from LES, which clearly demonstrates these statements. The knock occurrence in case R018 is well captured by the total-enthalpy-based CMC model.

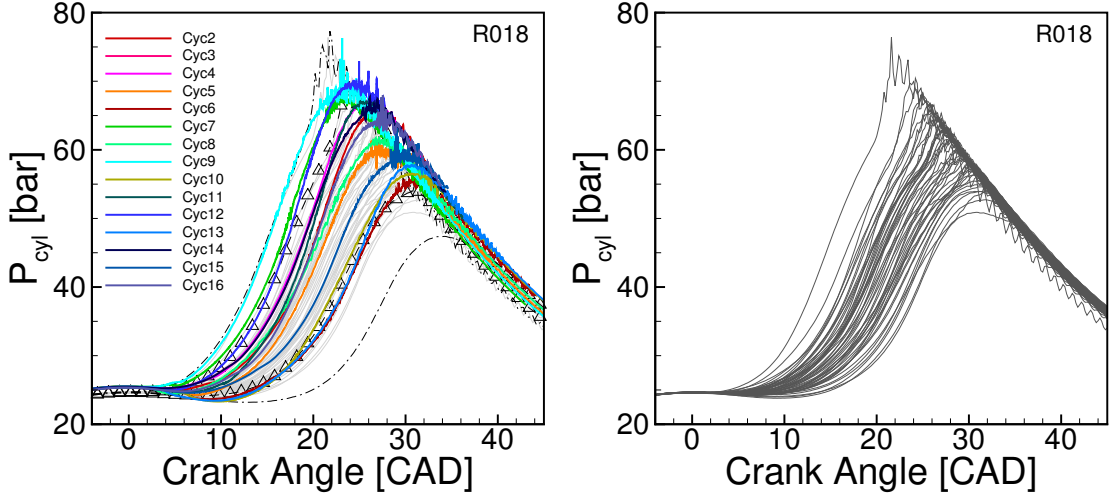


Figure 5.10: In-cylinder pressure evolution in consecutive multicycle LES with total-enthalpy-based CMC for R018 (thin gray lines: measured 50 cycles cylinder pressure randomly selected from 5000 cycles in the ORNL experiment R018, black dashed-dotted lines: fastest and slowest cycles in the experiment, black lines with triangles: 5% and 95% bounds from 5000 cycles in the experiment, thick colored lines: pressure from fifteen consecutive LES cycles). The measured 50 cycles cylinder pressure randomly selected from 5000 cycles in the ORNL experiment R018 are shown in the right figure to display the pressure oscillation amplitudes in experiment.

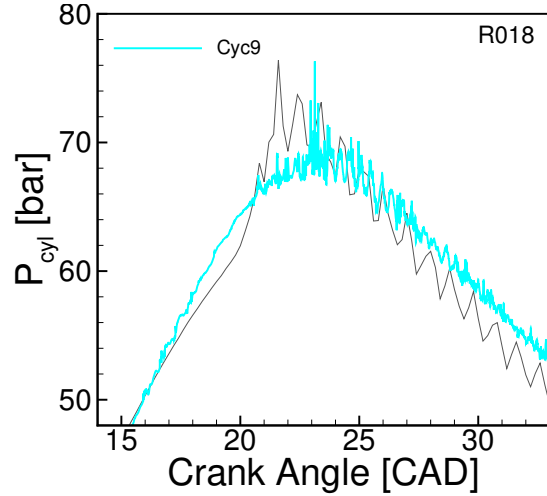


Figure 5.11: Comparison of the measured cylinder pressure from one cycle of engine experiments (grey) and the probed pressure from one cycle of multicycle LES (cyan).

### 5.3.3.3 Spark Timing Sweep

To further validate the total-enthalpy-based CMC model, LES of selected cycles from R018 are restarted with retarded ST. The results from the ST retarding study are compared with the corresponding cases R019 and R020. Five cycles from R018 are selected, two for fast cycles (Cyc11 and Cyc12), two for middle cycles (Cyc5 and Cyc8), and one for a slow cycle (Cyc6). The five cycles are restarted before the discharge of the spark. The ST are retarded according to the experimental setting, and all other models and conditions remain the same as those in the LES of R018.

Figure 5.12 shows the in-cylinder pressure at a probed location for the selected LES cycles. The FPF model well captures the combustion phasing and pressure evolution when the ST is retarded. In R019, the combustion phasing is retarded, and pressure oscillations are observed in all the five selected cycles. Cyc11 displays light pressure oscillations. In R020, the combustion phasing is further retarded, and pressure oscillations with reduced amplitudes are observed in Cyc5, Cyc8, and Cyc12. In Cyc6 and Cyc11, the pressure oscillations are minor. The pressure oscillations also start at around the peaks of the pressure profile for the selected cycles in cases R018-R020, which are in good agreement with the experimental data. However, in cases R019 and R020, the amplitudes of pressure oscillations in LES seem to be larger than those in the experiments. It is to be noted that filtering is applied to the experimental data for pressure, which removes small magnitude high-frequency components.

### 5.3.3.4 Wall Temperature Effect on the Occurrence of Knock

The heat transfer between the charge mixture and the engine walls is a major source of the in-cylinder thermal stratification, which affects knock. In particular, the

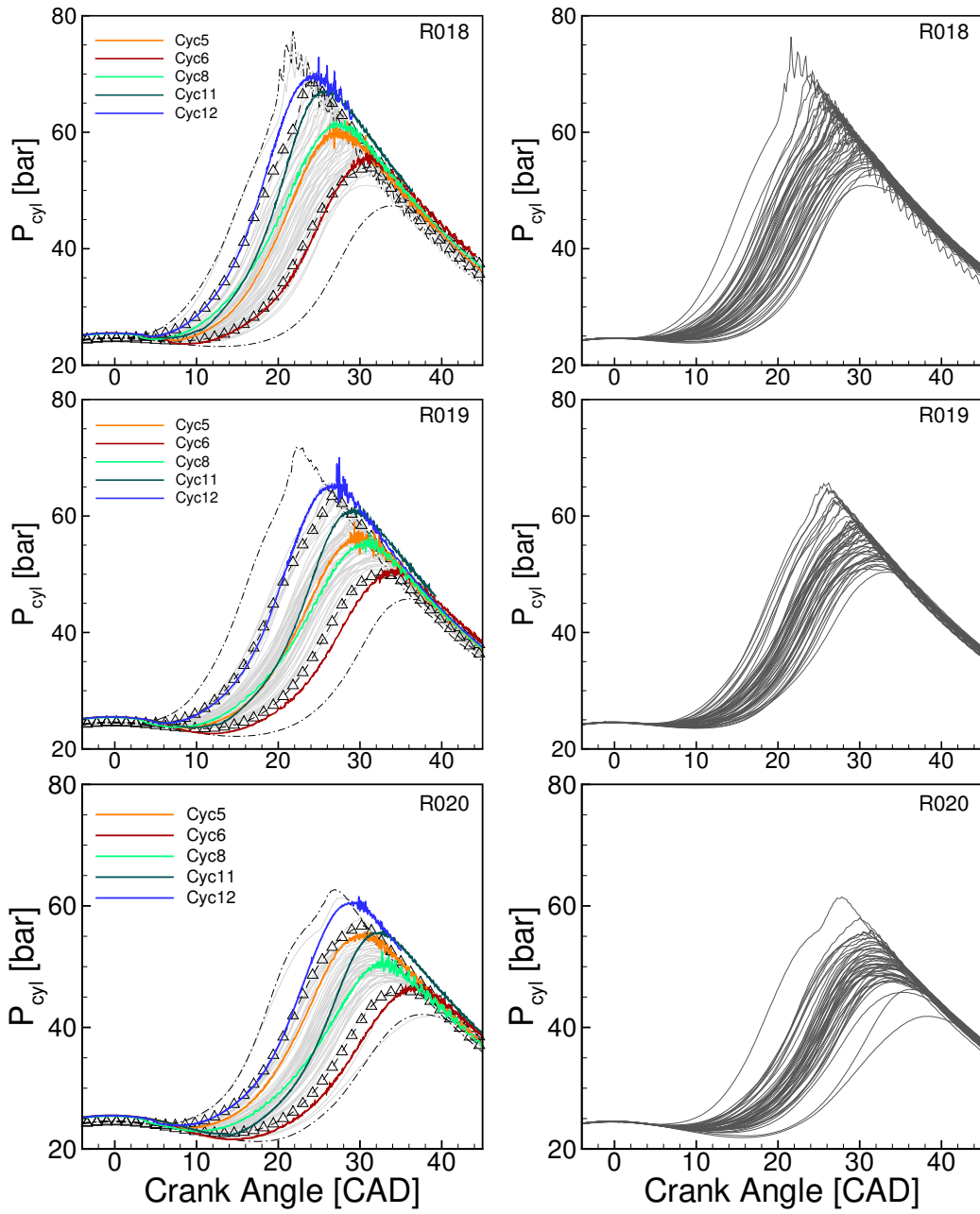


Figure 5.12: In-cylinder pressure evolution for selected cycles for cases R018-R020. The prediction is from consecutive multicycle LES with total-enthalpy-based CMC (thin gray lines: measured 50 cycles cylinder pressure randomly selected from 5000 cycles in the ORNL experiments, black dashed-dotted line: fastest and slowest cycles in the experiment, black lines with triangles: 5% and 95% bounds from 5000 cycles in the experiment, thick colored lines: pressure from selected consecutive LES cycles). In the figures at the right side, only measured pressure curves are shown to better present the amplitude of the pressure oscillations in the experiment.

estimation of the temperature near the exhaust valves, which are usually hotter than other components, can be of importance to the prediction of knock occurrence [114, 94]. For instance, Misdariis *et al.* [94] studied the wall temperature effect on the knock occurrence using the conjugate heat transfer (CHT) method in LES. In their case, they found the temperature of the exhaust valve wall surface is around 610 K when a contact resistance model is not used in the CHT simulation. Knock was not observed due to the underpredicted wall temperature. When a contact resistance model was included, the temperature of the exhaust valve wall increased to around 690 K, and knock occurrence was captured.

To investigate the effect of wall temperature on the occurrence of knock, two cycles, Cyc6 and Cyc8, are selected from the consecutive LES cycles and the simulations are restarted at -360 CAD with the exhaust valve wall temperature being changed. Two wall temperatures, 690 K and 610 K, are chosen for this study and the results are compared with the results from the consecutive LES cycles with the exhaust valve wall temperature of 725 K. The reference temperature, 725 K, is lower than the constant temperature boundary condition used for the exhaust valve in Misdariis *et al.* [94, 114], but is higher than the temperature used in LES with CHT in the same work. The restart timing of -360 CAD corresponds to the early stage of the intake stroke and there is a sufficient time for the thermal stratification to develop. The spark timing is chosen as -0.19 CAD and the corresponding experiment case is R020.

Figure 5.13 shows the in-cylinder pressure evolution at a probed location for the wall temperature effect study. For the exhaust valve wall temperature of 725 K, pressure oscillations are present in both cycles. For the exhaust valve wall temperature of 690 K, pressure oscillations are present in both cycles. However, the pressure

oscillations decrease after the peaks of the pressure profile. As the temperature further decreases to 610 K, knock does not occur in Cyc6, and occurs much later in Cyc8. It is also noted that the burning rates change as the wall temperature changes. This is because the in-cylinder flow field is affected by the wall temperature [94]. For Cyc8, the burning rates increase as the wall temperature of the exhaust valves changes from 725 K to 610 K. The knock is suppressed even with the increase in the burning rate and in-cylinder pressure, indicating the importance of the wall temperature boundary condition in knock prediction. However, the study of the effect of exhaust valves wall temperature on knock is limited in this work. Since the occurrence of knock is a stochastic behavior, multicycle LES needs to be performed to rigorously study the effect of wall temperature on knock. And the effect of the wall models on the heat transfer and turbulent mixing also needs to be studied.

### 5.3.4 Conclusions

The spatially-integrated total-enthalpy-based CMC model for the prediction of knock in SI engines is described. The method to apply the CMC model in the prediction of knock in SI engines is presented. The CMC model is coupled with a multidimensional flow solver, CONVERGE. In the coupling, a method to reduce the computational cost by solving a subset of species in CONVERGE is developed. Multicycle LES of knocking cases in a GDI engine is conducted using CONVERGE and the spatially-integrated total-enthalpy-based CMC model. The LES results are compared with data from ORNL engine experiments to validate the coupling method and the spatially-integrated total-enthalpy-based CMC model on the prediction of knock in SI engines. The end-gas auto-ignition spots are observed in knocking cycles and

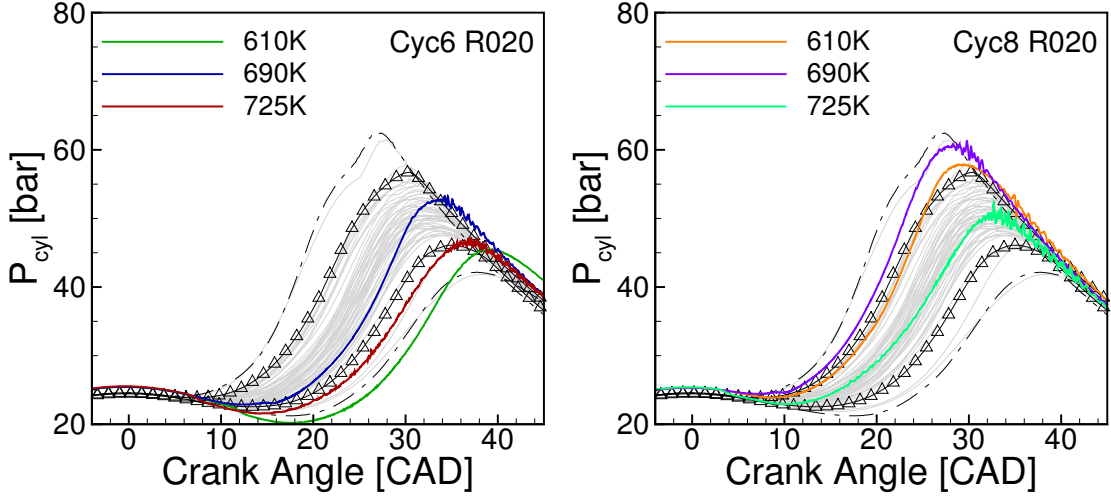


Figure 5.13: Effects of the exhaust valve temperature on knock occurrence in selected consecutive LES cycles (thin gray lines: measured 50 cycles cylinder pressure randomly selected from 5000 cycles in the ORNL experiment, black dashed-dotted lines: fastest and slowest cycles in the experiment, black lines with triangles: 5% and 95% bounds from 5000 cycles in the experiment, thick colored lines: probed pressure from selected consecutive LES cycles; the total-enthalpy-based CMC knock model is used).

the pressure oscillations after the end-gas auto-ignition are captured. Results from multicycle LES of a reference knocking case show that the onsets and the amplitudes of the pressure oscillations match well with those from the experiments. The effects of the ST retarding and wall temperature on the occurrence of knock are also investigated. The trend that ST retarding tends to suppress the occurrence of knock is correctly captured. The onsets of the pressure oscillations in a ST retarded knocking cycle match well with those from the corresponding experiments. While the amplitudes of pressure oscillations in the ST retarded cases seem to be larger than those in the experiments. The change of the wall temperature of the exhaust valves is found to affect the in-cylinder flow field and the burning rates in the cylinder. And knock is suppressed when the wall temperature of the exhaust valves is reduced. Due to uncertainties in thermal boundary conditions on walls, validation in this work is not

conclusive. Multicycle LES with well-defined thermal boundary conditions needs to be performed for more rigorous validation.

## Chapter 6: Summary and Future Work

The accurate prediction of the ignition of premixed mixtures in IC engines is one of the major challenges in the development of advanced engine technologies. The CMC method has potential in modeling the ignition of premixed mixtures accurately. This study aims at applying the CMC method to the ignition of premixed mixtures with temperature inhomogeneity under HCCI and SI engine knocking conditions. The major contributions of this thesis work are summarized as follows:

- A CMC model based on sensible enthalpy is developed for the ignition of premixed mixtures with temperature inhomogeneity under IC engine conditions. The motivation of using sensible enthalpy as the conditioning variable is that sensible enthalpy is strongly correlated with temperature. The ignition of premixed mixtures is governed by chemical kinetics, which show strong nonlinear-dependence on temperature. Using sensible enthalpy as the conditioning variable, the conditional fluctuations of temperature are expected to be small and the estimation of the reaction rates can be made accurate. The accurate prediction of the mean reaction rates also requires closure of the PDF and conditional SDR of the conditioning variable. A mapping method is proposed to model these mixing statistics of sensible enthalpy.

- The enthalpy-based CMC methods are validated on the prediction of ignition of premixed mixtures under HCCI conditions and SI engine knocking conditions through an *a priori* analysis using 2-D DNS data. Results show that the total-enthalpy-based CMC gives good predictions of the HRR under HCCI conditions with low temperature inhomogeneity levels, but leads to substantial overprediction of the HRR under SI engine knocking conditions regardless of thermal stratification levels. The sensible-enthalpy-based CMC is shown to perform well in predicting HRR for all conditions considered in this study due to the suppressed conditional temperature fluctuations. The proposed mapping method generally well captures the mixing characteristics of sensible enthalpy.
- A method to apply the CMC model in the prediction of knock in SI engines is developed. The CMC model is coupled with a multidimensional flow solver, CONVERGE. In the coupling with CONVERGE, a hybrid coupling method is developed to account for the weak mixture inhomogeneity in engine simulations. Modifications to the conditioning variable are made to compensate the dependence of enthalpy on the weak mixture composition stratification and the pressure-induced oscillation in the enthalpy field in knocking events. A method to reduce the computational cost by solving a subset of species in CONVERGE is developed.
- The coupling method and the spatially-integrated total-enthalpy-based CMC model are validated on the prediction of knock in a GDI engine. Multicycle LES of knocking cases in a GDI engine is conducted using CONVERGE and the spatially-integrated total-enthalpy-based CMC model. The results are

compared with data from ORNL engine experiments. The end-gas auto-ignition spots are observed in knocking cycles and the pressure oscillations after the end-gas auto-ignition are captured. Results from multicycle LES of knocking cases show that the onsets of the pressure oscillations match well with those from the experiments. The amplitudes of pressure oscillations in the reference knocking case match well with those from the experiments. While in the ST retarded cases the amplitudes seem to be larger than those in the experiments. The effects of the ST retarding and wall temperature on the occurrence of knock are also investigated. The trend that ST retarding tends to suppress the occurrence of knock is correctly captured. The knock model developed in this work shows the potential to investigate the effect of wall temperature on knock.

In the future, the potential of the enthalpy-based CMC models in the prediction of knock in SI engines will be further investigated. Multicycle LES of knocking cases in the GDI engine with the spatially-integrated sensible-enthalpy-based CMC model will be conducted. Multicycle LES of the GDI engine operated at different loads and engine speeds will be conducted with the spatially-integrated enthalpy-based CMC models. The effect of EGR on knock occurrence will also be investigated. The results will be compared with data from ORNL engine experiments to systematically study the potential of spatially-integrated enthalpy-based CMC models in the prediction of knock in SI engines.

## Bibliography

- [1] Salvador M Aceves, Daniel L Flowers, Francisco Espinosa-Loza, Joel Martinez-Frias, John E Dec, Magnus Sjöberg, Robert W Dibble, and Randy P Hessel. Spatial analysis of emissions sources for HCCI combustion at low loads using a multi-zone model. *SAE Transactions*, pages 1014–1024, 2004.
- [2] Salvador M Aceves, Daniel L Flowers, Francisco Espinosa-Loza, Joel Martinez-Frias, Robert W Dibble, Magnus Christensen, Bengt Johansson, and Randy P Hessel. Piston-liner crevice geometry effect on HCCI combustion by multi-zone analysis. *SAE Transactions*, pages 2691–2698, 2002.
- [3] Salvador M Aceves, Daniel L Flowers, Charles K Westbrook, J Ray Smith, William Pitz, Robert Dibble, Magnus Christensen, and Bengt Johansson. A multi-zone model for prediction of HCCI combustion and emissions. SAE Technical Paper 2000-01-0327, 2000.
- [4] SM Aceves, JR Smith, CK Westbrook, and WJ Pitz. Compression ratio effect on methane HCCI combustion. *Journal of Engineering for Gas Turbines and Power*, 121(3):569–574, 1999.
- [5] Avinash Kumar Agarwal, Akhilendra Pratap Singh, and Rakesh Kumar Mau-rya. Evolution, challenges and path forward for low temperature combustion engines. *Progress in Energy and Combustion Science*, 61:1–56, 2017.
- [6] Anthony A Amsden, Peter J Orourke, and T Daniel Butler. KIVA-2: A computer program for chemically reactive flows with sprays. *NASA STI/recon technical report N*, 89, 1989.
- [7] Shokri Amzin, N Swaminathan, JW Rogerson, and JH Kent. Conditional moment closure for turbulent premixed flames. *Combustion Science and Technology*, 184(10-11):1743–1767, 2012.
- [8] Hultqvist Anders, Magnus Christensen, Bengt Johansson, Axel Franke, Mattias Richter, and Marcus Aldén. A study of the homogeneous charge compression ignition combustion process by chemiluminescence imaging. SAE Technical Paper 1999-01-3680, 1999.

- [9] A Babajimopoulos, DN Assanis, DL Flowers, SM Aceves, and RP Hessel. A fully coupled computational fluid dynamics and multi-zone model with detailed chemical kinetics for the simulation of premixed charge compression ignition engines. *International journal of engine research*, 6(5):497–512, 2005.
- [10] H Barths, C Felsch, and N Peters. Mixing models for the two-way-coupling of CFD codes and zero-dimensional multi-zone codes to model HCCI combustion. *Combustion and Flame*, 156(1):130–139, 2009.
- [11] Frédérique Battin-Leclerc. Detailed chemical kinetic models for the low-temperature combustion of hydrocarbons with application to gasoline and diesel fuel surrogates. *Progress in Energy and Combustion Science*, 34(4):440–498, 2008.
- [12] Amit Bhave, Michael Balthasar, Markus Kraft, and Fabian Mauss. Analysis of a natural gas fuelled homogeneous charge compression ignition engine with exhaust gas recirculation using a stochastic reactor model. *International Journal of Engine Research*, 5(1):93–104, 2004.
- [13] RW Bilger. Turbulent diffusion flames. *Annual Review of Fluid Mechanics*, 21(1):101–135, 1989.
- [14] RW Bilger. Conditional moment closure for turbulent reacting flow. *Physics of Fluids A: Fluid Dynamics*, 5(2):436–444, 1993.
- [15] Fabrizio Bisetti, J-Y Chen, Evatt R Hawkes, and Jacqueline H Chen. Probability density function treatment of turbulence/chemistry interactions during the ignition of a temperature-stratified mixture for application to HCCI engine modeling. *Combustion and Flame*, 155(4):571–584, 2008.
- [16] Michele Bolla, Daniele Farrace, Yuri M Wright, and Konstantinos Boulouchos. Modelling of soot formation in a heavy-duty diesel engine with conditional moment closure. *Fuel*, 117:309–325, 2014.
- [17] Michele Bolla, Yuri M Wright, Konstantinos Boulouchos, Giulio Borghesi, and Epaminondas Mastorakos. Soot formation modeling of n-heptane sprays under diesel engine conditions using the conditional moment closure approach. *Combustion Science and Technology*, 185(5):766–793, 2013.
- [18] Derek Bradley and RA Head. Engine autoignition: The relationship between octane numbers and autoignition delay times. *Combustion and Flame*, 147(3):171–184, 2006.
- [19] Derek Bradley, Chris Morley, and HL Walmsley. Relevance of research and motor octane numbers to the prediction of engine autoignition. Technical report, SAE Technical Paper, 2004.

- [20] Sebastiano Breda, Alessandro D’Adamo, Stefano Fontanesi, Nicola Giovannoni, Francesco Testa, Adrian Irimescu, Simona Merola, Cinzia Tornatore, and Gerardo Valentino. CFD analysis of combustion and knock in an optically accessible GDI engine. *SAE Int. J. Engines*, 9(2016-01-0601):641–656, 2016.
- [21] Peter N Brown, George D Byrne, and Alan C Hindmarsh. VODE: A variable-coefficient ODE solver. *SIAM journal on scientific and statistical computing*, 10(5):1038–1051, 1989.
- [22] C Carey, M McAllister, M Sandford, S Richardson, S Pierson, N Damton, S Bredda, Sam Akehurst, Chris Brace, J Turner, et al. Extreme engine downsizing. *Innovations in Fuel Economy and Sustainable Road Transport*, pages 135–147, 2011.
- [23] Longhua Chen, Tie Li, Tao Yin, and Bin Zheng. A predictive model for knock onset in spark-ignition engines with cooled egr. *Energy Conversion and management*, 87:946–955, 2014.
- [24] Stephane Chevillard, Olivier Colin, Julien Bohbot, Mingjie Wang, Eric Pomraning, and PK Senecal. Advanced methodology to investigate knock for downsized gasoline direct injection engine using 3D RANS simulations. SAE Technical Paper 2017-01-0579, 2017.
- [25] Magnus Christensen and Bengt Johansson. The effect of in-cylinder flow and turbulence on HCCI operation. Technical report, SAE Technical Paper, 2002.
- [26] Magnus Christensen, Bengt Johansson, Per Amnéus, and Fabian Mauss. Supercharged homogeneous charge compression ignition. *SAE Transactions*, pages 1129–1144, 1998.
- [27] J Clarkson, JF Griffiths, JP MacNamara, and BJ Whitaker. Temperature fields during the development of combustion in a rapid compression machine. *Combustion and Flame*, 125(3):1162–1175, 2001.
- [28] Olivier Colin, António Pires da Cruz, and Stéphane Jay. Detailed chemistry-based auto-ignition model including low temperature phenomena applied to 3-D engine calculations. *Proceedings of the Combustion Institute*, 30(2):2649–2656, 2005.
- [29] David J Cook and Heinz Pitsch. Enthalpy-based flamelet model for HCCI applied to a rapid compression machine. *SAE Transactions*, pages 1558–1565, 2005.
- [30] David J Cook, Heinz Pitsch, Jacqueline H Chen, and Evatt R Hawkes. Flamelet-based modeling of auto-ignition with thermal inhomogeneities for application

- to HCCI engines. *Proceedings of the Combustion Institute*, 31(2):2903–2911, 2007.
- [31] A Pires Da Cruz. Three-dimensional modeling of self-ignition in HCCI and conventional diesel engines. *Combustion Science and Technology*, 176(5-6):867–887, 2004.
  - [32] Alessandro d’Adamo, Sebastiano Breda, Stefano Fontanesi, and Giuseppe Cantore. A RANS-based CFD model to predict the statistical occurrence of knock in spark-ignition engines. *SAE International Journal of Engines*, 9(1):618–630, 2016.
  - [33] Alessandro d’Adamo, Sebastiano Breda, Salvatore Iaccarino, Fabio Berni, Stefano Fontanesi, Barbara Zardin, Massimo Borghi, Adrian Irimescu, and Simona Merola. Development of a RANS-based knock model to infer the knock probability in a research spark-ignition engine. *SAE International Journal of Engines*, 10(3):722–739, 2017.
  - [34] G De Paola, E Mastorakos, Yuri Martin Wright, and Konstantinos Boulouchos. Diesel engine simulations with multi-dimensional conditional moment closure. *Combustion Science and Technology*, 180(5):883–899, 2008.
  - [35] John E Dec and Wontae Hwang. Characterizing the development of thermal stratification in an HCCI engine using planar-imaging thermometry. *SAE International Journal of Engines*, 2(1):421–438, 2009.
  - [36] John E Dec, Wontae Hwang, and Magnus Sjöberg. An investigation of thermal stratification in HCCI engines using chemiluminescence imaging. Technical report, SAE Technical Paper, 2006.
  - [37] José M Desantes, J Javier López, Santiago Molina, and Darío López-Pintor. Validity of the Livengood & Wu correlation and theoretical development of an alternative procedure to predict ignition delays under variable thermodynamic conditions. *Energy Conversion and Management*, 105:836–847, 2015.
  - [38] Olivier Desjardins, Guillaume Blanquart, Guillaume Balarac, and Heinz Pitsch. High order conservative finite difference scheme for variable density low mach number turbulent flows. *Journal of Computational Physics*, 227(15):7125–7159, 2008.
  - [39] AM Douaud and P Eyzat. Four-octane-number method for predicting the anti-knock behavior of fuels and engines. SAE Technical Paper 780080, 1978.
  - [40] Nicolas Dronniou and John Dec. Investigating the development of thermal stratification from the near-wall regions to the bulk-gas in an HCCI engine with

- planar imaging thermometry. *SAE International Journal of Engines*, 5(3):1046–1074, 2012.
- [41] Alessandro dAdamo, Sebastiano Breda, and Giuseppe Cantore. Large-eddy simulation of cycle-resolved knock in a turbocharged SI engine. *Energy Procedia*, 82:45–50, 2015.
  - [42] Peter Eckert, Song-Charng Kong, and Rolf D Reitz. Modeling autoignition and engine knock under spark ignition conditions. SAE Technical Paper 2003-01-0011, 2003.
  - [43] Colin R Ferguson, Robert M Green, and Robert P Lucht. Unburned gas temperatures in an internal combustion engine. ii: Heat release computations. *Combustion Science and Technology*, 55(1-3):63–81, 1987.
  - [44] Stefano Fontanesi, Alessandro dAdamo, and Christopher J Rutland. Large-eddy simulation analysis of spark configuration effect on cycle-to-cycle variability of combustion and knock. *International Journal of Engine Research*, 16(3):403–418, 2015.
  - [45] Stefano Fontanesi, Stefano Paltrinieri, Alessandro DAdamo, Giuseppe Cantore, and Christopher Rutland. Knock tendency prediction in a high performance engine using LES and tabulated chemistry. *SAE International Journal of Fuels and Lubricants*, 6(1):98–118, 2013.
  - [46] M Germano, A Maffio, S Sello, and G Mariotti. On the extension of the dynamic modelling procedure to turbulent reacting flows. In *Direct and Large-Eddy Simulation II*, pages 291–300. Springer, 1997.
  - [47] JF Griffiths, JP MacNamara, CGW Sheppard, DA Turton, and BJ Whitaker. The relationship of knock during controlled autoignition to temperature inhomogeneities and fuel reactivity. *Fuel*, 81(17):2219–2225, 2002.
  - [48] MP Halstead, LJ Kirsch, A Prothero, and CP Quinn. A mathematical model for hydrocarbon autoignition at high pressures. *Proceedings of the Royal Society of London. A. Mathematical and Physical Sciences*, 346(1647):515–538, 1975.
  - [49] MP Halstead, LJ Kirsch, and CP Quinn. The autoignition of hydrocarbon fuels at high temperatures and pressuresfitting of a mathematical model. *Combustion and Flame*, 30:45–60, 1977.
  - [50] RE Herold, JM Krasselt, David E Foster, JB Ghandhi, DL Reuss, and PM Najt. Investigations into the effects of thermal and compositional stratification on HCCI combustion—part ii: optical engine results. *SAE International Journal of Engines*, 2(1):1034–1053, 2009.

- [51] John B Heywood. *Internal combustion engine fundamentals*. McGraw-Hill New York, 1988.
- [52] IEA. *World Energy Outlook 2018*, 2018.
- [53] Asim Iqbal. *Fundamentals of Knock*. PhD thesis, The Ohio State University, 2012.
- [54] J Janicka and W Kollmann. A two-variables formalism for the treatment of chemical reactions in turbulent h<sub>2</sub>air diffusion flames. *Symposium (International) on Combustion*, 17(1):421–430, 1979.
- [55] C Jiménez, F Ducros, Benedicte Cuenot, and Benoit Bédat. Subgrid scale variance and dissipation of a scalar field in large eddy simulations. *Physics of Fluids*, 13(6):1748–1754, 2001.
- [56] Tobias Joelsson, Rixin Yu, Xue-Song Bai, Andreas Vressner, and Bengt Johansson. Large eddy simulation and experiments of the auto-ignition process of lean ethanol/air mixture in HCCI engines. *SAE International Journal of Fuels and Lubricants*, 1(1):1110–1119, 2009.
- [57] WP Jones and S Navarro-Martinez. Numerical study of n-heptane auto-ignition using LES-PDF methods. *Flow, Turbulence and Combustion*, 83(3):407–423, 2009.
- [58] Daniel D Joseph, J Belanger, and GS Beavers. Breakup of a liquid drop suddenly exposed to a high-speed airstream. *International Journal of Multiphase Flow*, 25(6-7):1263–1303, 1999.
- [59] Nobuyuki Kawahara, Eiji Tomita, and Yoshitomo Sakata. Auto-ignited kernels during knocking combustion in a spark-ignition engine. *Proceedings of the Combustion Institute*, 31(2):2999–3006, 2007.
- [60] Robert J Kee, Fran M Rupley, and James A Miller. Chemkin-II: A Fortran chemical kinetics package for the analysis of gas phase chemical kinetics. Technical Report SAND89-9009B, Sandia National Laboratories, 1996.
- [61] Seung Hyun Kim. A front propagation formulation for under-resolved reaction fronts. *Journal of Computational Physics*, 285:193–207, 2015.
- [62] Seung Hyun Kim and Kang Y Huh. Use of the conditional moment closure model to predict NO formation in a turbulent CH<sub>4</sub>/H<sub>2</sub> flame over a bluff-body. *Combustion and Flame*, 130(1-2):94–111, 2002.

- [63] Seung Hyun Kim, Kang Y Huh, and Robert W Bilger. Second-order conditional moment closure modeling of local extinction and reignition in turbulent non-premixed hydrocarbon flames. *Proceedings of the Combustion Institute*, 29(2):2131–2137, 2002.
- [64] Seung Hyun Kim, Kang Y Huh, and Roydon A Fraser. Modeling autoignition of a turbulent methane jet by the conditional moment closure model. *Proceedings of the Combustion Institute*, 28(1):185–191, 2000.
- [65] Seung Hyun Kim, Kang Y Huh, and Liu Tao. Application of the elliptic conditional moment closure model to a two-dimensional nonpremixed methanol bluff-body flame. *Combustion and Flame*, 120(1-2):75–90, 2000.
- [66] A Yu Klimenko. Multicomponent diffusion of various admixtures in turbulent flow. *Fluid Dynamics*, 25(3):327–334, 1990.
- [67] Alex Y Klimenko and Robert William Bilger. Conditional moment closure for turbulent combustion. *Progress in Energy and Combustion Science*, 25(6):595–687, 1999.
- [68] Song-Charng Kong, Zhiyu Han, and Rolf D Reitz. The development and application of a diesel ignition and combustion model for multidimensional engine simulation. *SAE Transactions*, pages 502–518, 1995.
- [69] Song-Charng Kong, Craig D Marriott, Rolf D Reitz, and Magnus Christensen. Modeling and experiments of HCCI engine combustion using detailed chemical kinetics with multidimensional CFD. SAE Technical Paper 2001-01-1026, 2001.
- [70] Song-Charng Kong and Rolf D Reitz. Application of detailed chemistry and CFD for predicting direct injection HCCI engine combustion and emissions. *Proceedings of the Combustion Institute*, 29(1):663–669, 2002.
- [71] Song-Charng Kong, Rolf D Reitz, Magnus Christensen, and Bengt Johansson. Modeling the effects of geometry generated turbulence on HCCI engine combustion. *SAE Transactions*, pages 1511–1521, 2003.
- [72] Markus Kraft, Peter Maigaard, Fabian Mauss, Magnus Christensen, and Bengt Johansson. Investigation of combustion emissions in a HCCI engine: Measurements and a new computational model. *Proceedings of the Combustion Institute*, 28:1195–1201, 2000.
- [73] A Kronenburg. Double conditioning of reactive scalar transport equations in turbulent nonpremixed flames. *Physics of Fluids*, 16(7):2640–2648, 2004.

- [74] A Kronenburg and AE Papoutsakis. Conditional moment closure modeling of extinction and re-ignition in turbulent non-premixed flames. *Proceedings of the Combustion Institute*, 30(1):759–766, 2005.
- [75] Guillaume Lecocq, Stéphane Richard, Jean-Baptiste Michel, and Luc Vervisch. A new LES model coupling flame surface density and tabulated kinetics approaches to investigate knock and pre-ignition in piston engines. *Proceedings of the Combustion Institute*, 33(2):3105–3114, 2011.
- [76] Pierre Leduc, Benjamin Dubar, Alain Ranini, and Gaëtan Monnier. Downsizing of gasoline engine: an efficient way to reduce CO<sub>2</sub> emissions. *Oil & Gas Science and Technology*, 58(1):115–127, 2003.
- [77] W Lee and HJ Schaefer. Analysis of local pressures, surface temperatures and engine damages under knock conditions. SAE Technical Paper 830508, 1983.
- [78] William R Leppard. A detailed chemical kinetics simulation of engine knock. *Combustion Science and Technology*, 43(1-2):1–20, 1985.
- [79] Houliang Li, David L Miller, and Nicholas P Cernansky. A study on the application of a reduced chemical reaction model to motored engines for heat release prediction. SAE Technical Paper 922328, 1992.
- [80] Long Liang, Rolf D Reitz, Claudia O Iyer, and Jianwen Yi. Modeling knock in spark-ignition engines using a G-equation combustion model incorporating detailed chemical kinetics. SAE Technical Paper 2007-01-0165, 2007.
- [81] Paul A Libby and Forman Arthur Williams. *Turbulent reacting flows*. Academic press, 1994.
- [82] MA Liberman, MF Ivanov, OE Peil, DM Valiev, and L-E Eriksson. Numerical modeling of the propagating flame and knock occurrence in spark-ignition engines. *Combustion Science and Technology*, 177(1):151–182, 2004.
- [83] Ock Taeck Lim, Hiroaki Nakano, and Norimasa Ilda. The research about the effects of thermal stratification on n-heptane/iso-octane-air mixture HCCI combustion using a rapid compression machine. Technical report, SAE Technical Paper, 2006.
- [84] Dirk Linse, Andreas Kleemann, and Christian Hasse. Probability density function approach coupled with detailed chemical kinetics for the prediction of knock in turbocharged direct injection spark ignition engines. *Combustion and Flame*, 161(4):997–1014, 2014.
- [85] Alex B Liu, Daniel Mather, and Rolf D Reitz. Modeling the effects of drop drag and breakup on fuel sprays. *SAE Transactions*, pages 83–95, 1993.

- [86] Shiling Liu, John C Hewson, Jacqueline H Chen, and Heinz Pitsch. Effects of strain rate on high-pressure nonpremixed n-heptane autoignition in counterflow. *Combustion and Flame*, 137(3):320–339, 2004.
- [87] Xu-Dong Liu, Stanley Osher, and Tony Chan. Weighted essentially non-oscillatory schemes. *Journal of Computational Physics*, 115(1):200–212, 1994.
- [88] JC Livengood and PC Wu. Correlation of autoignition phenomena in internal combustion engines and rapid compression machines. In *Symposium (International) on Combustion*, volume 5, pages 347–356. Elsevier, 1955.
- [89] TS Lundgren. Linearly forced isotropic turbulence. *Annual Research Briefs*, pages 461–473, 2003.
- [90] Minh Bau Luong, Zhaoyu Luo, Tianfeng Lu, Suk Ho Chung, and Chun Sang Yoo. Direct numerical simulations of the ignition of lean primary reference fuel/air mixtures with temperature inhomogeneities. *Combustion and Flame*, 160(10):2038–2047, 2013.
- [91] Minh Bau Luong, Gwang Hyeon Yu, Tianfeng Lu, Suk Ho Chung, and Chun Sang Yoo. Direct numerical simulations of ignition of a lean n-heptane/air mixture with temperature and composition inhomogeneities relevant to HCCI and SCCI combustion. *Combustion and Flame*, 2015.
- [92] SM Martin, JC Kramlich, G Kosaly, and JJ Riley. The premixed conditional moment closure method applied to idealized lean premixed gas turbine combustors. *Journal of Engineering for Gas Turbines and Power*, 125(4):895–900, 2003.
- [93] Antony Misdariis, Olivier Vermorel, and Thierry Poinsot. A methodology based on reduced schemes to compute autoignition and propagation in internal combustion engines. *Proceedings of the Combustion Institute*, 35(3):3001–3008, 2014.
- [94] Antony Misdariis, Olivier Vermorel, and Thierry Poinsot. LES of knocking in engines using dual heat transfer and two-step reduced schemes. *Combustion and Flame*, 162(11):4304–4312, 2015.
- [95] Eduard Moses, Alexander L Yarin, and Pinhas Bar-Yoseph. On knocking prediction in spark ignition engines. *Combustion and Flame*, 101(3):239–261, 1995.
- [96] Johannes Gerhard Mutzke. *Abnormal combustion in spark ignition engines*. PhD thesis, University of Oxford, 2018.
- [97] S Navarro-Martinez and A Kronenburg. LES–CMC simulations of a lifted methane flame. *Proceedings of the Combustion Institute*, 32(1):1509–1516, 2009.

- [98] Henrik Nordgren, Anders Hultqvist, and Bengt Johansson. Start of injection strategies for HCCI-combustion. Technical report, SAE Technical Paper, 2004.
- [99] Jenny Nygren, Johan Hult, Mattias Richter, Marcus Aldén, Magnus Christensen, Anders Hultqvist, and Bengt Johansson. Three-dimensional laser induced fluorescence of fuel distributions in an HCCI engine. *Proceedings of the Combustion Institute*, 29(1):679–685, 2002.
- [100] Peter J O’Rourke and AA Amsden. A spray/wall interaction submodel for the KIVA-3 wall film model. *SAE Transactions*, pages 281–298, 2000.
- [101] Pinaki Pal, Yunchao Wu, Tianfeng Lu, Sibendu Som, Yee Chee See, and Alexandra Le Moine. Multi-dimensional CFD simulations of knocking combustion in a CFR engine. In *ASME 2017 Internal Combustion Engine Division Fall Technical Conference*, pages V002T06A017–V002T06A017. American Society of Mechanical Engineers, 2017.
- [102] Pinaki Pal, Yunchao Wu, Tianfeng Lu, Sibendu Som, Yee Chee See, and Alexandra Le Moine. Multidimensional numerical simulations of knocking combustion in a cooperative fuel research engine. *Journal of Energy Resources Technology*, 140(10):102205, 2018.
- [103] Thierry Passot and Annick Pouquet. Numerical simulation of compressible homogeneous flows in the turbulent regime. *Journal of Fluid Mechanics*, 181:441–466, 1987.
- [104] Zhijun Peng, Hua Zhao, Tom Ma, and Nicos Ladommatos. Characteristics of homogeneous charge compression ignition (HCCI) combustion and emissions of n-heptane. *Combustion Science and Technology*, 177(11):2113–2150, 2005.
- [105] N Peters, W Hocks, and G Mohiuddin. Turbulent mean reaction rates in the limit of large activation energies. *Journal of Fluid Mechanics*, 110:411–432, 1981.
- [106] Dominique Petitjean, Luciano Bernardini, Chris Middlemass, and SM Shahed. Advanced gasoline engine turbocharging technology for fuel economy improvements. Technical report, SAE Technical Paper, 2004.
- [107] Charles D Pierce and Parviz Moin. A dynamic model for subgrid-scale variance and dissipation rate of a conserved scalar. *Physics of Fluids*, 10(12):3041–3044, 1998.
- [108] Thierry Poinsot and Denis Veynante. *Theoretical and numerical combustion*. RT Edwards, Inc., 2005.

- [109] E. Pomraning. *Development of large eddy simulation turbulence models*. PhD thesis, University of WisconsinMadison, 2000.
- [110] Rolf D Reitz and R Diwakar. Structure of high-pressure fuel sprays. *SAE Transactions*, pages 492–509, 1987.
- [111] M Ribaucour, R Minetti, LR Sochet, HJ Curran, WJ Pitz, and CK Westbrook. Ignition of isomers of pentane: an experimental and kinetic modeling study. *Proceedings of the Combustion Institute*, 28(2):1671–1678, 2000.
- [112] KJ Richards, PK Senecal, and E Pomraning. CONVERGE manual (version 2.3). *Convergent Science Inc., Madison, WI-USA*, 2016.
- [113] Mattias Richter, Axel Franke, Marcus Alden, Anders Hultqvist, and Bengt Johansson. Optical diagnostics applied to a naturally aspirated homogeneous charge compression ignition engine. Technical report, SAE Technical Paper, 1999.
- [114] A Robert, Stéphane Richard, Olivier Colin, Lionel Martinez, and Loic De Francqueville. LES prediction and analysis of knocking combustion in a spark ignition engine. *Proceedings of the Combustion Institute*, 35(3):2941–2948, 2015.
- [115] Anthony Robert, Stéphane Richard, Olivier Colin, and Thierry Poinsot. LES study of deflagration to detonation mechanisms in a downsized spark ignition engine. *Combustion and Flame*, 162(7):2788–2807, 2015.
- [116] Anthony Robert, Karine Truffin, Nicolas Iafrate, Stephane Jay, Olivier Colin, and Christian Angelberger. Large-eddy simulation analysis of knock in a direct injection spark ignition engine. *International Journal of Engine Research*, 20(7):765–776, 2019.
- [117] MR Roomina and RW Bilger. Conditional moment closure (CMC) predictions of a turbulent methane-air jet flame. *Combustion and Flame*, 125(3):1176–1195, 2001.
- [118] CJ Rutland. Large-eddy simulations for internal combustion engines—a review. *International Journal of Engine Research*, 12(5):421–451, 2011.
- [119] Fatemeh Salehi, Mohsen Talei, Evatt R Hawkes, Ankit Bhagatwala, Jacqueline H Chen, Chun Sang Yoo, and Sanghoon Kook. Doubly conditional moment closure modelling for HCCI with temperature inhomogeneities. *Proceedings of the Combustion Institute*, 36(3):3677–3685, 2017.

- [120] Fatemeh Salehi, Mohsen Talei, Evatt R Hawkes, Chun Sang Yoo, Tommaso Lucchini, Gianluca D'Errico, and Sanghoon Kook. Conditional moment closure modelling for HCCI with temperature inhomogeneities. *Proceedings of the Combustion Institute*, 35(3):3087–3095, 2015.
- [121] Samveg Saxena and Iván D Bedoya. Fundamental phenomena affecting low temperature combustion and HCCI engines, high load limits and strategies for extending these limits. *Progress in Energy and Combustion Science*, 39(5):457–488, 2013.
- [122] H Schäpertöns and W Lee. Multidimensional modelling of knocking combustion in SI engines. SAE Technical Paper 850502, 1985.
- [123] R Schießl and U Maas. Analysis of endgas temperature fluctuations in an SI engine by laser-induced fluorescence. *Combustion and Flame*, 133(1-2):19–27, 2003.
- [124] Jaeyeob Seo, Dongkyu Lee, Kang Y Huh, and Jaewoo Chung. Combustion simulation of a diesel engine in the pHCCI mode with split injections by the spatially integrated CMC model. *Combustion Science and Technology*, 182(9):1241–1260, 2010.
- [125] Jiankun Shao and Christopher Rutland. Modeling investigation of auto-ignition and engine knock by HO<sub>2</sub>. SAE Technical Paper 2014-01-1221, apr 2014.
- [126] Magnus Sjöberg and John E Dec. An investigation of the relationship between measured intake temperature, BDC temperature, and combustion phasing for premixed and DI HCCI engines. *SAE Transactions*, pages 1271–1286, 2004.
- [127] Magnus Sjöberg and John E Dec. Effects of engine speed, fueling rate, and combustion phasing on the thermal stratification required to limit HCCI knocking intensity. *SAE Transactions*, pages 1472–1486, 2005.
- [128] Magnus Sjöberg and John E Dec. Comparing late-cycle autoignition stability for single-and two-stage ignition fuels in HCCI engines. *Proceedings of the Combustion Institute*, 31(2):2895–2902, 2007.
- [129] Magnus Sjöberg, John E Dec, Aristotelis Babajimopoulos, and Dennis N Assanis. Comparing enhanced natural thermal stratification against retarded combustion phasing for smoothing of HCCI heat-release rates. SAE Technical Paper 2004-01-2994, 2004.
- [130] Magnus Sjöberg, John E Dec, and Nicholas P Cernansky. Potential of thermal stratification and combustion retard for reducing pressure-rise rates in HCCI engines, based on multi-zone modeling and experiments. SAE Technical Paper 2005-01-0113, 2005.

- [131] Magnus Sjöberg, Lars-Olof Edling, Torbjörn Eliassen, Lars Magnusson, and Hans-Erik Ångström. GDI HCCI: effects of injection timing and air swirl on fuel stratification, combustion and emissions formation. *SAE Transactions*, pages 407–424, 2002.
- [132] J Ray Smith, SM Aceves, C Westbrook, and W Pitz. Modeling of homogeneous charge compression ignition (HCCI) of methane. Technical report, Lawrence Livermore National Lab., CA (United States), 1997.
- [133] Derek A Splitter, Arthur Gilliam, James Szybist, and Jaal Ghandhi. Effects of pre-spark heat release on engine knock limit. *Proceedings of the Combustion Institute*, 37(4):4893–4900, 2019.
- [134] Rudolf H Stanglmaier and Charles E Roberts. Homogeneous charge compression ignition (HCCI): benefits, compromises, and future engine applications. *SAE Transactions*, pages 2138–2145, 1999.
- [135] Edward S Suh and Christopher J Rutland. Numerical study of fuel/air mixture preparation in a GDI engine. *SAE Transactions*, pages 2185–2201, 1999.
- [136] N Swaminathan and RW Bilger. Analyses of conditional moment closure for turbulent premixed flames. *Combustion Theory and Modelling*, 5(2):241–260, 2001.
- [137] N Swaminathan and KNC Bray. Effect of dilatation on scalar dissipation in turbulent premixed flames. *Combustion and Flame*, 143(4):549–565, 2005.
- [138] James P Szybist and Derek A Splitter. Pressure and temperature effects on fuels with varying octane sensitivity at high load in si engines. *Combustion and Flame*, 177:49–66, 2017.
- [139] Ben Thornber, RW Bilger, AR Masri, and ER Hawkes. An algorithm for LES of premixed compressible flows using the conditional moment closure model. *Journal of Computational Physics*, 230(20):7687–7705, 2011.
- [140] A Triantafyllidis, E Mastorakos, and RLGM Eggels. Large eddy simulations of forced ignition of a non-premixed bluff-body methane flame with conditional moment closure. *Combustion and Flame*, 156(12):2328–2345, 2009.
- [141] Karine Truffin and Olivier Colin. Auto-ignition model based on tabulated detailed kinetics and presumed temperature pdf-application to internal combustion engine controlled by thermal stratifications. *International Journal of Heat and Mass Transfer*, 54(23-24):4885–4894, 2011.

- [142] Jeroen Vancoillie, Louis Sileghem, and Sebastian Verhelst. Development and validation of a quasi-dimensional model for methanol and ethanol fueled si engines. *Applied Energy*, 132:412–425, 2014.
- [143] Olivier Vermorel, Stéphane Richard, Olivier Colin, Christian Angelberger, Adlène Benkenida, and Denis Veynante. Towards the understanding of cyclic variability in a spark ignited engine using multi-cycle LES. *Combustion and Flame*, 156(8):1525–1541, 2009.
- [144] Denis Veynante and Luc Vervisch. Turbulent combustion modeling. *Progress in Energy and Combustion Science*, 28(3):193–266, 2002.
- [145] Wei Wang and Seung Hyun Kim. Sensible-enthalpy-based conditional moment closure model for homogeneous charge compression ignition with temperature inhomogeneity. *Flow, Turbulence and Combustion*, pages 1–20, 2018.
- [146] Zhi Wang, Hui Liu, and Rolf D Reitz. Knocking combustion in spark-ignition engines. *Progress in Energy and Combustion Science*, 61:78–112, 2017.
- [147] Haiqiao Wei, Ceyuan Chen, Hua Zhou, Wanhui Zhao, and Zhuyin Ren. Effect of turbulent mixing on the end gas auto-ignition of n-heptane/air mixtures under ic engine-relevant conditions. *Combustion and Flame*, 174:25–36, 2016.
- [148] Charles K Westbrook. Chemical kinetics of hydrocarbon ignition in practical combustion systems. *Proceedings of the Combustion Institute*, 28(2):1563–1577, 2000.
- [149] Charles K Westbrook, Jürgen Warnatz, and William J Pitz. A detailed chemical kinetic reaction mechanism for the oxidation of iso-octane and n-heptane over an extended temperature range and its application to analysis of engine knock. *Symposium (International) on Combustion*, 22(1):893–901, 1989.
- [150] YM Wright, K Boulouchos, G De Paola, and E Mastorakos. Multi-dimensional conditional moment closure modelling applied to a heavy-duty common-rail diesel engine. *SAE International Journal of Engines*, 2(1):714–726, 2009.
- [151] YM Wright, G De Paola, Konstantinos Boulouchos, and E Mastorakos. Simulations of spray autoignition and flame establishment with two-dimensional CMC. *Combustion and Flame*, 143(4):402–419, 2005.
- [152] Yunchao Wu, Pinaki Pal, Sibendu Som, and Tianfeng Lu. A skeletal chemical kinetic mechanism for gasoline and gasoline/ethanol blend surrogates for engine CFD applications. In *International Conference on Chemical Kinetics, Chicago, IL, May*, pages 21–25, 2017.

- [153] Hongming Xu, Michael Liu, Shadi Gharahbaghi, Steve Richardson, Miroslaw Wyszynski, and Thanos Megaritis. Modelling of HCCI engines: Comparison of single-zone, multi-zone and test data. Technical report, SAE Technical Paper, 2005.
- [154] Chun Sang Yoo, Tianfeng Lu, Jacqueline H Chen, and Chung K Law. Direct numerical simulations of ignition of a lean n-heptane/air mixture with temperature inhomogeneities at constant volume: Parametric study. *Combustion and Flame*, 158(9):1727–1741, 2011.
- [155] YZ Zhang, EH Kung, and DC Haworth. A PDF method for multidimensional modeling of HCCI engine combustion: effects of turbulence/chemistry interactions on ignition timing and emissions. *Proceedings of the Combustion Institute*, 30(2):2763–2771, 2005.
- [156] Fuquan Zhao, Thomas N Asmus, Dennis N Assanis, John E Dec, James A Eng, and Paul M Najt. Homogeneous charge compression ignition (HCCI) engines. SAE Technical Paper PT-94, 2003.